CHALMERS
UNIVERSITY OF TECHNOLOGY

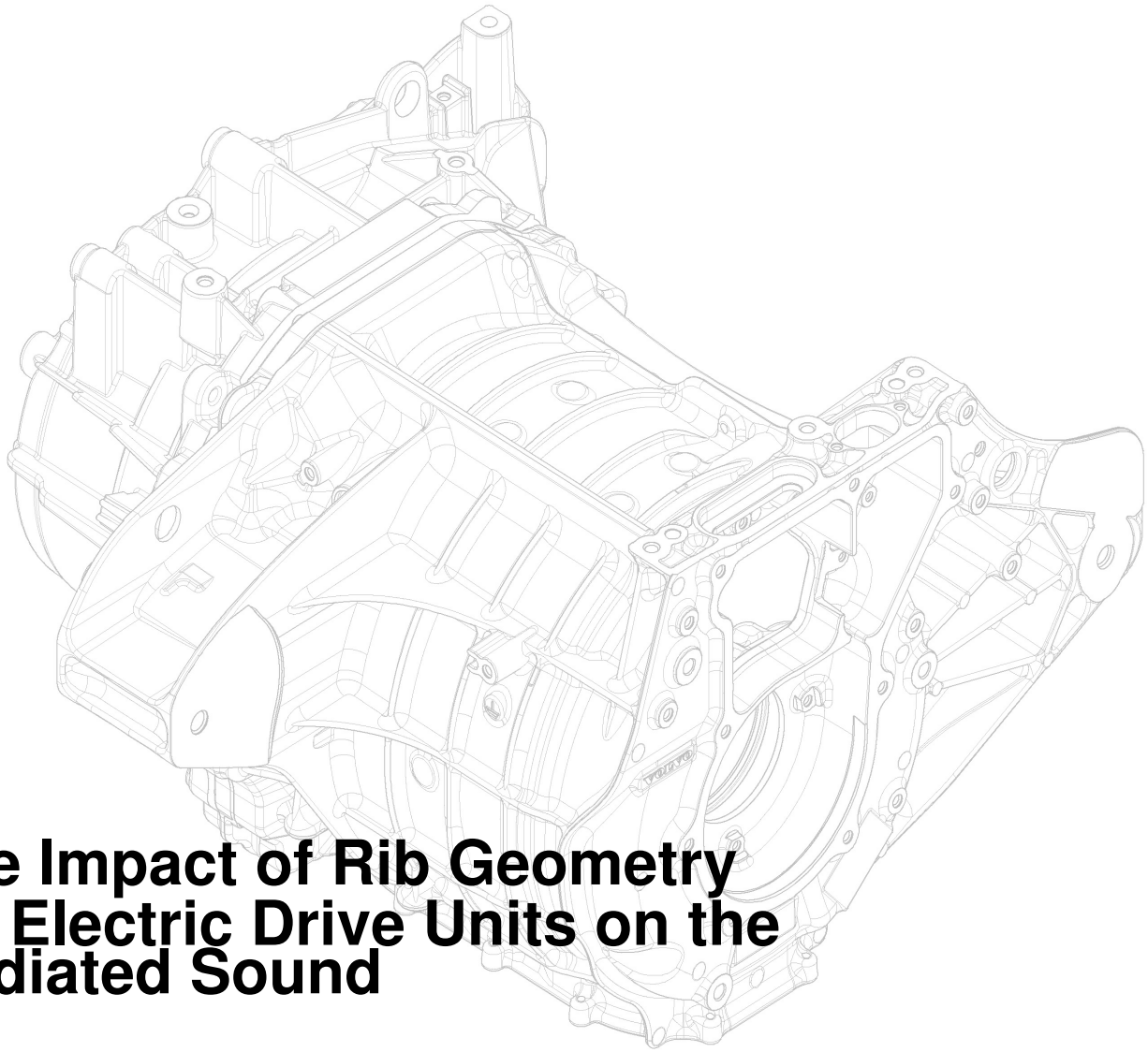

The Impact of Rib Geometry for Electric Drive Units on the Radiated Sound

Master's thesis in Mobility Engineering

OSKAR MALM
JAKOB WURZINGER

DEPARTMENT OF MECHANICS AND MARITIME SCIENCES

CHALMERS UNIVERSITY OF TECHNOLOGY
Gothenburg, Sweden 2024
www.chalmers.se

Master's thesis 2024

The Impact of Rib Geometry for electric Drive Units on the Radiated Sound

OSKAR MALM
JAKOB WURZINGER

CHALMERS
UNIVERSITY OF TECHNOLOGY

Department of Mechanics and Maritime Sciences
Division of Dynamics
Chalmers University of Technology
Gothenburg, Sweden 2024

The Impact of Rib Geometry for Electric Drive Units on the Radiated Sound
OSKAR MALM & JAKOB WURZINGER

Supervisors: David Lennström, technical expert driveline NVH and sound quality, Volvo Cars.
Johan Cederlund, technical expert multibody dynamics, Volvo Cars.
Examiner: Håkan Johansson, Professor at Mechanics and Maritime Sciences, Division of Dynamics, Chalmers University of Technology

Master's Thesis 2024
Department of Mechanics and Maritime Sciences
Division of Dynamics
Chalmers University of Technology
SE-412 96 Gothenburg
Telephone +46 31 772 1000

Cover: Drawing of an existing electric drive unit (EDU) from Volvo Cars.

Typeset in LaTeX
Printed by Chalmers Reproservice
Gothenburg, Sweden 2024

The Impact of Rib Geometry for Electric Drive Units on the Radiated Sound
OSKAR MALM
JAKOB WURZINGER
Department of Mechanics and Maritime Sciences
Chalmers University of Technology

Abstract

In recent years, the automotive industry has been moving towards electrification of vehicles. One of the most essential parts of electric vehicles are the electric drive units or EDUs, which convert electrical energy into mechanical energy that drive the wheels. An EDU typically consists of several parts, such as an electric motor, gearbox, and differential, which are encapsulated in an aluminum housing. The housing has ribs, that can increase the stiffness or casting quality of the housing. These design requirements are to fulfill the crash safety requirements, as well as noise, vibration, and harshness (NVH) requirements in terms of structure born noise. The combination of these requirements, can result in ribs which has be observed to in some cases, produce unwanted airborne sound.

To investigate how the rib geometry affect the sound radiated from ribs, a number geometry of variations was performed on four different base models. This includes curvature of the outer edge, dimensions (area), angles, etc. These variations were then simulated by meshing the CAD models in ANSA, calculating the nodal displacement of the surface nodes in NASTRAN using a velocity boundary condition, and mapping the displacements to the air using an acoustic mesh in Actran. The simulations were performed for frequencies between 100 Hz and 6 kHz. Finally, the radiated power, radiation efficiency, and mean square velocity was saved from the simulations and analyzed for each geometrical variation.

The first bending mode was found to have a large impact on the radiated sound and has a strong connection to the bending stiffness of the rib. The peak mean square velocity always occurs at the first bending mode however, the radiation efficiency does not show any general pattern and is therefore difficult to predict. From the simulations, it could be concluded that the area of the rib has the largest impact on the radiated power, which is a clear indication to design as small ribs as possible. It could also be shown that for some ribs, it is beneficial in terms of reducing the radiated power, to add a small curvature to the outer edge. A relationship between the dimensions of the ribs and the thickness of the rib was also found, where some thickness increases or decreases the radiated power for ribs with same dimensions. Finally, two adjacent ribs can interact to increase the radiated power significantly for some distances or angle between the ribs.

Keywords: Acoustic simulations, Actran, Electric driveline, Electric drive unit, Radiation efficiency, Ribbed structures, Structural vibrations and sound radiation.

Acknowledgements

During our work with this thesis, we have been grateful for receiving support and feedback from several people to whom we want to express our gratitude.

Firstly, we would like to express our deepest gratitude to Johan Cederlund and David Lennström, our supervisors at Volvo Cars, for their invaluable support and insightful feedback. We would also like to express our profound appreciation to our examiner and supervisor, Håkan Johansson, at Chalmers University of Technology, for his indispensable support and guidance. Furthermore, we would also like to thank the entire team at Volvo Cars for the opportunity to carry out this thesis.

We would also like to extend our thanks to Benjamin Grozdanic, at Hexagon, for his endless technical support and shown interest for the simulations. Also a huge thanks to the rest of the team at Hexagon for their help with troubleshooting and for providing software licences for our thesis. Finally, we are grateful for Peter Petrov, at Volvo Cars, for his shown interest and his help with creating the models in CAD.

Oskar Malm & Jakob Wurzinger, Gothenburg, June 2024

Contents

List of Figures

List of Tables

1

Introduction

1.1 Background

In recent years, the automotive industry has been moving towards electrification of vehicles which has called for a lot of development of new technologies. This includes Volvo Cars, which has the goal of only producing battery electric vehicles (BEVs) by 2030 and becoming a carbon-neutral company by 2040 [5]. One of the most essential parts of electric vehicles are the electric drive units (EDUs), which convert electrical energy into mechanical energy, which drives the wheels. A typical EDU consists of several different parts, such as an electric motor, gearbox, and differential, which are encapsulated in a housing and an inverter that can be mounted on the housing. The housing, which is made of aluminum, has ribs that can increase the stiffness of the housing or, for example, improve the casting quality, but most importantly, ensure the desired stiffness in the points where the motor mounts are connected to the EDU. The reason for these design requirements is for safety reasons to ensure that the front of the car deforms in a safe and controlled way in the event of a crash. There are also noise, vibration, and harshness (NVH) requirements in terms of structure-borne noise. The combination of these requirements affects the design of the ribs. Furthermore, the ribs can also influence the acoustic performance of the EDUs, as they can act as sound-emitting surfaces. The radiated sound from electric drivelines is more tonal and has a larger frequency range compared to the sound emitted from internal combustion engines. For this reason, it is important to investigate and understand how the geometrical properties of the ribs influence the radiated sound, in terms of shape, size, orientation, and spacing. Previous acoustic measurements done of the EDU housing by Volvo Cars have resulted in the discovery that some ribs radiate more than others. In Figure 1.1 below, the ribs that radiate more sound than others are highlighted.

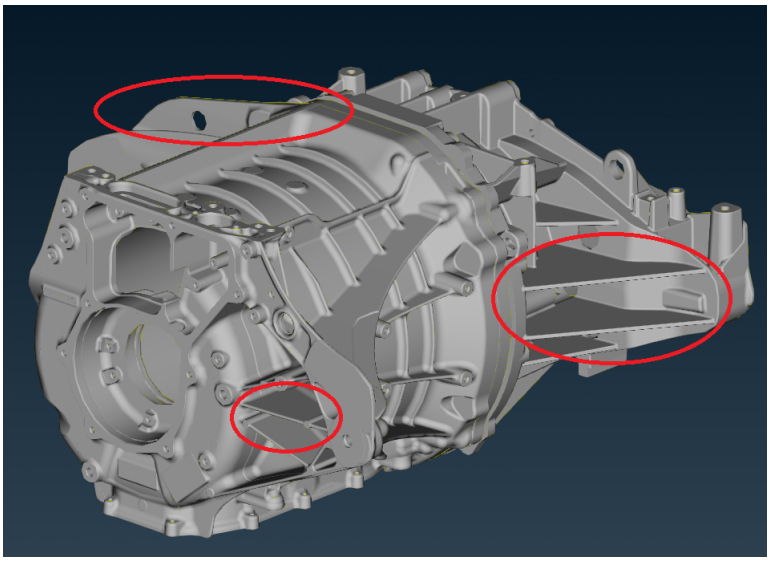

Figure 1.1: Front EDU housing with the ribs that radiate more than other ribs highlighted.

1.2 Purpose

The project aims to study the geometrical properties of ribs and gain knowledge of how this affects the acoustics of the ribs, which can lay the foundation for future guidelines that can aid mechanical designers in minimizing sound radiation.

1.3 Scope and Delimitations

The results of this study will not consist of exact descriptions of how to design the ribs but rather to find which design aspects, e.g., geometrical ratios (height and width), shape, thickness, and placement of ribs in relation to other ribs, affect the radiated sound. These findings may lay the foundation for future guidelines on how to design new ribs so that a mechanical designer will know what design aspects to avoid to minimize the radiated sound. Furthermore, due to the limited time, these findings were not tested or implemented on a complete EDU, since redesign and manufacturing were outside the project's time frame.

The project was focused on frequencies between 1 kHz and 5 kHz since this is the range of the radiated sound that is most noticeable in the cabin. Higher frequencies do not propagate into the cabin as efficiently due to the sound insulation already installed in the cars. Also, a larger frequency range increases the time for each simulation. However, to gain more knowledge about the acoustic behavior of ribs, the simulations were performed for frequencies between 100 Hz and 6 kHz.

The existing EDU housing is made of aluminum, which means that the final results are based on the properties of aluminum and not any other materials. Different materials will affect the radiated sound due to the different material properties, but

due to manufacturing and cost, aluminum was the most relevant material to study.

1.4 Research Questions

To fulfill the purpose of the thesis, the following research questions were formulated:

- Which acoustic variables affect the radiated sound power of a vibrating rib structure?
- How should acoustic simulations of a vibrating rib structure be performed?
- How do different geometrical properties of ribs, such as dimensions and curvatures, affect the radiated sound?
- Can adjacent ribs interact acoustically with each other?

The project started with a literature study to learn about the basic concepts in acoustics. In combination with the theoretical literature study, previous work done at Volvo Cars was also reviewed to get an insight into what has been done already and what needs further investigation. In parallel with the literature study, the basics of the calculation/simulation software, ANSA, NASTRAN, Meta, and Actran, were learned. After this, several prototype models were defined to illustrate as many types of rib structures as possible.

2

Theory

This chapter will present the relevant theory and knowledge that the thesis is based on.

2.1 Airborne sound

Acoustics is the science of sounds which is the wave motion in fluids and solids. Sound waves are small pressure variations that affect and can be detected by our eardrums. The pressure variations are oscillatory and propagate in a medium, meaning that molecules move back and forth in the direction of propagation with no net flow. This is displayed in Figure 2.1 below. [11]

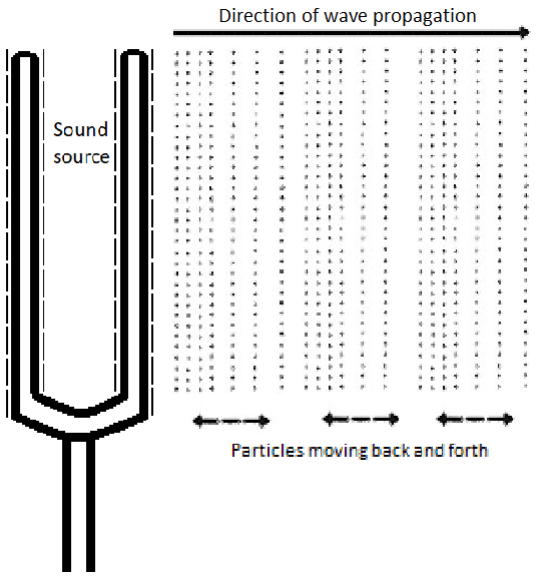

Figure 2.1: Illustration of sound propagation by particles moving back and forth.

Sound pressure is most commonly expressed as the root mean square sound pressure, P_{rms}, defined as

$$P_{rms} = \sqrt{\overline{P^2(t)}} = \left(\lim_{T \to \infty} \frac{1}{T} \int_0^T P^2(t)\, dt \right)^{\frac{1}{2}} \tag{2.1}$$

The human ear can handle sound pressure variations with a range, in magnitude, of more than a million times. It is, therefore, common to use a logarithmic scale to handle the wide range of sound pressure variations. It is also good for another reason, the perception of loudness aligns more closely with a logarithmic representation rather than a linear representation. The scale is shown in Equation 2.2 below [11].

$$L_p = 10 \cdot \log_{10}\left(\frac{{P_{rms}}^2}{{P_{ref}}^2}\right) = 20 \cdot \log_{10}\left(\frac{P_{rms}}{P_{ref}}\right) \tag{2.2}$$

L_p is called the sound pressure level (SPL) and is represented as a decibel scale (dB). The reference pressure P_{ref} is based on the threshold of human hearing for a young person at 1000 Hz ($2 \cdot 10^{-5}$ Pa), which means that $L_p = 0$ dB if $P_{rms} = P_{ref}$ [11].

The frequency of the sound wave defines the pitch of the sound, where low frequencies give a low-pitch sound and a high frequency gives a high-pitch sound, defined as Equation 2.3, and denoted as f. The speed at which the sound travels in a medium is called the propagation speed or speed of sound, denoted as c and λ is the wavelength. The speed of sound is constant within a given fluid but varies between different fluids.

$$f = \frac{c}{\lambda} \tag{2.3}$$

2.1.1 Wave equation and sound power

In Figure 2.2a is an example of two sinusoidal sound waves from one signal, where the amplitudes are the sound pressure. In reality, it is uncommon that a sound consists of only one or a few sound characteristics (frequencies and amplitudes), like in Figure 2.2a, but rather a wide frequency and amplitude range. It is, therefore, difficult to extract information from a signal in the time domain, which is why it can be beneficial to study the signal in the frequency domain, as shown in Figure 2.2b [11].

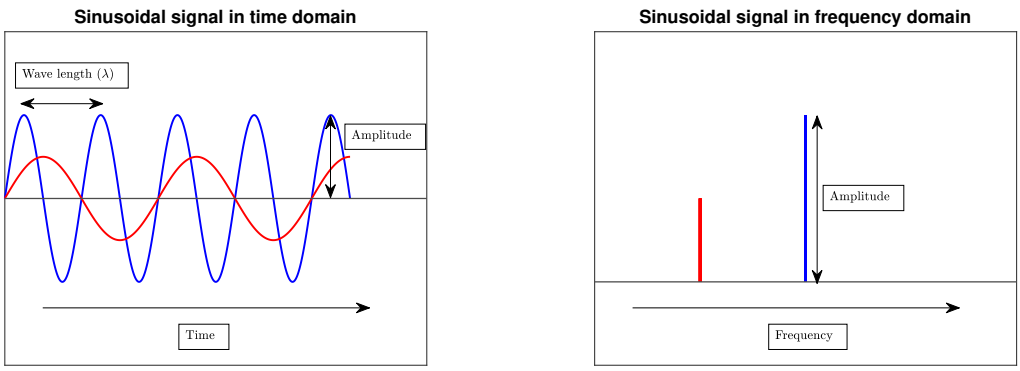

(a) Two sinusoidal signals, with a amplitude (A) and a wavelength (λ) marked.

(b) Corresponding sinusoidal signals in the frequency domain.

Figure 2.2: Two sinusoidal signals in the time and frequency domain.

To describe waves like in Figure 2.2a, but in three dimensions, in the time domain, there is an equation called the d'Alembert equation shown in Equation 2.4, which is a wave equation.

$$\nabla^2 \xi = \frac{1}{c^2} \frac{\partial^2 \xi}{\partial t^2} \tag{2.4}$$

Where ∇^2 is the Laplace's operator, defined as,

$$\nabla^2 = \frac{\partial^2}{\partial^2 x} + \frac{\partial^2}{\partial^2 y} + \frac{\partial^2}{\partial^2 z} \tag{2.5}$$

and $\xi = p$ for sound waves. To go from Equation 2.4 in the time domain to the frequency domain, like in Figure 2.2b, the Fourier transform can be used, which is shown below. [9]

$$P(\omega) = \int_{-\infty}^{\infty} p(t) e^{-j\omega t} dt \tag{2.6}$$

This results in the Helmholtz equation, defined as

$$\nabla^2 \hat{p} + k^2 \hat{p} = 0 \tag{2.7}$$

where $k = \omega / c$ and $\hat{p}$ is the complex representation of the sound pressure [11].

A sound field can be considered as an energy field that can generate, transmit, and dissipate energies. This gives a source of sound the possibility to emit power, this has shown to be very useful in noise control engineering. The usefulness comes from the fact that sound power, radiated by a source, is almost completely independent of its surroundings in the frequency range at which a human can perceive. The radiated power, W_{ac}, can be calculated by integrating the sound intensity over a closed surface:

$$\oint_S \mathbf{I} \cdot d\mathbf{S} = \oint_S \mathbf{I} \cdot \hat{\mathbf{n}} \, dS = W_{ac} \tag{2.8}$$

Where $\hat{\mathbf{n}}$ is the normal vector of the surface $\mathbf{S}$ and $\mathbf{I}$ is the time averaged sound intensity defined as,

$$\mathbf{I} = \overline{\mathbf{I}(t)} = \overline{p(t)\mathbf{u}(t)} \tag{2.9}$$

Where $p(t)$ and $\mathbf{u}(t)$ are the instantaneous sound pressure and instantaneous particle velocity, respectively.

With the sound power, the sound power level can be calculated similarly to the sound pressure level in Equation 2.2. This is shown below.

$$L_W = 10 \cdot \log_{10} \left(\frac{W_{ac}}{W_{ref}} \right) \tag{2.10}$$

Where W_{ref} is the reference power. [11]

2.1.2 Near field and far field

As described in [3], sound waves behave differently depending on the distance from the source and are divided into two groups: near field and far field. The near field is defined as the region at the sound source stretching out to a distance of approximately one wavelength. The sound waves are complex in the near field. The sound energy is circulating close to the source, and a bit further away, it's both circulating and propagating. This means that there is no specific relation between sound pressure and distance in the near field. The far field starts approximately one wavelength from the sound source and continues to infinity. The sound pressure and acoustic particle velocity are in phase in the far field and a doubling in distance results in a reduction of 6 dB in sound pressure level, assuming free field and spherical wave propagation. A free field is when there are no reflecting areas, and the sound reaches the observer directly. This is illustrated in Figure 2.3, below.

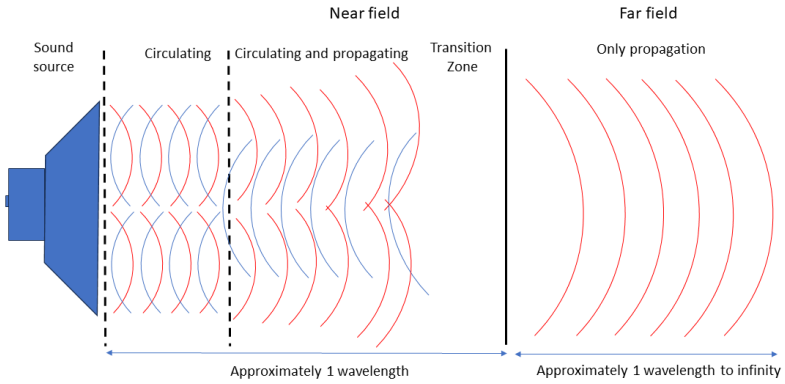

Figure 2.3: Illustration of near and far field, adapted from [3].

2.2 Structural vibration and sound radiation

Kropp [12] mentions that there are different characteristics between fluids and solids. Fluids are unable to transmit shearing forces and, therefore, only consist of longitudinal waves or compression waves. In solids, there are two types, longitudinal and transversal waves or shear waves. Transversal waves can cause a wave called a bending wave. Bending waves are the main reason for sound radiation from structures and the most common type of wave when dealing with structure-born sound.

2.2.1 Sound radiation at critical frequency

The propagation speed of bending waves (c_b) has a unique correlation with the frequency, which is that the speed of sound increases with the frequency. This is shown for both beams (c_{bb}) and plates (c_{bp}) in Equation 2.11 and 2.12.

$$c_{bb} = \left(\frac{Eh^2}{12\rho}\omega^2\right)^{\frac{1}{4}} \qquad (2.11) \qquad c_{bp} = \left(\frac{Eh^2}{12(1-\nu^2)\rho}\omega^2\right)^{\frac{1}{4}} \qquad (2.12)$$

Where h is the thickness, ρ is the density of the material of the structure, ω is the angular frequency, and ν is Poisson's ratio (about 0,33 for aluminium). Furthermore, Kropp [12] also mentions that if the propagation speed in the structure is the same as the speed of sound for the surrounding medium (e.g., 343 m/s as for air), then the corresponding frequency of the wave is referred to as the critical frequency. This is visualized in Figure 2.4, below.

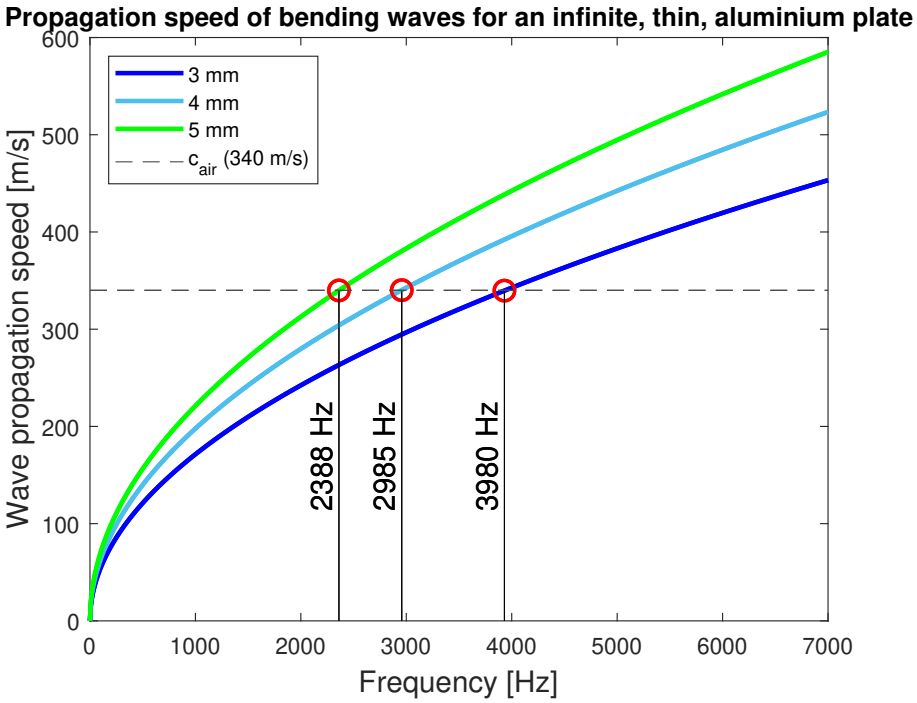

Figure 2.4: Using equation 2.12, the propagation speed of bending waves in an infinite, thin, aluminum plate plotted as a function of frequency for different thicknesses.

From Figure 2.4, it can be concluded that the critical frequency decreases as the thickness of the plate increases. Since the radiation efficiency is at its largest at the critical frequency, a thicker plate will start to radiate sound more efficiently at lower frequencies compared to a thinner plate. As described in [14], the radiation efficiency is dependent on the surface radiation impedance, Z_r, which is calculated using the following equation:

$$Z_r = \frac{i\rho_0}{\sqrt{\left(\frac{1}{c_{bp}}\right)^2 - \left(\frac{1}{c_{air}}\right)^2}} \tag{2.13}$$

Using Z_r, the radiation efficiency can be calculated by: $\frac{Re(Z_r)}{\rho_0 c_{air}}$. The efficiency of the acoustic radiation can be plotted as a function of c_{bp}:

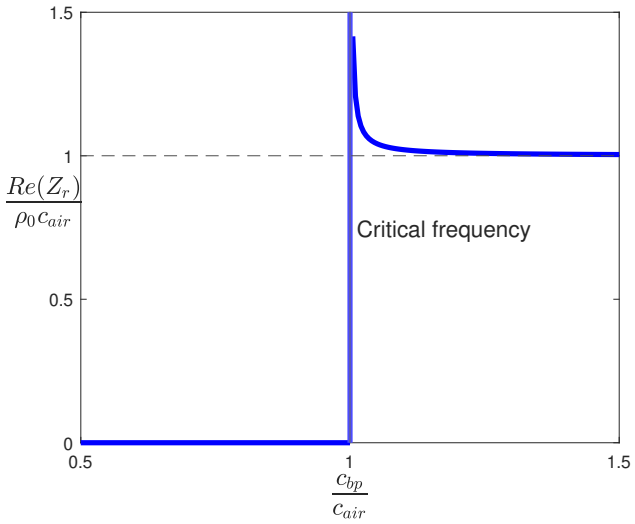

Figure 2.5: The acoustic radiation efficiency has the following dependence of c_{bp}, adapted from [14].

As shown in Figure 2.5, the efficiency goes towards infinity as c_{bp} approaches c_{air}, which is not representative of the physical world, which is caused by the denominator in Equation 2.13.

2.2.2 Sound radiation from structural vibration modes

There is also the important aspect of structural vibration modes when investigating sound radiation for vibrating structures. The modes are characterized by their modal frequency and mode shape. This means that a structure has a certain shape at a fixed frequency. For simple structures, such as one-dimensional ones, the modes are numbered based on the wavelength, where mode 1 is $\frac{\lambda}{2}$, mode 2 is λ and so on [8]. This is illustrated in Figure 2.6 and 2.7. For more complex structures, the modes are numbered by increasing the frequency.

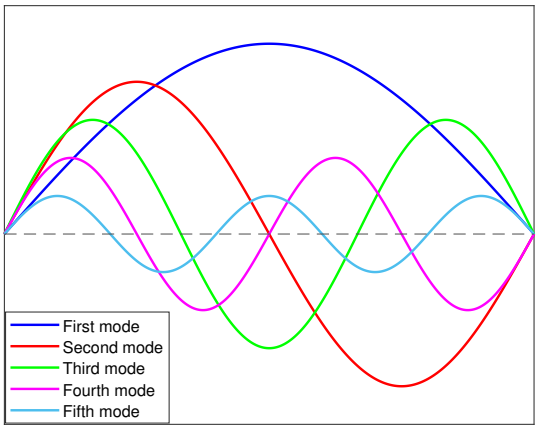

Figure 2.6: Illustration of the first 5 bending wave modes in an arbitrary one-dimensional structure.

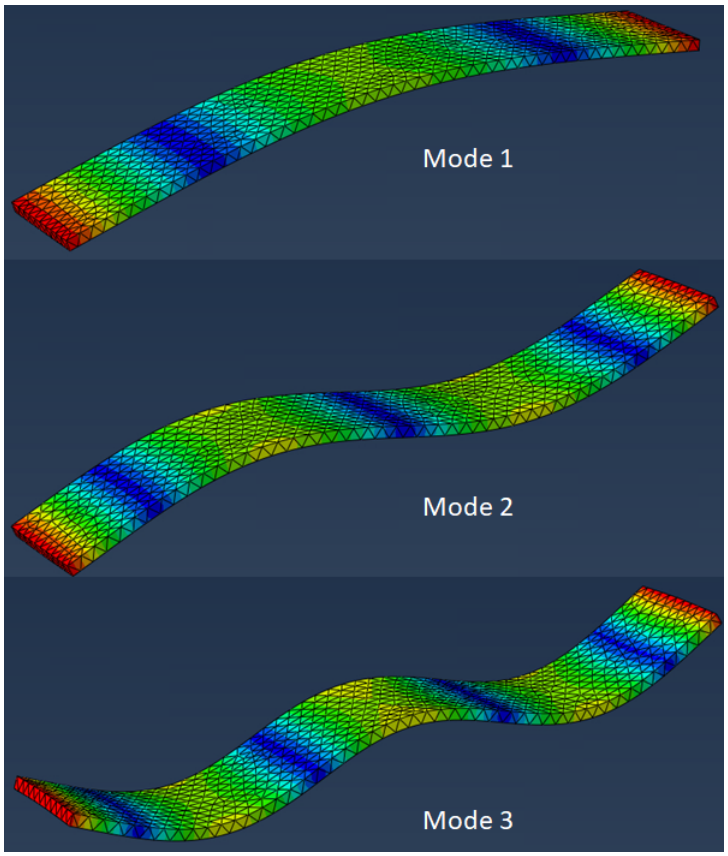

Figure 2.7: Illustration of the first 3 bending wave modes in an aluminum plate.

The radiated sound power varies depending on which mode number it has. Bending modes with odd numbers tend to radiate more than modes with even numbers, but the first bending mode tends to be the most efficient mode in terms of radiated sound. The reason is that even modes are almost completely compensated due to

hydrodynamic short-circuiting. This is illustrated in Figure 2.8. It can also be seen in Figure 2.8a that mode 1 is not compensated at all, which usually leads to the highest radiation power [12].

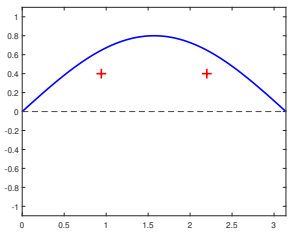

(a) Bending mode 1.

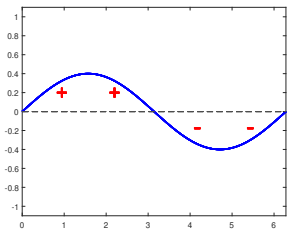

(b) Bending mode 2.

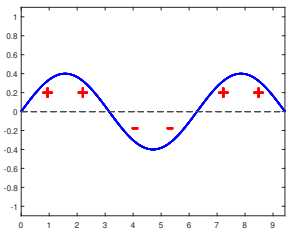

(c) Bending mode 3.

Figure 2.8: Illustrations of how a one-dimensional structure's three first bending modes affect the surrounding air pressure.

Important to note in Figure 2.6, 2.7, and 2.8 is that they are illustrated as simply supported at both ends. A fixed beam would instead have a small horizontal line, a "flat spot", at the ends. For a rib structure the reality lies somewhere in between, being fixed to a wall that can move, see Figure 3.9b. Another thing to note in e.g. Figure 2.8b is that the positive and negative poles do not need to be the same size, it depends on the geometry of the structure.

2.2.3 Equivalent radiated power and radiation efficiency

According to [6], the equivalent radiated power (ERP) of a structure that vibrates, is based on the surrounding fluid density (ρ_0), the speed of sound in the fluid (c_0), the surface area (S), and the mean square velocity of the surface (v^2). ERP is calculated by the following formula:

$$W_{ERP} = \frac{1}{2}\rho_0 c_0 S v^2 \tag{2.14}$$

The radiation efficiency, often denoted as σ, is based on the fraction of the acoustic radiated power, W_{ac} and ERP, by the following formula:

$$\sigma = \frac{W_{ac}}{W_{ERP}} \tag{2.15}$$

This quantity describes how efficiently a structure radiates acoustic power.

The radiated power, W_{ac}, therefore has two variables, v and σ, which are frequency dependent and are affected by the geometry of the structure. Using Equation 2.15, W_{ac} can be determined if σ is known:

$$W_{ac} = \sigma W_{ERP} = \frac{1}{2}\sigma\rho_0 c_0 S v^2 \tag{2.16}$$

This is one of the most important equations in this study since it describes how the acoustic radiated power, W_{ac}, depends on both the radiation efficiency and the

mean square velocity of the structure.

According to [10], there is a relationship between the physical dimensions of the vibrating structure and the radiation efficiency. Where the maximum efficiency occurs when the wavelength of the sound wave matches the dimension of the structure. The example given in the paper is a baffled cylinder and the dimension of interest is the cylinder's diameter. This example can not be directly applied to ribs, which are neither baffled nor circular, but it shows that there can be a relationship between the dimensions of the ribs and the radiation efficiency.

2.3 Human sound perception

As described in [2], humans have the ability to hear a limited range of frequencies, normally between 20 Hz and 20 kHz but with age, this range decreases. Sound with a frequency below 20 Hz is referred to as infrasound, and if the frequency exceeds 20 kHz, it is referred to as ultrasound. In terms of pressure, the ear can detect pressure fluctuations as small as 20 μPa and up to 20 Pa. Due to the big differences in this range, it is more practical to use a logarithmic scale (dB) to measure the pressure fluctuations. Furthermore, the human ear perceives sounds differently at different frequencies, which is why sound pressure measurements are usually weighted as a function of frequency. This means that a sound with a frequency of 1000 Hz is perceived as a louder sound than a sound at 100 Hz, for the same amplitude in air pressure. For this reason, weighting curves are usually applied. The A-weighting curve is the most common and accounts for the relative loudness perceived by humans [2],[1]. The weighting curves are shown in Figure 2.9, and if A-weighting is applied, then the unit is dB(A).

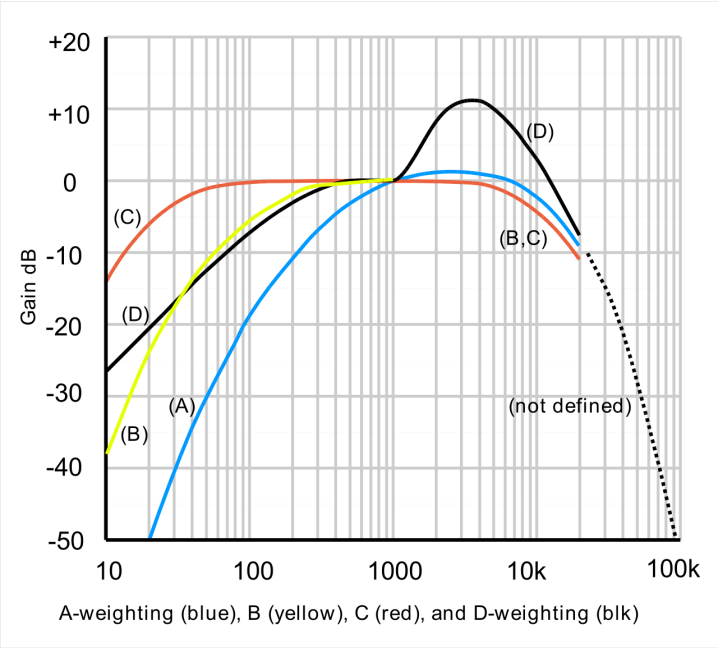

Figure 2.9: A- B- C- and D-weighting curves shown for a frequency range of 10Hz - 20KHz (from [1]).

From Figure 2.9, it can be concluded that sounds that have a frequency between around 1 kHz to 7 kHz are perceived as louder than sounds with frequencies outside of this range. This further strengthens the choice of frequency range, 1 kHz to 5 kHz, that was studied.

2.4 Finite element method (FEM) and meshing

FEM is a numerical method to calculate complex problems by dividing structures into smaller elements. Each element is simpler and can be represented by a mathematical model, which makes it easier to analyze a complete structure. There is often a trade-off between the size of the mesh elements and time, where smaller elements can give more accurate results but increase the calculation time. For acoustics, the rule of thumb is about six elements per wavelength at the highest frequency, i.e. the shortest wavelength.

According to [13], there are different types of shapes of elements but to closely mesh arbitrary geometries, triangles are needed for the surface mesh and tetrahedral for the volume mesh. These elements can be both linear (first order) or quadratic (second order). Linear elements only have nodes at the corners where the lines of the element meet while quadratic elements have an extra node on each line, meaning that the lines do not need to be straight within the element. The quadratic elements can therefore increase the accuracy but it also increases the computational time.

As explained in [6], there is also a need to mesh the fluid surrounding the structure. The exterior mesh is a volume mesh whose size and shape depend on the mesh of the structure, meaning that if quadratic triangles are used on the structure, then the exterior mesh will be quadratic tetrahedral starting at the same size as the mesh on the structure. The size of the exterior mesh gradually increases with a user-defined factor until it reaches a limit, called the finite component, also defined by the user. On the free face of the finite component, an infinite component is applied. The infinite component is supported by 2D elements which approximates the pressure on the free faces and calculates the pressure at a given distance through interpolation.

3

Methodology

In this chapter, each step of the method of the project will presented and discussed. This includes the prototype models, simulations, and validation of the results from the simulations.

3.1 Prototype models

Four different prototype models with parameterization were made to capture as many design concepts of a rib structure on an EDU as possible. The models were based on three different types of ribs inspired by an existing EDU, a rib connected on two sides, see Figure 3.1, a rib connected on two sides with a corner at the edge, see Figure 3.2 and a rib connected on three sides, see Figure 3.3. To investigate the effect of multiple ribs and cavities, the same type of rib as in Figure 3.1 was used but with two parallel ribs instead of one, making it four models in total.

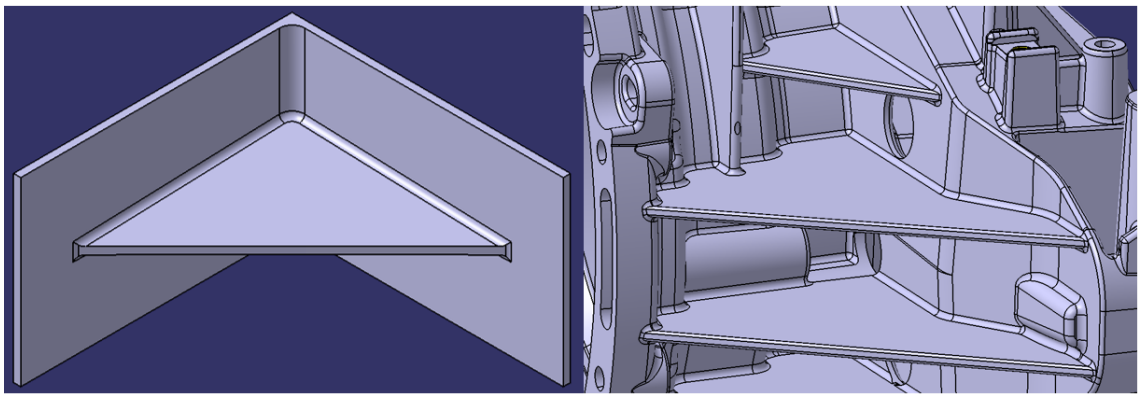

Figure 3.1: Simplified model called "M1 single" on the left and the corresponding rib from an EDU on the right.

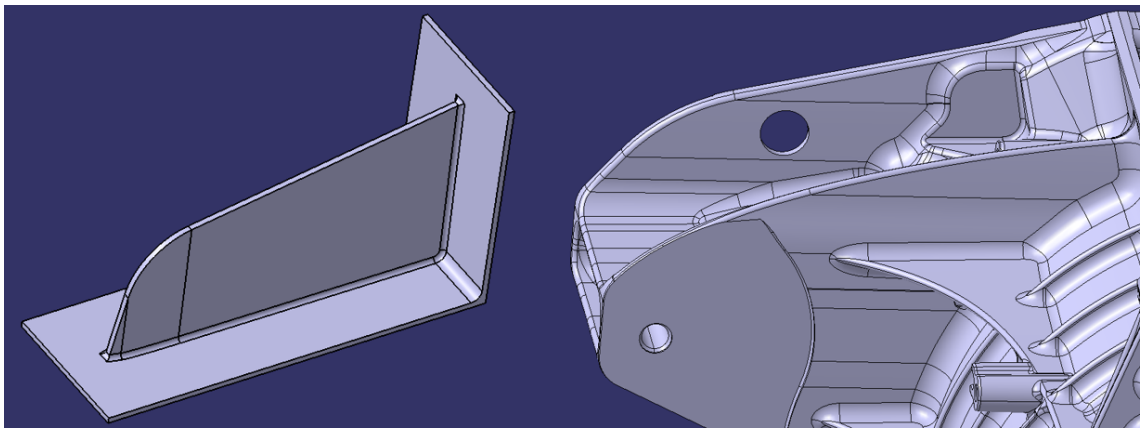

Figure 3.2: Simplified model called "M1 single corner" on the left and the corresponding rib from an EDU on the right.

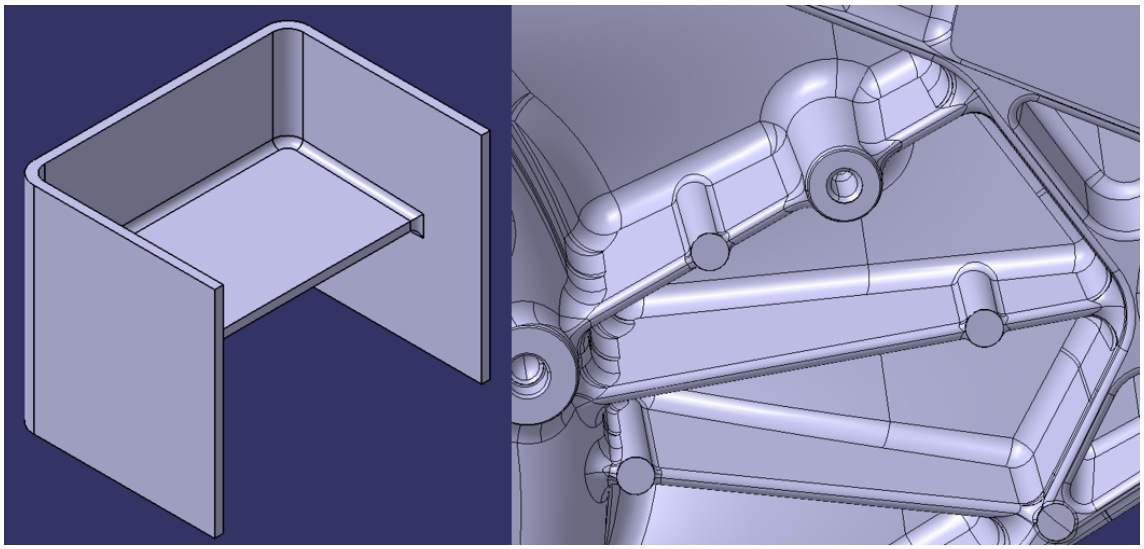

Figure 3.3: Simplified model called "M2 single" on the left and the corresponding rib from an EDU on the right.

The base models, meaning no parameterization variation has been done, have the dimensions shown in Table 3.1. These dimensions can be changed in the CAD model using the parameterization. The model called "double" is the model with two ribs. All parameters in the table are shown in Figure 3.5 - 3.8. To make the models more representative of real ribs, some parameters are kept constant, such as fillets and draft angle, which are necessary for casting. Without a draft angle, it would be difficult to release the mold from the housing after the aluminum has solidified since it is cast using high-pressure die casting. These and other dimensions that are the same through all models and simulations are shown in Figure 3.4.

Table 3.1: The dimensions (mm/°) of the base models.

Dimensions (mm/°)	M1 single	M1 single corner	M2 single	M1 double
X	120	240	120	-
X_1	-	-	-	120
X_2	-	-	-	120
Y	120	120	-	-
Y_1	-	-	60	120
Y_2	-	-	60	120
T	4	4	4	4
R	10 000	50	10 000	10 000
R1	-	-	-	10 000
R2	-	-	-	10 000
α_1	-	80	-	-
α_2	-	80	-	-
D	-	-	-	40
Angle	-	-	-	0.01

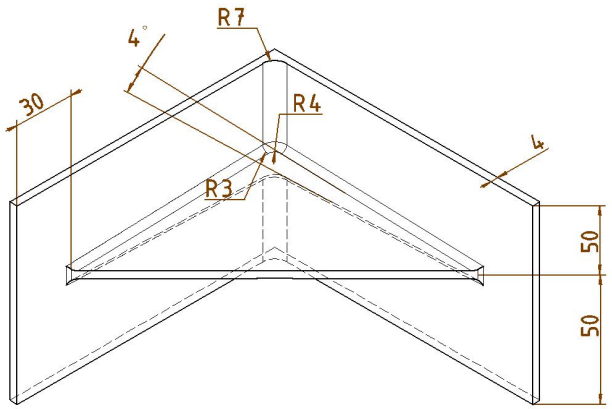

Figure 3.4: Drawing of model 1 single rib (M1 single) with the dimensions that are fixed.

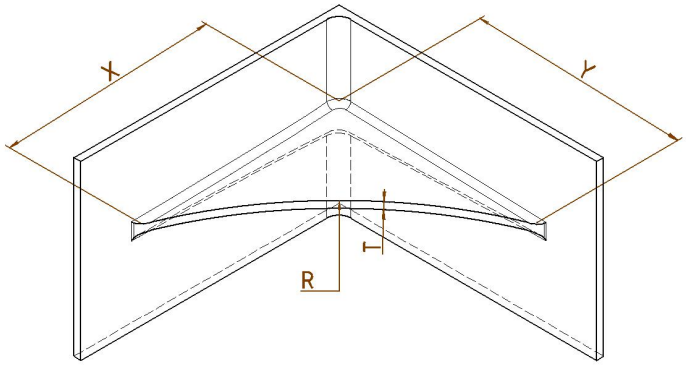

Figure 3.5: Drawing of model 1 single rib (M1 single) with the parameterized dimensions.

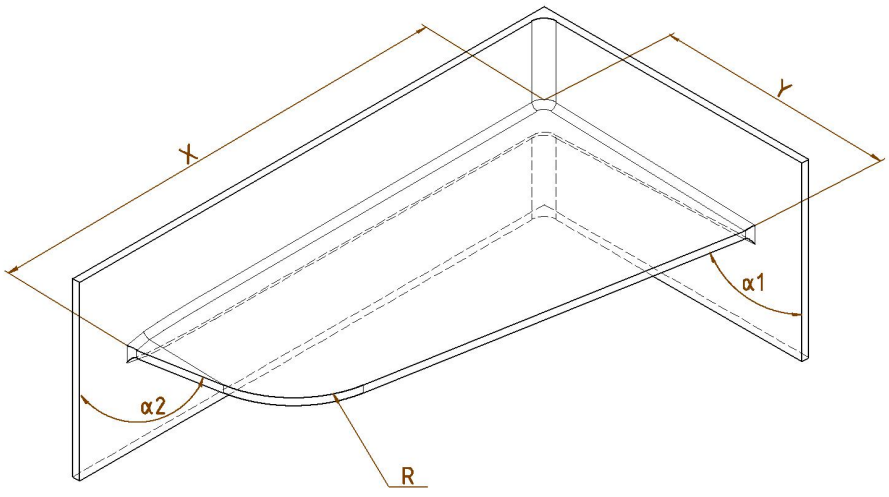

Figure 3.6: Drawing of model 1 single rib with corner (M1 single corner) with the parameterized dimensions.

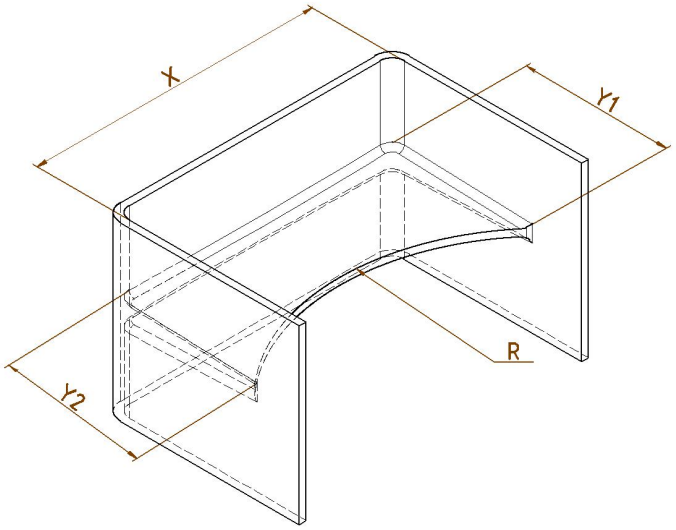

Figure 3.7: Drawing of model 2 single rib (M2 single) with the parameterized dimensions.

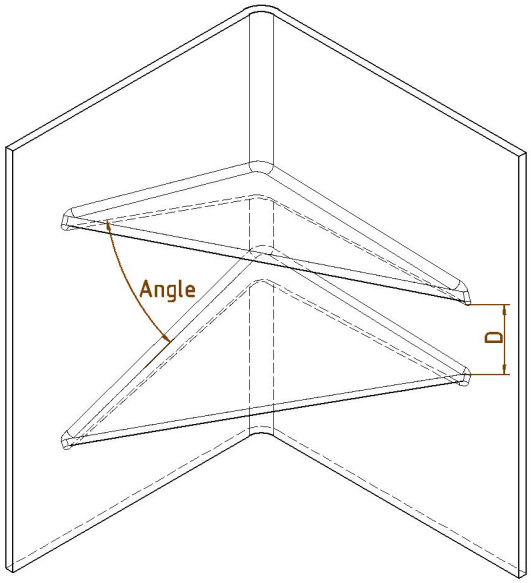

Figure 3.8: Drawing of model 1 double rib (M1 double) with the parameterized dimensions, the model also has the same parameterized dimensions as M1 single.

3.2 Verification of models and simulations

This sub-chapter will discuss the choice of boundary conditions, excitations of the rib, model dimensions, and which mesh was used.

3.2.1 Model dimensions

The dimensions of the model affect the modes and the radiated sound. It's, therefore, important to validate that the fixed dimensions of the models give modes at similar frequencies as the modes of the ribs on a complete EDU. Most of the fixed dimensions, shown in Figure 3.4, are similar to the dimensions on an EDU and are fixed due to manufacturability. However, when only looking at a "cutout" of the EDU housing, the stiffness of the model will be affected. The initial thought was, therefore, to make the "back" of the rib thicker, as shown in Figure 3.9a, to isolate the acoustic contribution from the rib. This resulted in mode 1 at 4908 Hz, which is not close to the measured value of a real, similar rib. Using 4 mm as in Figure 3.9b instead gives a more reasonable result of 3255 Hz for mode 1. Both models have a boundary condition that makes the surface of the boundary infinitely stiff, which makes the thicker model too stiff, while the thinner model is more representative of a real EDU housing due to the frequency of the first bending mode.

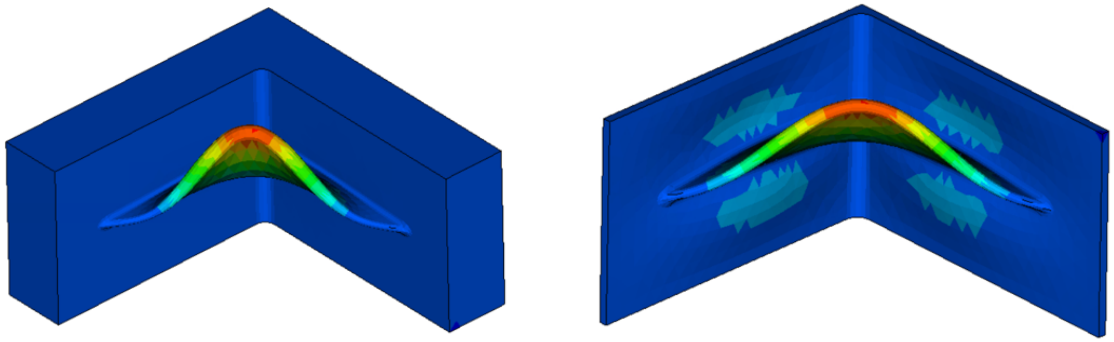

(a) Illustration of mode 1 at 4908 Hz with a 40mm back.

(b) Illustration of mode 1 at 3255 Hz with a 4mm back.

Figure 3.9: Comparison of the thickness of the back of the model and how it affects the mode frequency.

To avoid having separate models with no curvature on the ribs (no R), R was instead put to 10 000 mm. This meant that the edge of the rib in practice was straight and that 5 models could be used instead of 9 (M1 single corner has a different type R, see Figure 3.6). To verify that this gave the same result as a completely straight edge a comparison between the two was done for M1 single, see figure 3.10.

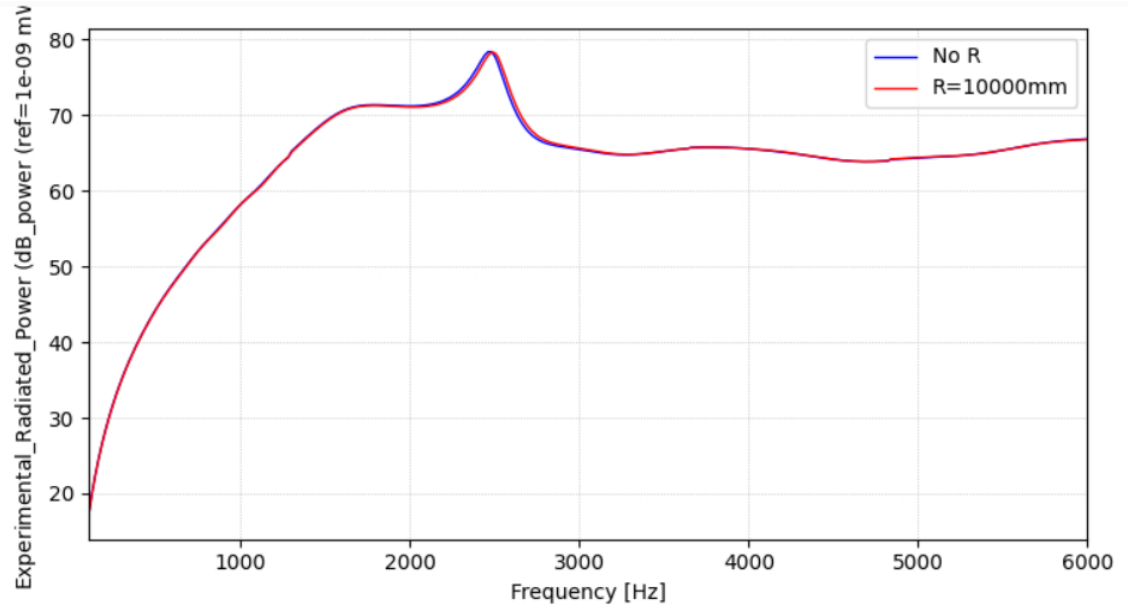

Figure 3.10: Comparison of model M1 single with no R and with R = 10 000 mm.

Based on figure 3.10, it can be concluded that R = 10 000 mm is a good approximation for a straight edge.

3.2.2 Excitations of the rib and boundary conditions

To find the most representative and repeatable way of exciting the ribs, three different methods were tested (each acting in the normal direction of the rib). These are a point load of 1 N in one node on the surface of the rib, a distributed load of 1 N on the boundary nodes, and a velocity of 1 mm/s on the boundary nodes, see Figure 3.16, of the rib structure. These different ways of excitation are based on a sinusoidal signal with an amplitude of one, 1 N, or 1 mm/s and with frequencies between 100 Hz and 6000 Hz.

The first method of exciting that was studied was a harmonic point load of 1 N acting in one of the nodes on the surface of the rib. The advantage of this method is that the results are easy to compare to experiments done on physical models since previous tests have been conducted in a similar way. To do such a test on a physical model, the rib is excited with a hammer with a load cell so that the input, the force, can be normalized to 1 N. The disadvantage of using this way of excitation is that the simulation has low repeatability and reproducibility since the results vary depending on which node the point load is acting on, which is shown in Figure 3.11. Furthermore, when changes to the geometry are done, the position of the nodes also changes, which makes the choice of which node to place the load on difficult. For this reason, a point load was excluded.

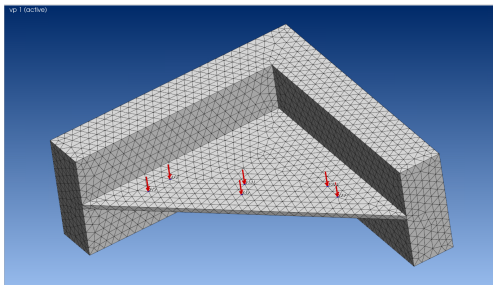

(a) Illustration of point loads acting on different nodes.

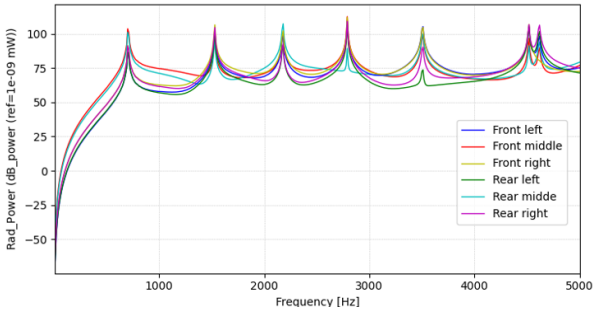

(b) Sound power levels in dB from the different point loads.

Figure 3.11: Illustration of how the result is affected by the placement of the point load.

The second form of exciting that was investigated was a harmonic distributed load over the boundary of the rib structure. The advantage of this form of excitation, contrary to the point load, is that the result will be independent of the rib's geometry since it will act on the boundary. But, the disadvantage is the fact that different ribs will have different masses which will affect how much each of the ribs moves. This is due to Newton's second law which states that the acceleration depends on both the force and mass of an object. Finally, this way of exciting is difficult to recreate experimentally which makes it difficult to compare the results from simulations and experiments. For these reasons, a distributed load was also excluded.

Finally, a velocity of 1 mm/s for the edge of the structure was chosen since this form of excitation is independent of the geometry and mass of the rib. This method can also be motivated by the fact that the mass of the rib is small compared to the whole EDU. This means that an individual rib will not affect the global movement of a complete EDU significantly. However, the disadvantage is the same as for the distributed load, it is difficult to reproduce in testing. However, it is a robust comparison between the different models.

The boundary condition used assigns an infinite stiffness to the boundary nodes of the structure. This was achieved by using the NASTRAN element RBE2, which defines rigid elements with a reference node to which the velocity condition is applied, see Figure 3.16.

3.2.3 First and second order mesh

Using linear (first order) mesh elements will cause the deformations to be under-predicted due to a too high prediction of stiffness [4]. To confirm this statement, acoustic simulations were performed for both linear and quadratic (second order) surface and solid mesh elements, see Figure 3.12. Important to note is that the surface (shell) mesh of the model is only used to map the nodal displacement to the acoustic mesh and is not used in the structural calculation.

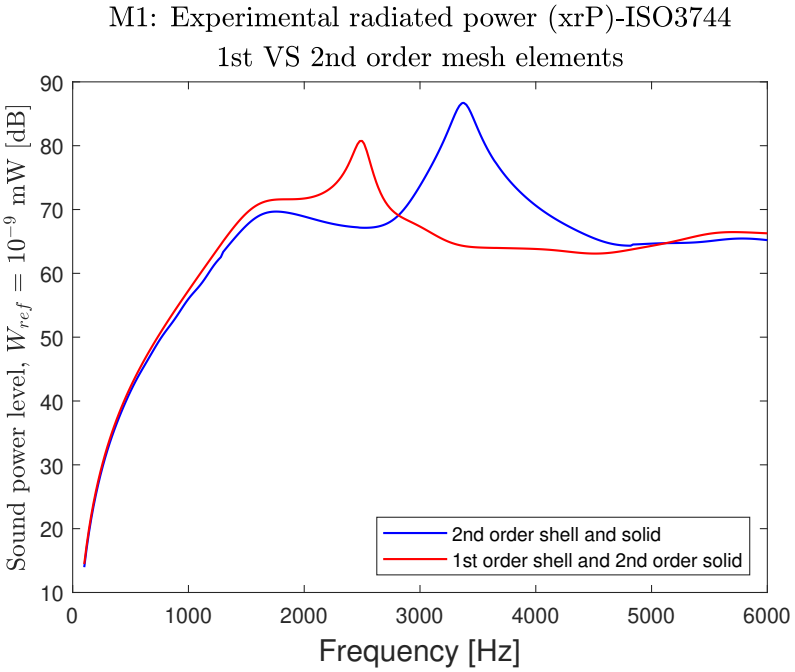

Figure 3.12: Radiated power from model 1 single rib with linear and quadratic surface (shell) and solid mesh elements.

It can be concluded from Figure 3.12 that using linear solid mesh elements will cause an overestimation of the structure's stiffness, which means that the behavior of the rib won't be captured correctly.

To compare the radiated power when using linear or quadratic surface mesh elements, to map the nodal displacement to the acoustic mesh, in combination with quadratic solid mesh elements, the two results are plotted in the same plot:

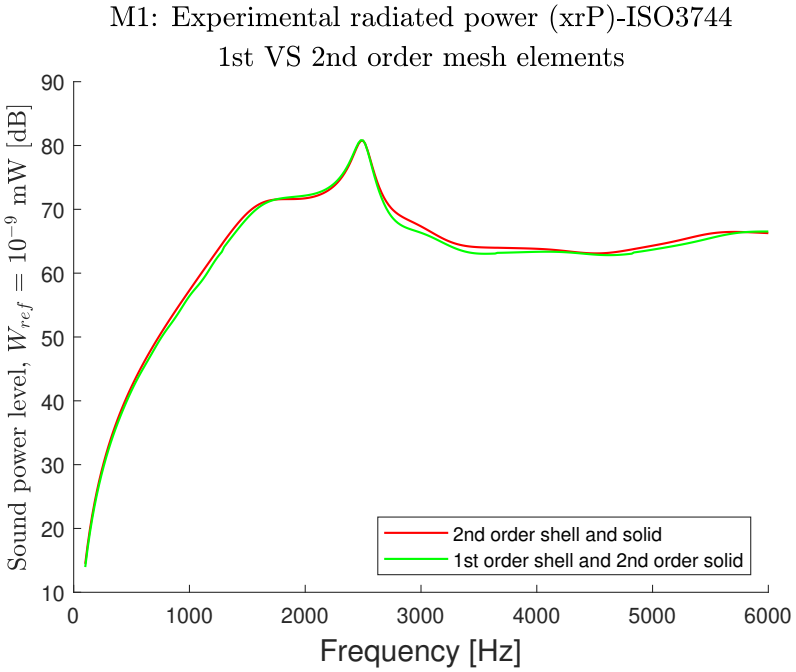

Figure 3.13: Comparison between linear and quadratic surface (shell) mesh elements in combination with quadratic solid mesh elements of the radiated power for model 1 single rib.

From Figure 3.13, it can be concluded that there is no significant difference when using linear or quadratic surface mesh elements to map the nodal displacements to the acoustic mesh when simulating the radiated acoustic power. Furthermore, when simulating with quadratic surface mesh elements the simulation time increases substantially compared to linear. Based on these observations, the combination of quadratic solid mesh elements and linear surface mesh elements was used for the acoustic simulations.

3.2.4 Mesh size

To find a good compromise between accuracy and simulation time, a mesh convergence study was done. Three different mesh sizes were tested to find the optimal mesh size for this study: 3 mm, 5 mm, and 8 mm. For each size, two tests were done, giving six tests in total, where one of the tests forced at least two elements, even if the model was thinner than the mesh size. The other test did not have that requirement. To compare the six different cases, the experimental radiated power was plotted for each of the six cases.

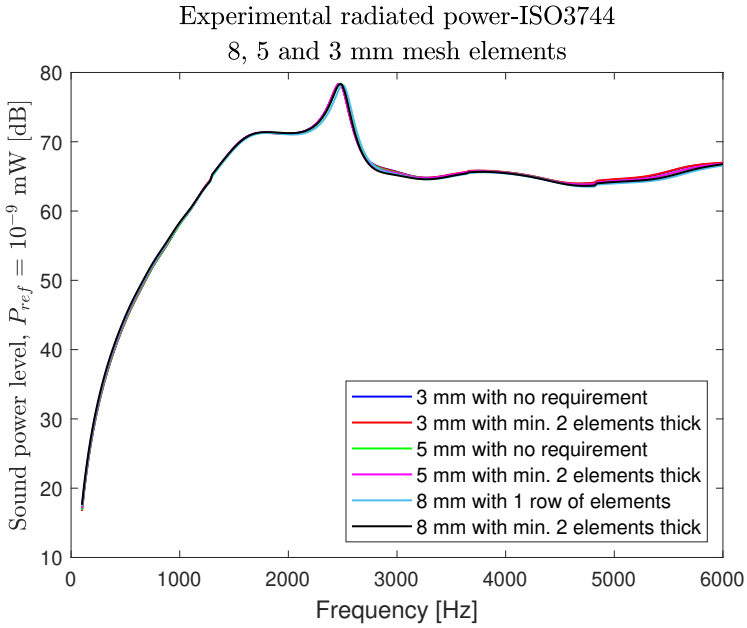

Figure 3.14: Mesh convergence study of experimental radiated power for sizes: 3 mm, 5 mm, and 8 mm.

From Figure 3.14, it is difficult to make out any differences, so the peak was investigated closer:

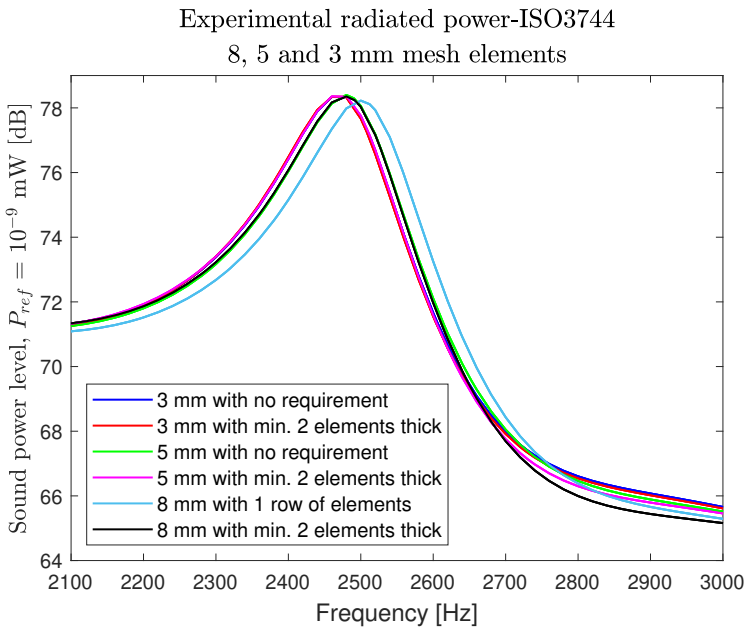

Figure 3.15: Mesh convergence study of experimental radiated power for sizes: 3 mm, 5 mm, and 8 mm (zoomed).

From Figure 3.14 and 3.15, it was concluded that a mesh size of 5 mm with the setting for minimum two elements per smallest thickness activated was a good compromise. This conclusion was drawn based on the small difference in the result from the 3 mm mesh elements and the substantially lower simulation time.

3.2.5 Verification of Actran results

To ensure that the results from Actran were relevant, a simple calculation was done by hand to verify that the radiation efficiency (σ) is calculated as expected, see Equation 2.14. The radiated power for the rib of M1 single base model (X=Y=120 mm) from BC Mesh peaks at a frequency of 2480 Hz with a value of 80.5598 dB ($W_{ref} = 10^{-9}$ mW), at this frequency the rib has a mean square velocity (mv) of 144.232 mm^2/s^2 and a radiation efficiency of 0.2394. These values are used in Equation 2.14 along with the area, $S = 15819$ mm^2, speed of sound, $c_0 = 340000$ mm/s, and the density of air, $\rho_0 = 1.225 \cdot 10^{-12}$ t/mm^3:

$$W_{ERP} = \frac{1}{2}\rho_0 c_0 S v^2 = \frac{1}{2} \cdot 1.225 \cdot 10^{-12} \cdot 3.4 \cdot 10^5 \cdot 15819 \cdot 144.232 = 0.4751 \text{ mW} \quad (3.1)$$

To calculate the radiation efficiency, the radiated acoustic power is also required, which is the radiated power from BC Mesh in this case. Since the equivalent radiated power (ERP) is expressed in mW, the radiated power has to be converted to mW as well. This is done in the following way:

$$P_{dB} = 10 \cdot \log_{10}\left(\frac{P}{P_{ref}}\right) \Longrightarrow P = P_{ref} \cdot 10^{P_{dB}/10} \quad (3.2)$$

In this case, the power in dB, $P_{dB}(P_{ref} = 10^{-9}$ mW), is equal to 80.834 dB, which equals 0.1138 mW. This equals a radiation efficiency of, according to Equation 2.15:

$$\sigma = \frac{W_{\text{BC Mesh}}}{W_{ERP}} = \frac{0.1138 \text{ mW}}{0.4751 \text{ mW}} = 0.2394 \quad (3.3)$$

Since the two values of the radiation efficiency match, the conclusion can be drawn that Actran calculates σ as expected when using BC Mesh.

3.3 Workflow

The workflow for the simulations can be broken down into five sub- steps, which will be described in detail. In short, these steps include modifying the parameterized model in CATIA V5, meshing the model in ANSA and applying the boundary conditions, calculating the displacements of the nodes in NASTRAN, visualizing the eigenmodes in META to identify which type of modes, and performing the acoustic simulations in Actran.

The first step is to open the model that will be analyzed in CATIA V5 and modify the base model accordingly to get the desired rib geometry. Only one parameter is changed at a time to see the effect of that specific parameter. These changes are listed in Tables 3.2 - 3.5 for each model including the span of the variation and the number of simulations within that span. For a more detailed list of the simulations, see Appendix A.3. When the changes are done, the model is saved as a CATPart, which is used as an input to ANSA.

Table 3.2: The span of the dimensions of the M1 single model.

dimensions (mm/mm^2/°)	span	number of simulations
X = Y	X/Y: 50 - 250	8
Area = 3600 with X ≠ Y	X: 50 - 80 / Y: 90 - 144	5
Area = 7200 with X ≠ Y	X: 60 - 240 / Y: 60 - 240	4
Area = 12800 with X ≠ Y	X: 80 - 160 / Y: 160 - 320	4
R	151 - 400	5
Area = 9750 with X = Y, R ≠ const.	X/Y: 150 - 170 / R: 262.7 - 532	4
Thickness, X=Y=100 mm	T: 2-6	5
Thickness, X=Y=120 mm	T: 2-6	5
Thickness, X=Y=130 mm	T: 2-6	5
Thickness, X=Y=140 mm	T: 2-6	5
Thickness, X=Y=150 mm	T: 2-6	5

Table 3.3: The span of the dimensions of the M1 single corner model.

dimensions (mm/mm^2/°)	span	number of simulations
α_1	28-80	8
α_2	70-90	4
R	20 - 116	6

Table 3.4: The span of the dimensions of the M2 single model.

dimensions (mm/mm^2/°)	span	number of simulations
X= $2Y_1 = 2Y_2$	X: 50 - 250	5
Area= 3600 with X= 100, $Y_1 \neq Y_2$	Y_1: 46 - 66 / Y_2: 6 - 26	3
Area= 7200 with X= 120, $Y_1 \neq Y_2$	Y_1: 70 - 90 / Y_2: 30 - 50	3
Area= 12800 with X= 160, $Y_1 \neq Y_2$	Y_1: 90 - 110 / Y_2: 50 - 70	3
R	62 - 200	7
Area= 5000 with X= $2Y_1$= $2Y_2$, R ≠ const.	X: 110 - 160 / R: 80.72 - 268.72	4

Table 3.5: The span of the dimensions of the M1 double model.

dimensions (mm/mm^2/mm^3/°)	span	number of simulations
X= Y, rib1= rib2	X: 50 - 200	4
X= Y, rib1≠ rib2, rib1= 120x120	X: 50 - 200	4
X= Y, rib1≠ rib2, rib1= 50x50	X: 50 - 200	4
X= Y, rib1≠ rib2, rib1= 200x200	X: 50 - 200	4
R, rib1= rib2	151 - 400	5
X= Y, rib1≠ rib2, rib1= R151	R: 151 - 400	5
X= Y, rib1≠ rib2, rib1= R10 000	R: 151 - 400	5
Area= 9750, volume= 390 000 with X= Y, R≠ const.	X/Y: 150 - 170 / R: 262.7 - 532	4
D, rib1= rib2	20 - 110	14
Angle, rib1= rib2	0 - 50	7
Volume= 288 000, rib1= rib2, X= Y, D≠ const.	X/Y: 90 - 150 / D: 27.89 - 81.63	5

In ANSA, the CAD model is converted to a surface model and meshed using the Batch mesh function with the following settings: second-order triangular mesh elements with a target size of 5 mm and a minimum length of 1 mm in combination

with force 2 rows of element per smallest thickness. The resulting surface mesh is exported using the NASTRAN format. The reason for exporting the surface mesh separately is to use it as a geometry input for Actran. Then, the volume mesh is created using tetra rapid with a maximum growth rate of 1.2 combined with a minimum of two elements per smallest thickness. The next step is to define a set of all the surface nodes for which the resulting displacements are calculated. Then, the RBE2 is defined, which uses the nodes on the boundary as slave nodes, which can be seen in Figure 3.16.

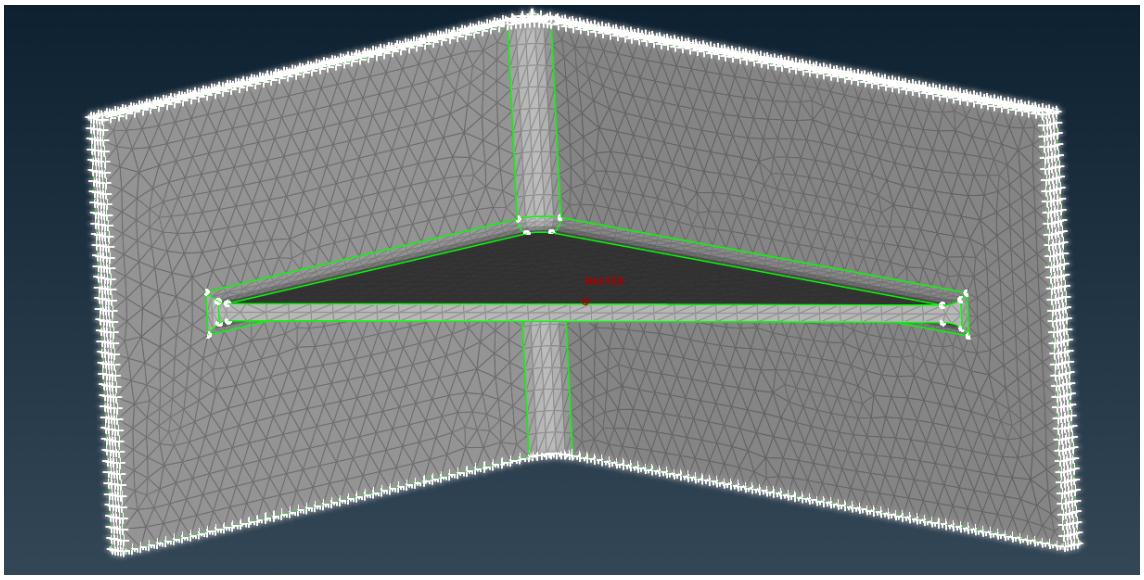

Figure 3.16: Visualization of the RBE2 in ANSA. The white nodes represent the slave nodes and the red node represents the master node.

The boundary condition is then applied in the master nodes by importing a NASTRAN header and merging it with the current model, see Appendix A.1 for more details. In short, the header contains the boundary conditions and the eigenmode solver. The last step is to define the material constants, aluminum in this case, which can be seen in Table 3.6 below:

Table 3.6: Material constants for aluminum used in the model.

Variable	Value
Density of aluminium	2700 kg/mm^3
Young's modulus of aluminium	70 GPa
Poisson's ratio of aluminium	0.33

Finally, the complete model is exported using the NASTRAN format.

When the model is defined in ANSA, the nodal displacements are calculated in NASTRAN and visualized in META to identify which of the modes are bending modes and find the corresponding frequency, an example of this can be seen in Figure 3.17.

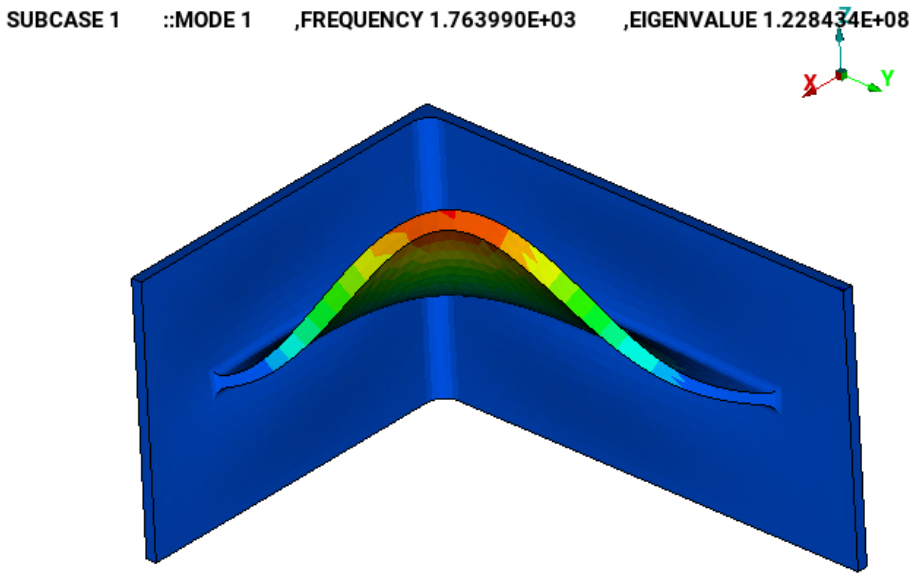

Figure 3.17: Visualization of how the modes were characterized in META. In this example, the first bending mode with a frequency of 1764 Hz.

Finally, when the model is defined in ANSA and the nodal displacement is calculated, the model in Actran can be defined. The surface mesh that was exported separately from ANSA was used as the input mesh, and the elements were interpolated to first-order elements. This was done to save on the computational time but gives comparable results to using a second-order surface mesh, see Figure 3.13. After the mesh was imported, it was split into two domains, the rib and the remaining surface, denoted as the back. This was done to isolate the acoustic contribution from just the rib, making the comparisons more relevant since a bigger rib also has a bigger back structure compared to a smaller rib. The Actran analysis was done by performing a direct frequency response, which uses the frequencies that were used to calculate the nodal displacements in NASTRAN, 100 Hz to 6000 Hz, with 20 Hz steps. In addition to the 20 Hz steps, five extra points around the modes were also calculated to improve the accuracy around the modes, see Appendix A.1. When the frequencies of the direct frequency response are defined, the exterior acoustic component is defined, which creates the mesh that models the free field radiation (in this case, air). This function also adapts the mesh according to the frequencies of the analysis decreasing the mesh size for increasing frequencies. In this component, the near-field definition is also controlled, and it is defined as a thickness of 700 mm with a minimum of six elements per wavelength. It also includes the far field definition, which uses infinite elements to model the far field with an interpolation order of 10. The air was defined by two variables, the speed of sound, which was set to $3.4 \cdot 10^5$ mm/s and a density of $1.225 \cdot 10^{-12}$ t/mm^{-3}. The nodal displacements calculated previously are imported and applied using the function BC Mesh, which maps the nodal displacements to the fluid (the air). The reason why the displacements were calculated separately is that Actran didn't have the necessary functions to perform velocity excitations. The function BC Mesh also gives data, such as velocity and radiation efficiency (σ) of the rib. By applying BC Mesh on the rib, the back of the rib, and the whole model, each domain can be analyzed separately. Finally,

the function Experimental Radiated Power is used to create a spherical microphone array (40 microphones) according to ISO3744 [7], 1 m away, which calculates the experimental radiated power (xrP). For the complete list of settings in Actran, see Appendix A.2. The results, the radiation efficiency (σ), the mean square velocity (mv), the radiated power (rP), and the experimental radiated power (xrP), are saved and plotted in MATLAB.

4

Results and observations

This chapter presents the results and observations from the simulations performed. The most important measurement is the simulated experimental radiated power (xrP), denoted as radiated power in the figures since these measurements have been simulated according to ISO3744, which is commonly used when performing acoustic measurements. Unless explicitly stated, each dB value is given based on the same reference value, $W_{ref} = 10^{-9}$ mW. Furthermore, no weighting curves were applied to the results from the simulations. Finally, the radiation efficiency is also important since it has been observed to affect the radiated power significantly.

4.1 Model 1- Single rib (M1 single)

4.1.1 M1 single base model

The base model, X=Y=120 mm and R=10 000 mm, has the following radiated power (xrP):

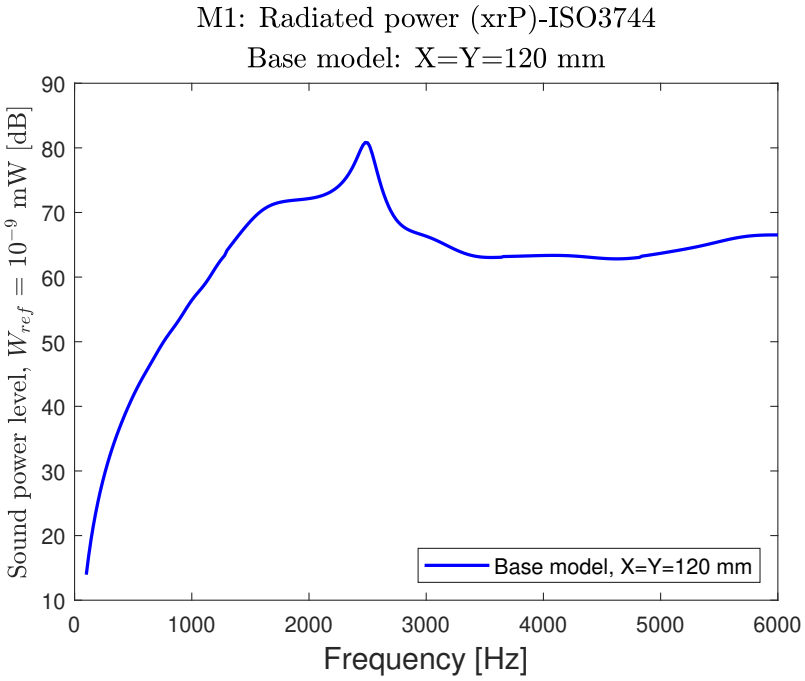

Figure 4.1: Radiated power of M1 single base model (X=Y=120 mm)

From Figure 4.1 it can be observed that the base model has one peak in radiated power at 2480 Hz, corresponding to the structure's first bending mode. To further investigate the acoustic performance of the base model, the radiation efficiency and mean square velocity of the rib were also plotted:

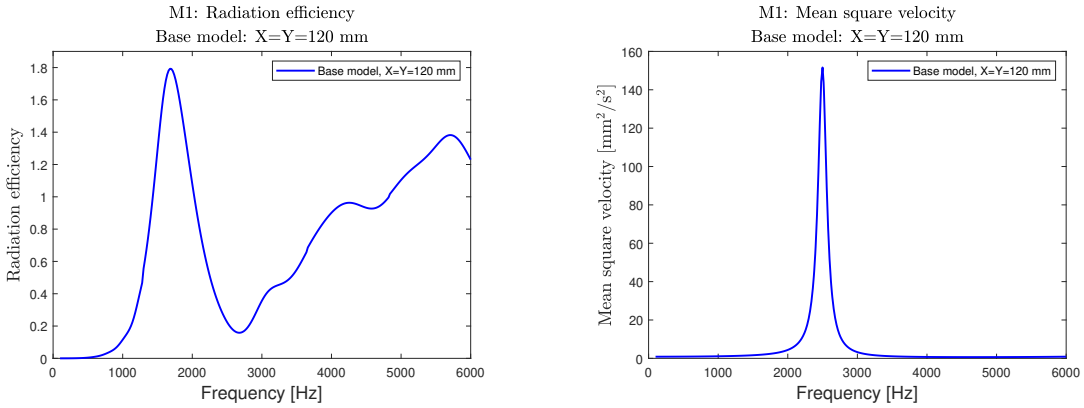

(a) Radiation efficiency. **(b)** Mean square velocity.

Figure 4.2: Radiation efficiency and mean square velocity of M1 single base model (X=Y=120 mm).

From Figure 4.2b, it can be concluded that the highest mean square velocity occurs at the first bending mode, 2480 Hz. This has been shown to be the case for all types of single rib models, while the double rib model can have two peaks because the two ribs can have their first bending mode at different frequencies. While the peak velocity can vary, the effect of the difference in velocity from one variation to another on W_{ac} in equation 2.16 is still small compared to the radiation efficiency. This is caused by the fact that the radiation efficiency at the first bending mode can differ significantly more than the velocity for variations of the same model. For this reason, the radiated power and radiation efficiency are the most interesting measurements to study. All velocity plots and plots of the radiated power normalized by the area of the rib structure, see Figure A.7 for the definition of the rib surface, for all simulations are shown in appendix A.4.

4.1.2 Area variation

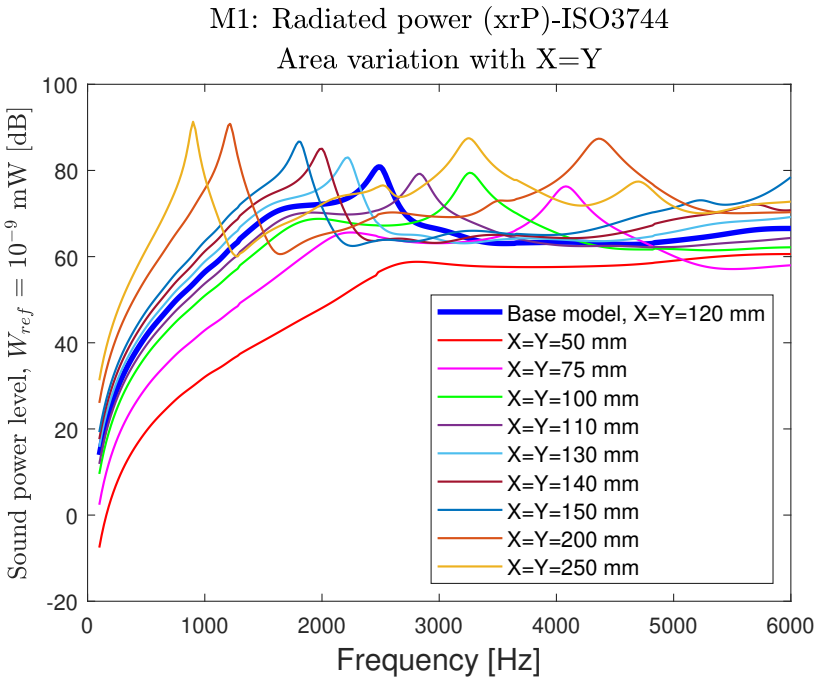

Figure 4.3: Radiated power for area variation of M1 single.

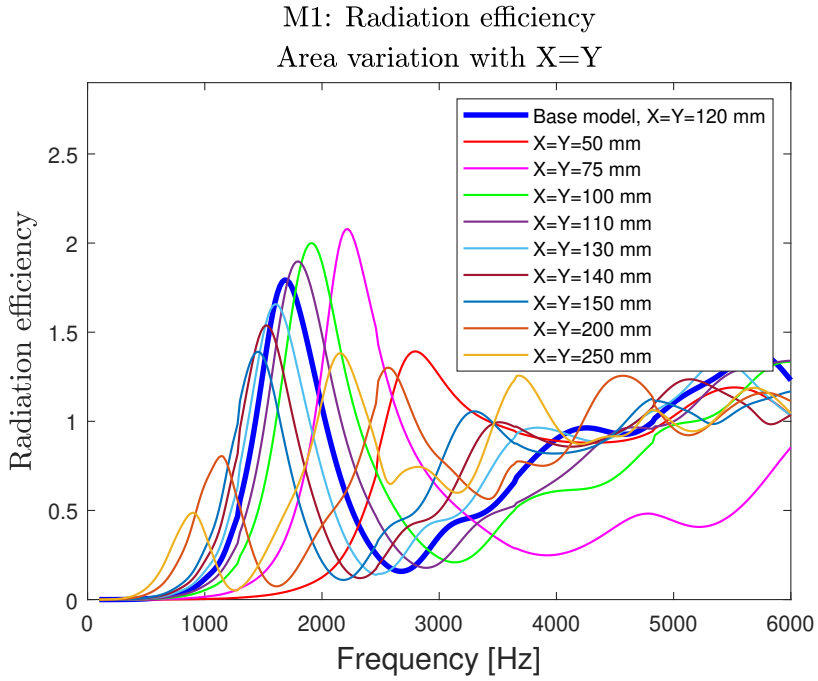

Figure 4.4: Radiation efficiency for area variation of M1 single.

From Figure 4.3 and 4.4, it can concluded that a rib with smaller dimensions has their peak in both radiated power and radiation efficiency at higher frequencies compared

to a larger rib, see A.3.1.1. In terms of radiated power, it can be explained by the fact that a larger rib's first bending mode has a lower frequency compared to a smaller one. The same behavior can be observed for the radiation efficiency, the reason however is not obvious. It can also be concluded from Figure 4.3 that a rib with a larger area has higher sound radiation compared to a smaller one. This is to be expected, see Equation 2.16, as the radiated sound is proportional to the surface area of the rib. Also, a larger rib has a higher mean square velocity which also increases the sound radiation. However, there are some results which do not follow this trend perfectly. If comparing X=Y=250 mm with X=Y=200 mm, there is only a difference of about 0.5 dB, and X=Y=100 mm is about 0.2 dB higher than X=Y=110 mm. This is because the radiation efficiency is higher at the first bending mode for X=Y=200 mm compared to 250 mm and for X=Y=100 mm compared to X=Y=110 mm.

4.1.3 Constant area

To investigate the impact of changing X and Y while having a constant area, three different areas were tested: 7200 mm^2 (same area as the base model), 3600 mm^2, and 12800 mm^2. Important to note that the areas are based on $\frac{1}{2}$XY, in the case of triangular ribs, which gives the area of one side of the rib, which is not the same area as S in Equation 2.16. This is because S includes the top, the bottom, the side of the rib, and the curved corners, see Figure A.7.

4.1.3.1 7200 mm^2

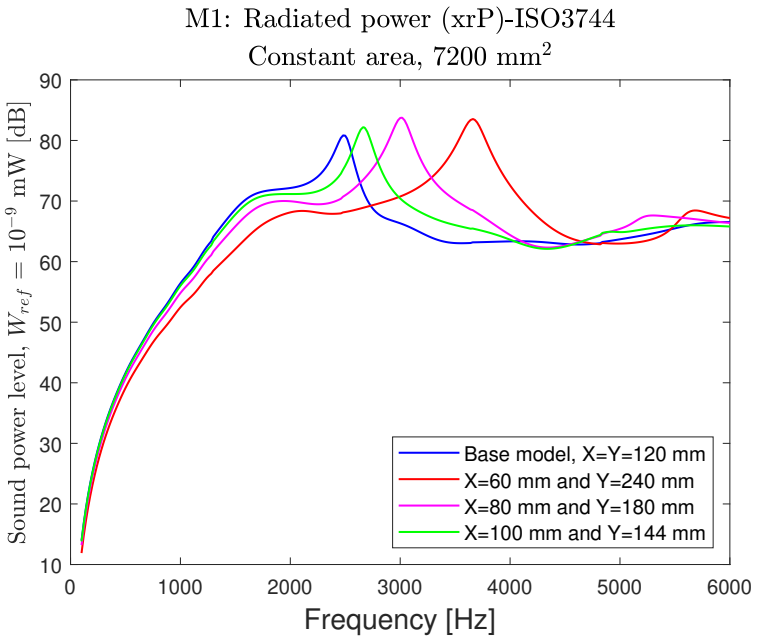

Figure 4.5: Radiated power for different dimensions and constant area (7200 mm^2) of M1 single.

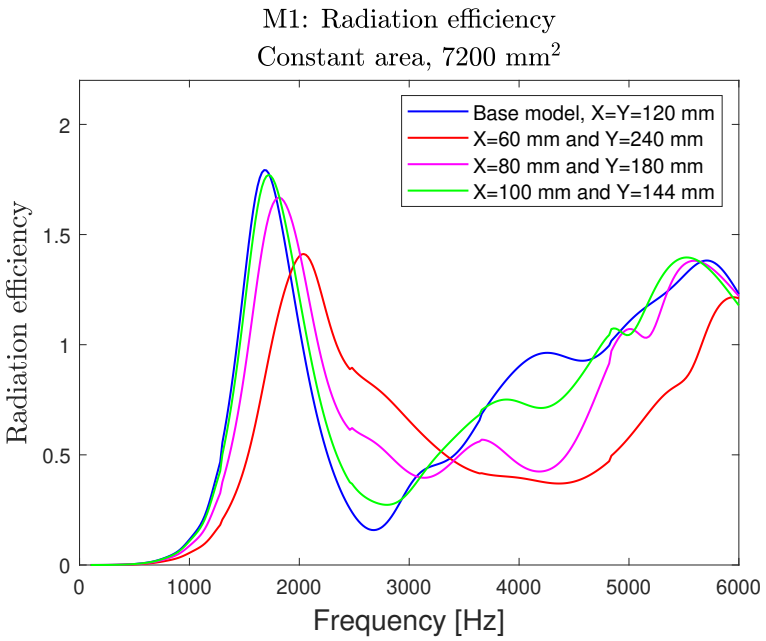

Figure 4.6: Radiation efficiency for different dimensions and constant area (7200 mm^2) of M1 single.

4.1.3.2 3600 mm^2

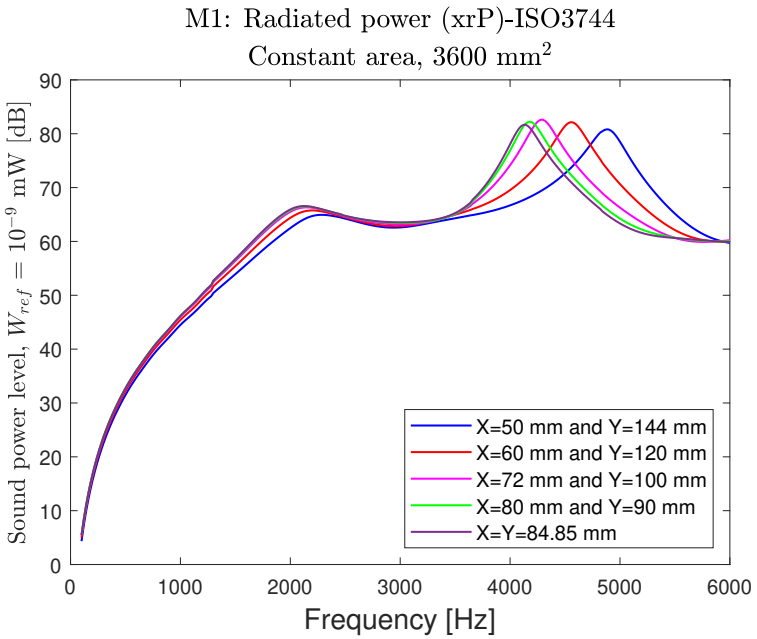

Figure 4.7: Radiated power for different dimensions and constant area (3600 mm^2) of M1 single.

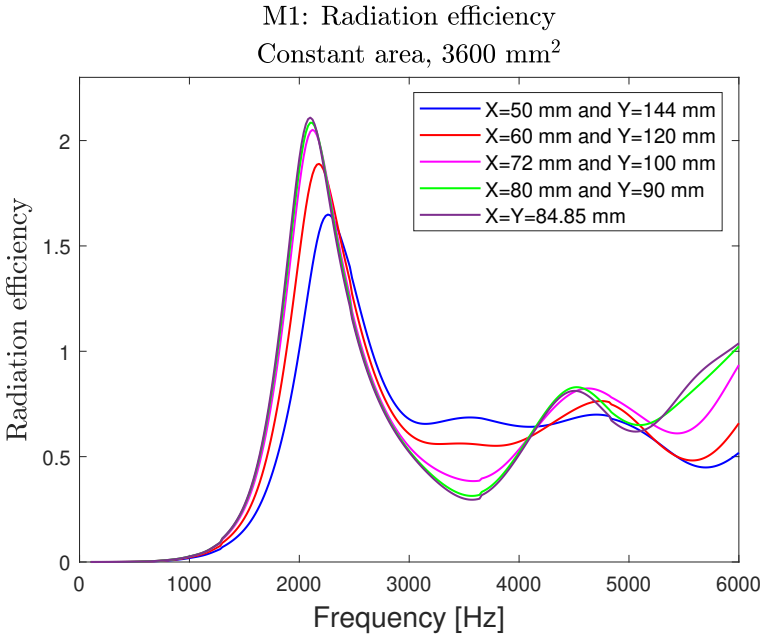

Figure 4.8: Radiation efficiency for different dimensions and constant area (3600 mm^2) of M1 single.

4.1.3.3 12800 mm^2

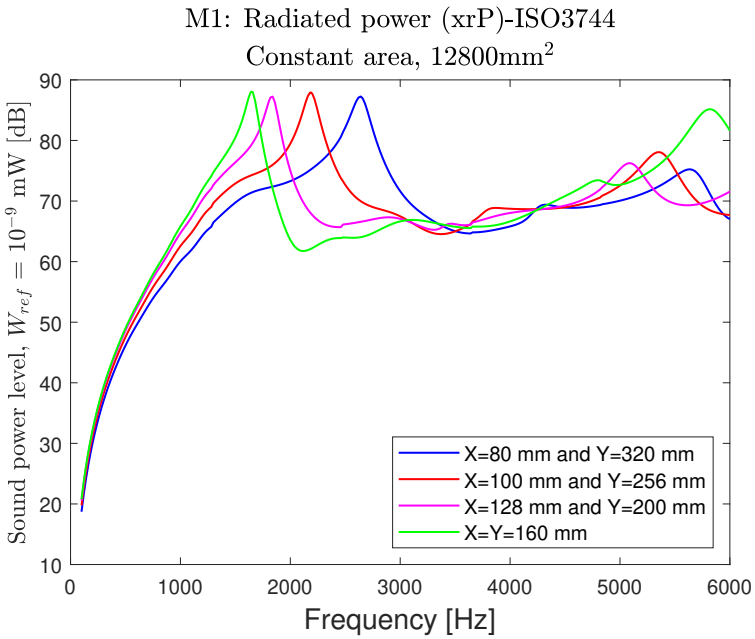

Figure 4.9: Radiated power for different dimensions and constant area (12800 mm^2) of M1 single.

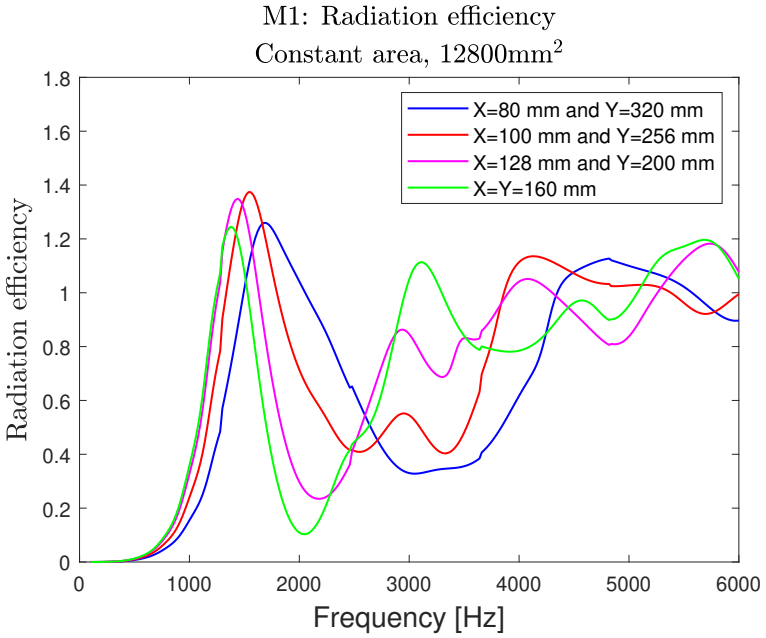

Figure 4.10: Radiation efficiency for different dimensions and constant area (12800 mm^2) of M1 single.

It can be concluded from Figure 4.5 - 4.10, that both the peaks in radiated power and radiation efficiency increase in frequency as the length in the y-direction increases. This may be caused by the fact that the draft angle acts in the y-direction, which, for an increased length, increases the rib's average thickness. The increased thickness of the rib causes it to become stiffer, which in turn increases the frequency of the first bending mode, see Appendix A.3.1.2. In terms of the values of the peaks in radiated power, there is no clear pattern between the variation of X and Y and the maximum sound power level. Since an increase of the length in the y-direction, for the ribs with an area of 7200 mm^2 the maximum radiated power increases, while for 3600 mm^2, the power decreases, and for 12800, the power does not change much for the different ribs.

In hindsight, simulations, where X is larger than Y, should have been performed instead of only ribs where Y is larger than X. Another alternative could've been to do these simulations without a draft angle. By performing these simulations as well, it is possible that a trend could have been observed.

4.1.4 R variation

The impact of adding a curvature to the outer edge of the rib was investigated by using the same dimensions as the base model, X=Y=120 mm, and changing the radius of the curvature. This was done for five different radii and then compared to the base model with a radius of 10 000 mm.

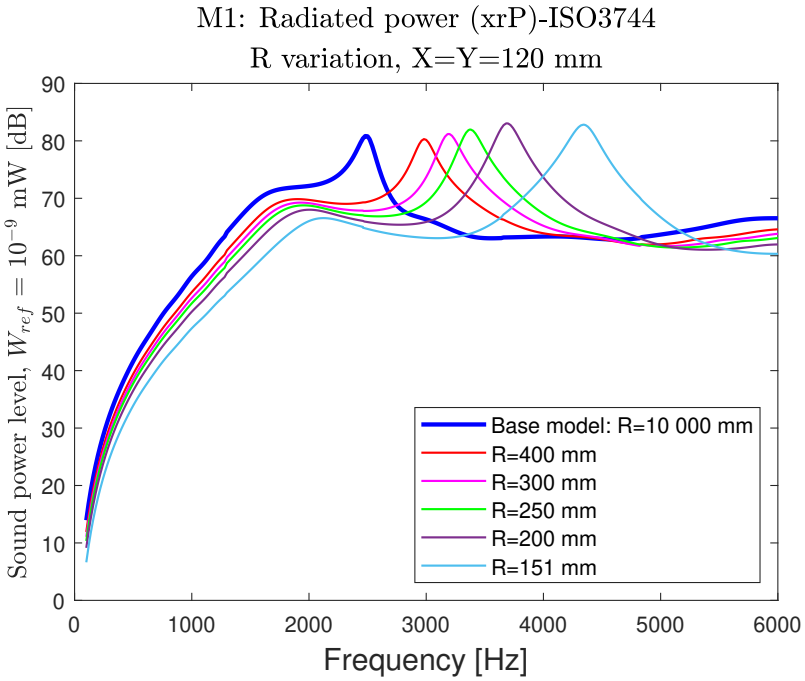

Figure 4.11: Radiated power for radius variation of M1 single.

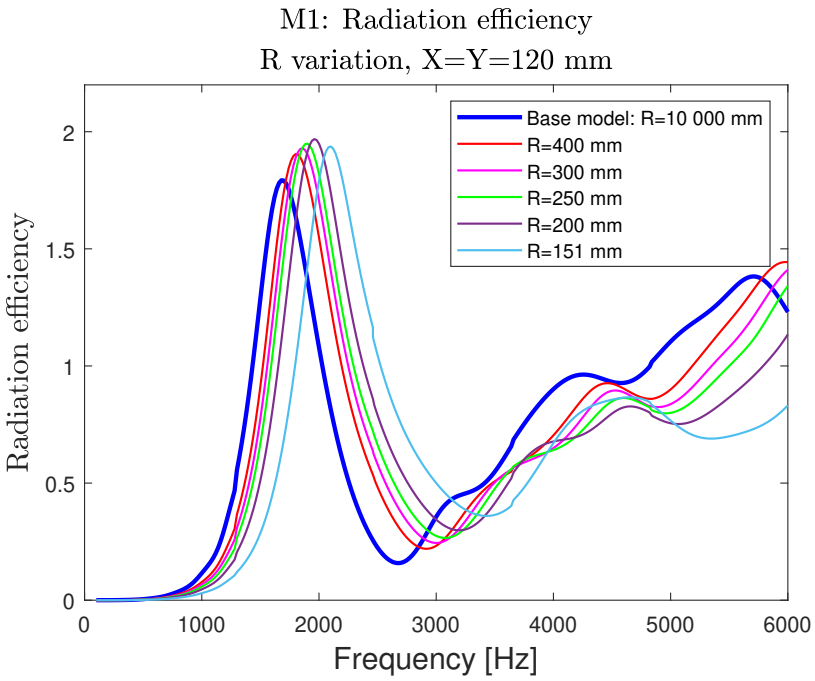

Figure 4.12: Radiation efficiency for radius variation of M1 single.

Notable from Figure 4.11 and 4.12, is the fact that a smaller radius causes the peak in radiated power and radiation efficiency to increase in frequency. There seems to also be a trend between the radius and the maximum peak value in radiated power, where a smaller radius results in a slightly higher peak in radiated power. This resulted in a difference of around 2 dB in maximum radiated power between R=10 000 mm and R=151 mm. This can be explained by the fact that the radiation efficiency has a higher value for the frequency of the first bending mode for ribs with a smaller radius. However, when comparing R=10 000 mm and R=400 mm, there is a decrease of around 0.5 dB in the maximum radiated power. To confirm that adding a small curvature while keeping the area almost identical can decrease the maximum radiated power, a second test was performed where X=Y=150 mm and R=10 000 mm was compared to X=Y=150 mm and R=532 mm:

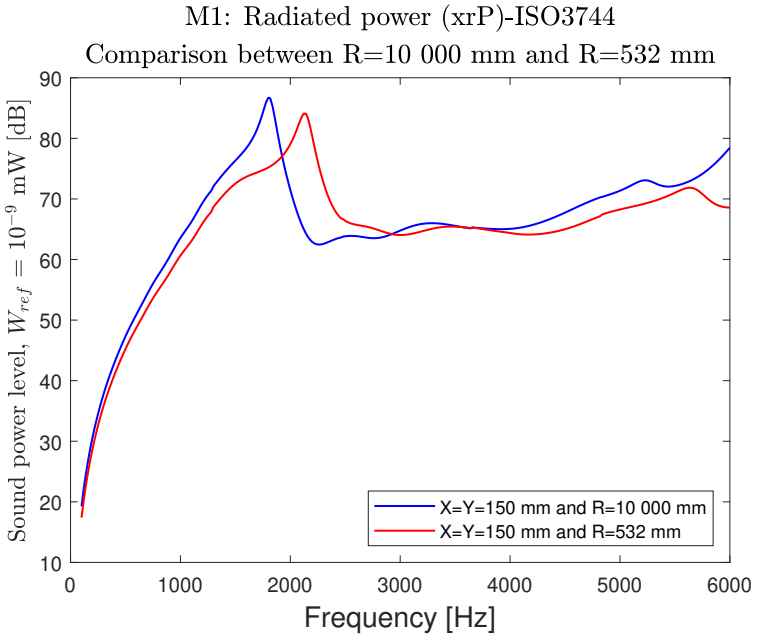

Figure 4.13: Comparison between the radiated power of R=10 000 mm and R=532 mm for a rib with equal dimensions (X=Y=150 mm).

From Figure 4.13 it can be concluded, that adding a small curvature to the rib, barely visible to the naked eye when looking at the model, see Figure 4.14, will decrease the radiated power. Since the curvature is so small, the area decreases with about 12 %, from 24 222 mm^2 to 21 358 mm^2, which does not explain the reduction in the radiated sound alone, see Equation 2.16. In this case, the maximum radiated power decreases by around 3 dB.

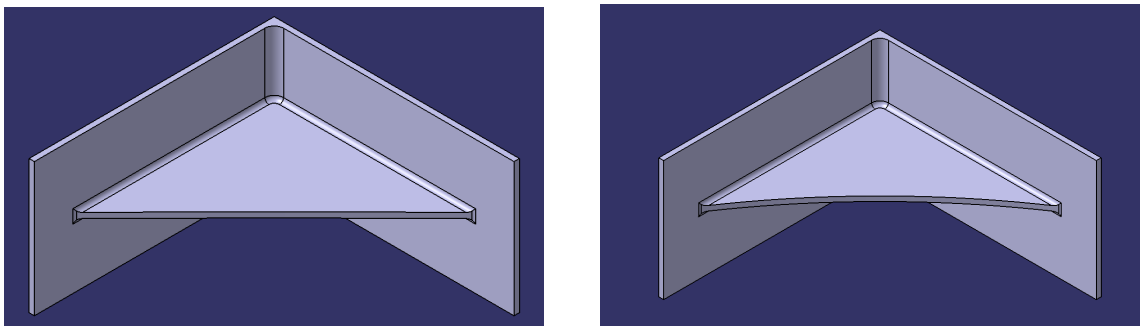

(a) X=Y=150 mm and R=10 000 mm. **(b)** X=Y=150 mm and R=532 mm.

Figure 4.14: Visual comparison between a rib with X=Y=150 mm with two different radii of the curvature on the outer edge, 10 000 mm and 532 mm.

Since the decrease in area does not fully explain the reduction in the radiated power, the radiation efficiency has to be studied. From Figure 4.15a, it can be observed that the radiation efficiency is lower for the rib with a radius of 532 mm than for the rib with a radius of 10 000 mm. Furthermore, the mean square velocity is also lower for the rib with R=532 mm compared to the rib with R=10 000 mm, see Figure 4.15b.

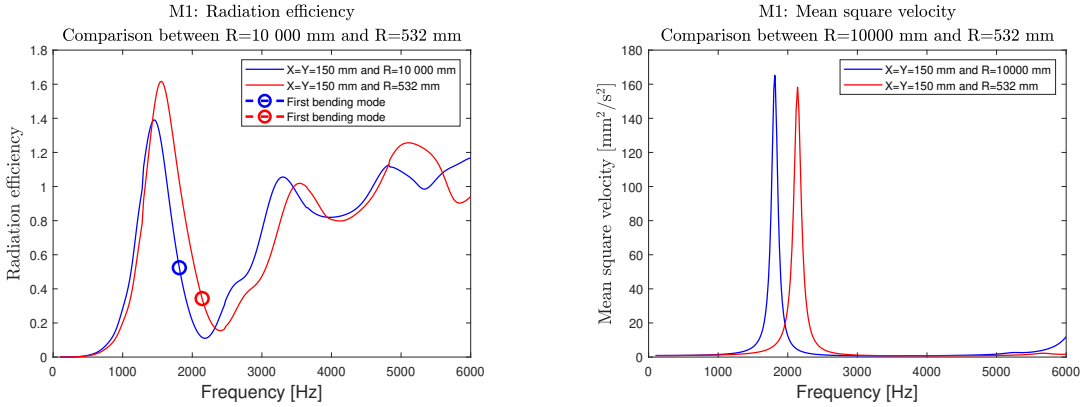

(a) Radiation efficiency. **(b)** Mean square velocity.

Figure 4.15: Comparison between the radiation efficiency and the mean square velocity of ribs with X=Y=150 mm and R=10 000 or R=532 mm.

In summary, the reduction of the radiated power can be explained by both the slightly smaller area, the radiation efficiency, and the mean square velocity. This is an important finding since adding a small curvature to the outer edge will likely not significantly affect the stiffness of the rib, which makes it easier to implement compared to changing the area of the rib.

4.1.5 Constant area different R

To further investigate the effect of different curvatures on the outer edge, a test was done in which the area is kept constant by changing both the dimensions of the rib

(X=Y) and R. The area is kept constant by using a smaller R to compensate for an increased length in X and Y.

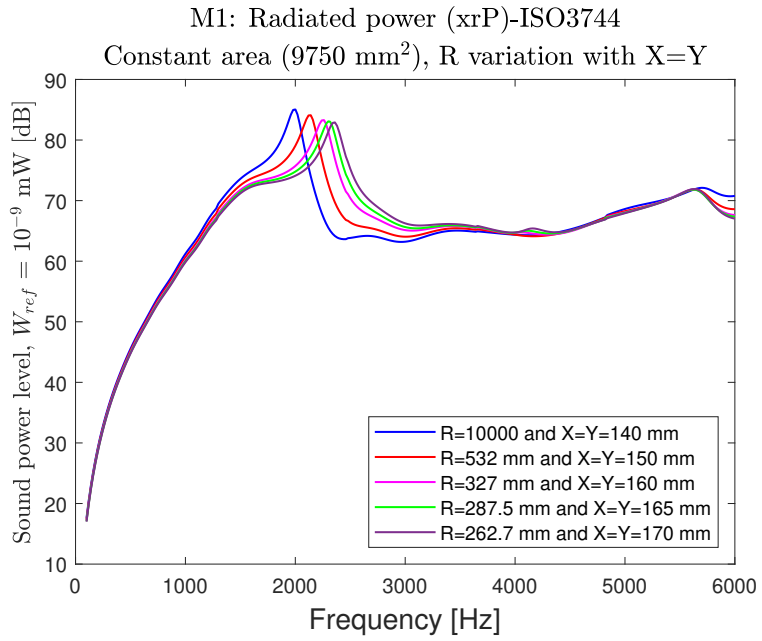

Figure 4.16: Radiated power for constant area with different dimensions, X and Y, and radii of M1 single.

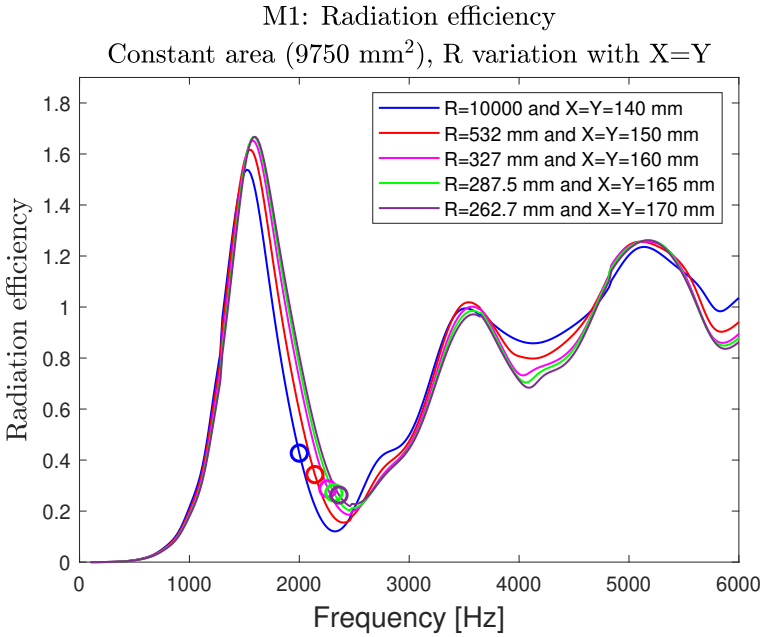

Figure 4.17: Radiation efficiency for constant area with different dimensions, X and Y, and radii of M1 single. With the frequency of the corresponding first bending modes marked with circles.

From these simulations with constant area for ribs of different sizes and different curvatures, it can be concluded that a larger rib with a larger curvature has a lower

maximum radiated power compared to a smaller rib with a smaller curvature. From Figure 4.16 this trend can be observed, with a decrease of around 2 dB between the smallest rib compared to the largest. In terms of the radiation efficiency, see Figure 4.17, the peaks for the different ribs have similar frequencies, while the frequency of the first bending modes for the different ribs increases, see A.3.1.4. This causes a reduction in the radiated power since the radiation efficiency will be lower for a larger rib due to the increased frequency of the corresponding first bending mode, see Figure 4.17.

4.1.6 Constant area, 7200 mm^2, with no draft angle

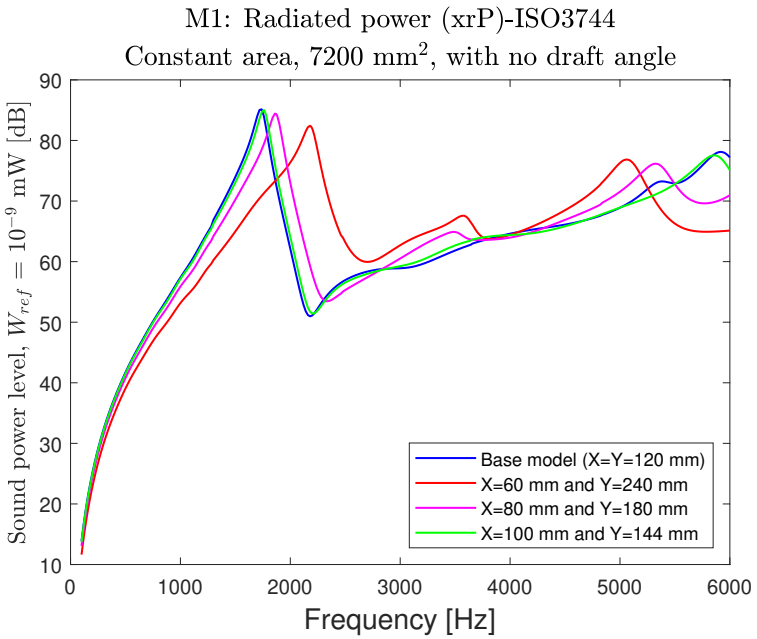

Figure 4.18: Radiated power for constant area, 7200 mm^2, with different dimensions, X and Y of M1 single and no draft angle.

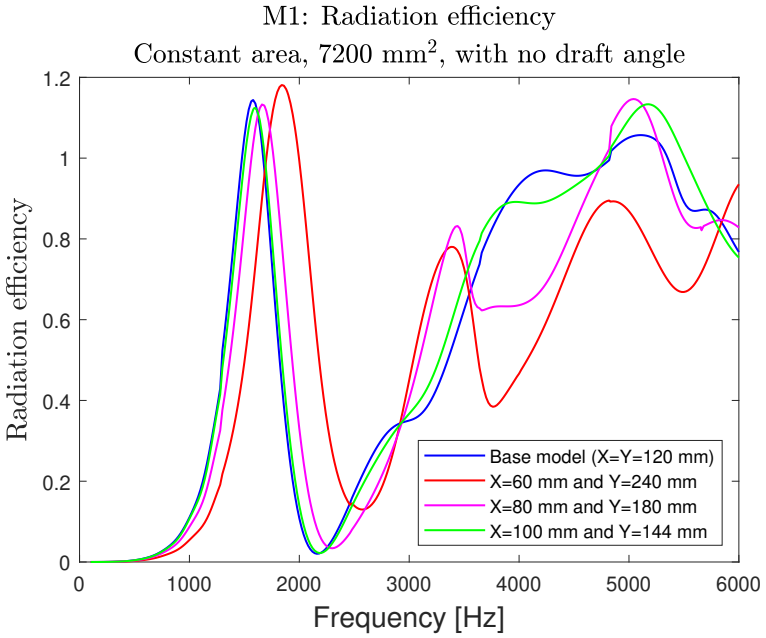

Figure 4.19: Radiation efficiency for constant area, 7200 mm^2, with different dimensions, X and Y of M1 single and no draft angle

From Figure 4.18 and 4.19, it can be concluded that it seems to be a trend that increasing the length in y-direction causes the frequency of the peaks in radiated power and radiation efficiency to increase. This is the same behavior as observed in Figure 4.5 - 4.10, but compared to the ribs with a draft angle, the shift in frequency of the peaks is not as great. In terms of the radiated power, when there is no draft angle, the radiated power decreases with an increased length in the y-direction, but when there is a draft angle, the radiated power increases for the constant area of 7200 mm^2.

4.1.7 Rib thickness variation with no draft angle

To try and find a relationship between the thickness of the rib and the dimensions of the rib, five different dimensions and thicknesses were investigated. These simulations were done with ribs with no draft angle to have a constant thickness across the ribs. The ribs did not have a curvature (R=10 000 mm) on the outer edge. The back structure had the same thickness, 4 mm, for all tests. This was done for five thicknesses and five different dimensions (X=Y): 100 mm, 120 mm, 130 mm, 140 mm, and 150 mm.

4.1.7.1 X=Y=100 mm

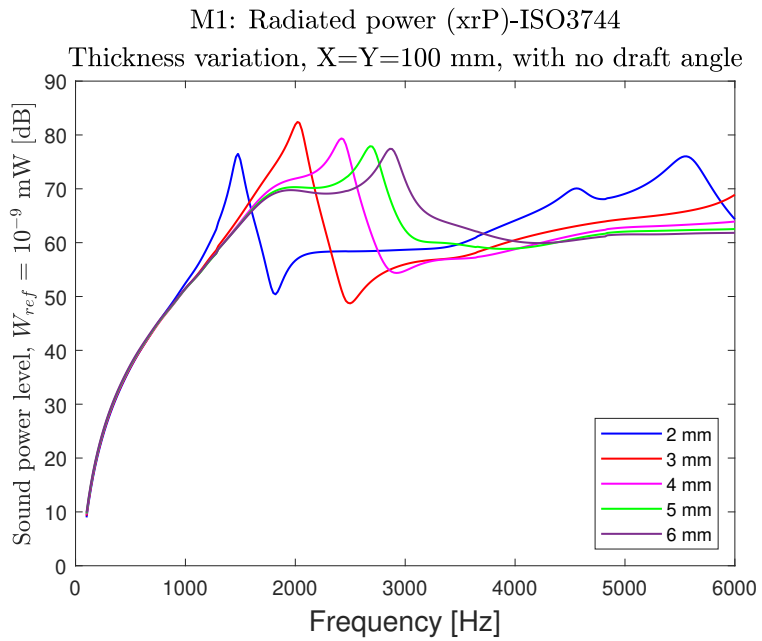

Figure 4.20: Radiated power for M1 single with X=Y=100 mm with varying thickness and no draft angle.

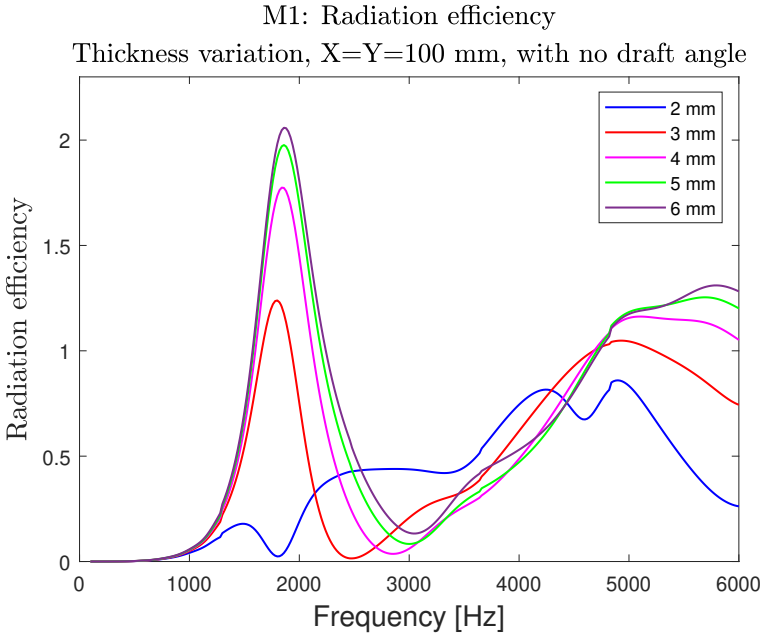

Figure 4.21: Radiation efficiency for M1 single with X=Y=100 mm with varying thickness and no draft angle.

4.1.7.2 X=Y=120 mm

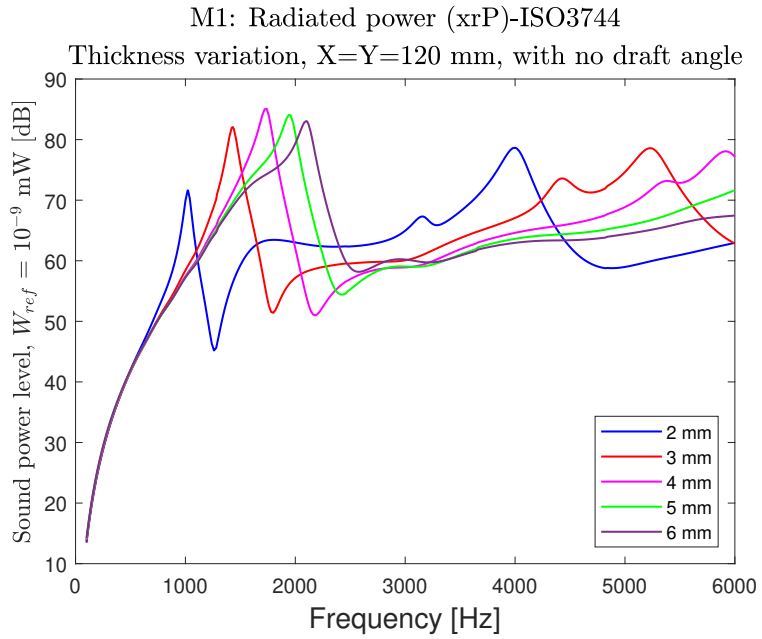

Figure 4.22: Radiated power for M1 single with X=Y=120 mm with varying thickness and no draft angle.

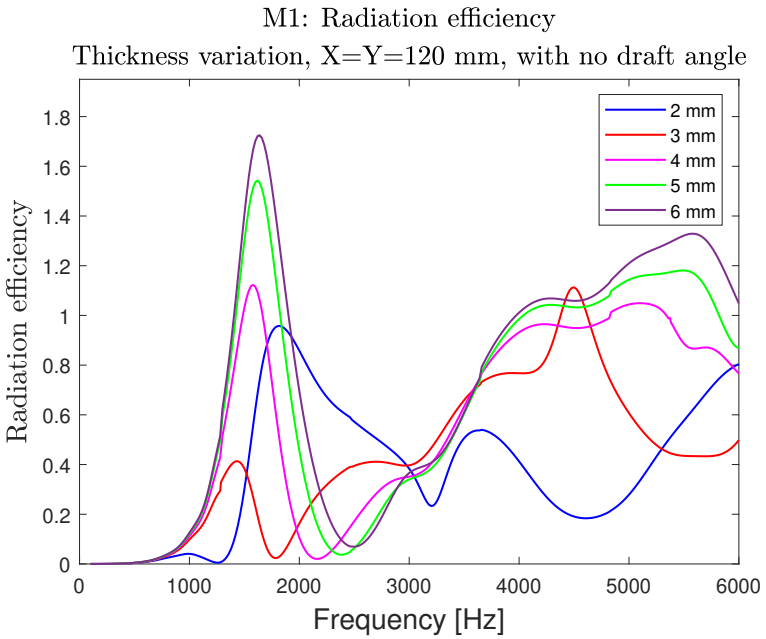

Figure 4.23: Radiation efficiency for M1 single with X=Y=120 mm with varying thickness and no draft angle.

The behavior of X=Y=130 mm, X=Y=140 mm, and X=Y=150 mm is similar but the thickness which has the highest radiated power increase as the dimensions increase, see Figures A.26, A.30, and A.34.

It can be noted from Figures 4.20 - 4.23 and A.26 - A.34 that there is always a thickness that has a higher peak in the radiated power than the others thicknesses for each dimension. It can also be noted that the thickness with the highest radiated power is increased when the size of the rib is increased. The reason for the higher radiated power is the fact that there is a better match between the frequency of the first bending mode and the radiation efficiency.

4.2 Model 1 corner- Single rib (M1 single corner)

4.2.1 Angle variation

For these simulations, the angles α_1 and α_2 were varied, one at a time. The other dimensions of the rib, X=240 mm, Y=120 mm, and R=50 mm, were fixed, and the angle not being varied was fixed at 80°. A smaller α_1 or α_2 makes the rib resemble a triangle rather than the shape of the base model which is rectangular, see Figure 4.24 below.

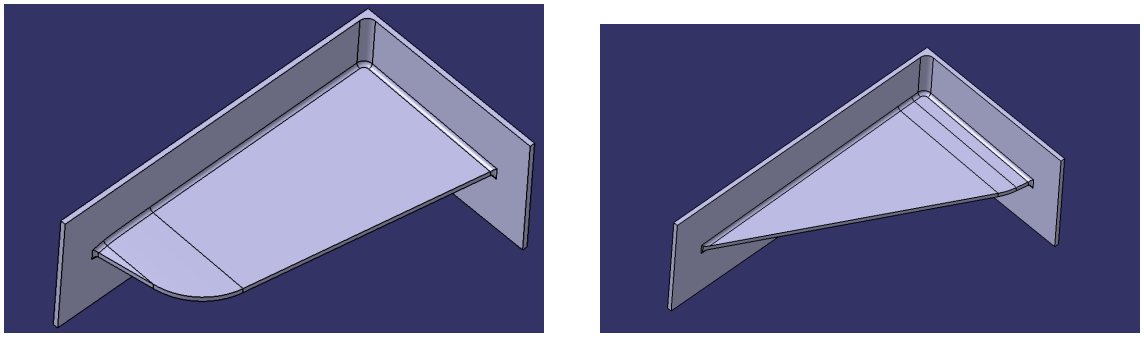

(a) $\alpha_1 = 80°$, base model. **(b)** $\alpha_1 = 28°$.

Figure 4.24: Visual comparison between $\alpha_1 = 80°$ (base model) and $\alpha_1 = 28°$.

4.2.1.1 α_1 variation

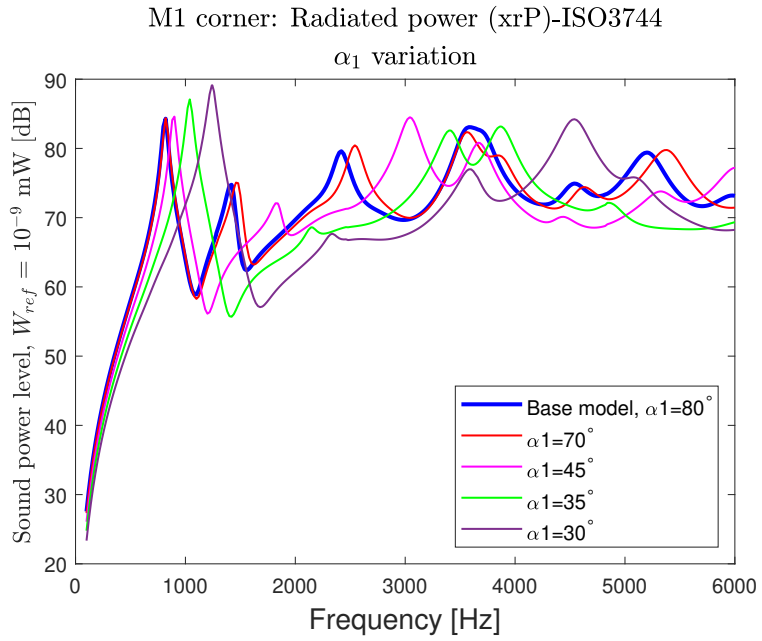

Figure 4.25: Radiated power for M1 single corner with X240 mm, Y=120 mm, and $\alpha_2 = 80°$ with varying α_1.

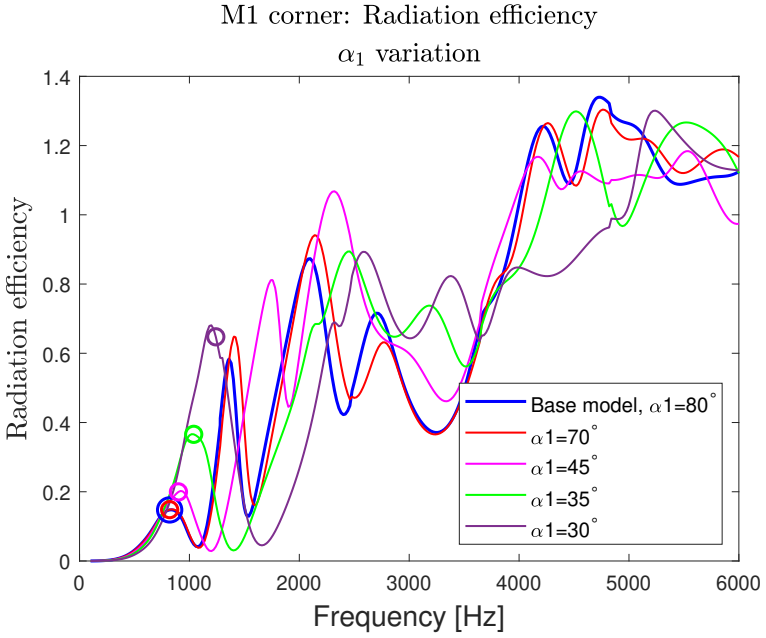

Figure 4.26: Radiation efficiency for M1 single corner with X240 mm, Y=120 mm, and $\alpha_2 = 80°$ with varying α_1. With the frequency of the corresponding first bending modes marked with circles.

4.2.1.2 α_2 variation

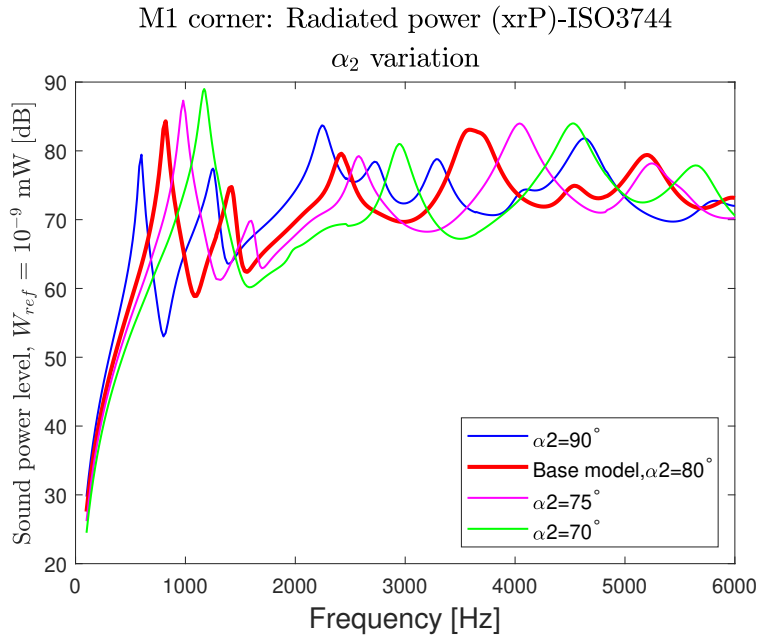

Figure 4.27: Radiated power for M1 single corner with X240 mm, Y=120 mm, and $\alpha_1 = 80°$ with varying α_2.

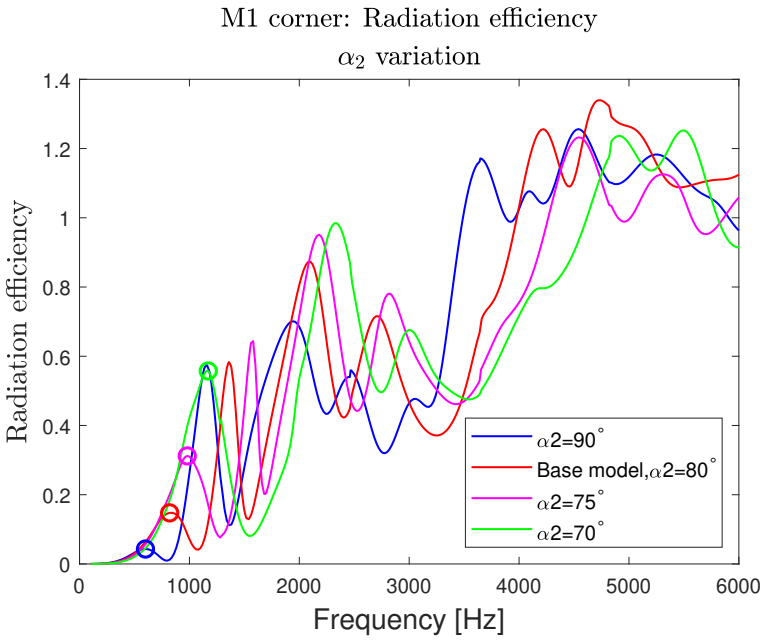

Figure 4.28: Radiation efficiency for M1 single corner with X240 mm, Y=120 mm, and $\alpha_1 = 80°$ with varying α_2. With the frequency of the corresponding first bending modes marked with circles.

From Figure 4.25 and 4.27, it can be observed that the smaller α_1 or α_2 gets, the higher the radiated power peak gets. The peaks also have an increase in frequency

when α_1 or α_2 is decreased. The large size of the rib results in a lot of modes, which makes it difficult to find a pattern in the radiation efficiency. However, for both the α_1 and α_2 variations, the first peaks in the radiation efficiency match the corresponding first bending modes of the ribs. This is not ideal since this will cause the radiated power to increase more compared to if the frequency does not match.

In hindsight, the base model of model 1 corner should have been smaller, similar to model 1. It is hard to see any trends in radiation efficiency with such large ribs. Also, the radiated power does not follow the trend observed for other ribs, which is that when the area increases, the power increases as well. Since a decrease in the angle α_1 or α_2 decreases the area of the rib while there is an increase of the radiated power. Therefore, simulations with different areas, not only X=240 mm and Y=120 mm, should have been performed and investigated.

4.2.2 R variation

For these simulations, the radius of the corner (R) was varied while the other dimensions of the rib: X=240 mm, Y=120 mm, and $\alpha_1 = \alpha_2 = 80°$ were fixed.

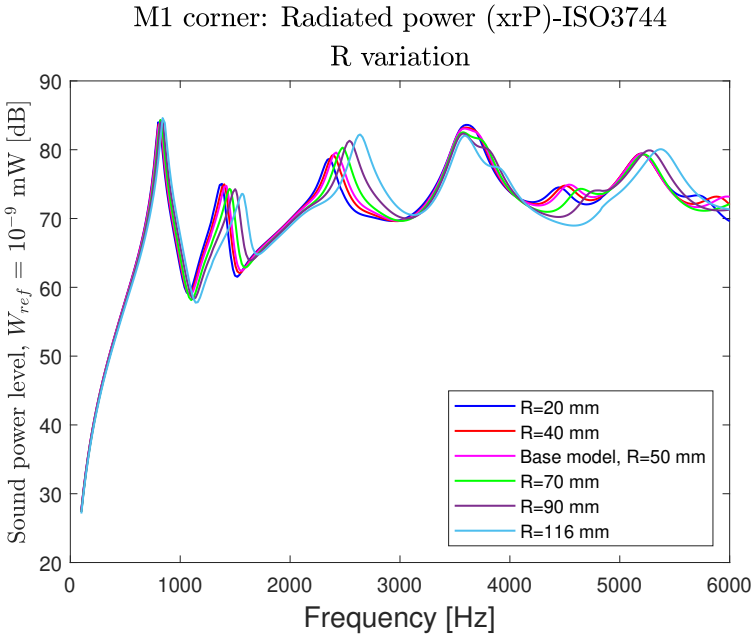

Figure 4.29: Radiated power for M1 single corner with X240 mm, Y=120 mm, and $\alpha_1 = \alpha_2 = 80°$ with varying R.

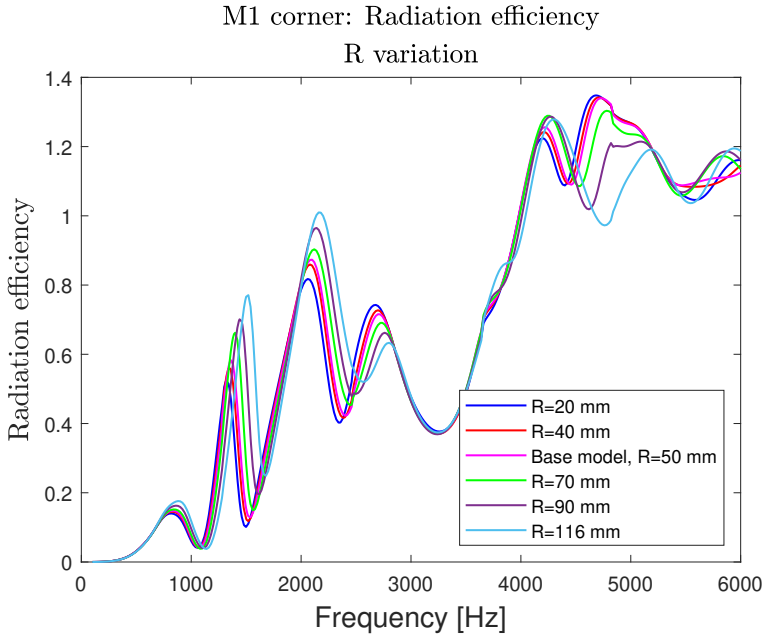

Figure 4.30: Radiation efficiency for M1 single corner with X240 mm, Y=120 mm, and $\alpha_1 = \alpha_2 = 80°$ with varying R.

Notable from these simulations is that it is clear that the radius (R) on the corner does not affect the acoustic behavior of the rib significantly. This is most likely caused by the fact that when the radius, R, changes, the geometry of the rib does not change significantly. The base model, with R=50 mm, has an area of 48365 mm^2 while the model with the largest radius has an area of 46352 mm^2, which is a decrease of 4.2 %. For the other ribs, a smaller radius reduces the area of the rib, which is not the case for this model, this will be discussed in Chapter 5. Furthermore, the argument that the radius variation does not change the rib geometry significantly is also supported by the fact that the frequencies of the first bending modes do not change significantly either, see A.3.3.3.

4.3 Model 2-Single rib (M2 single)

4.3.1 Area variation

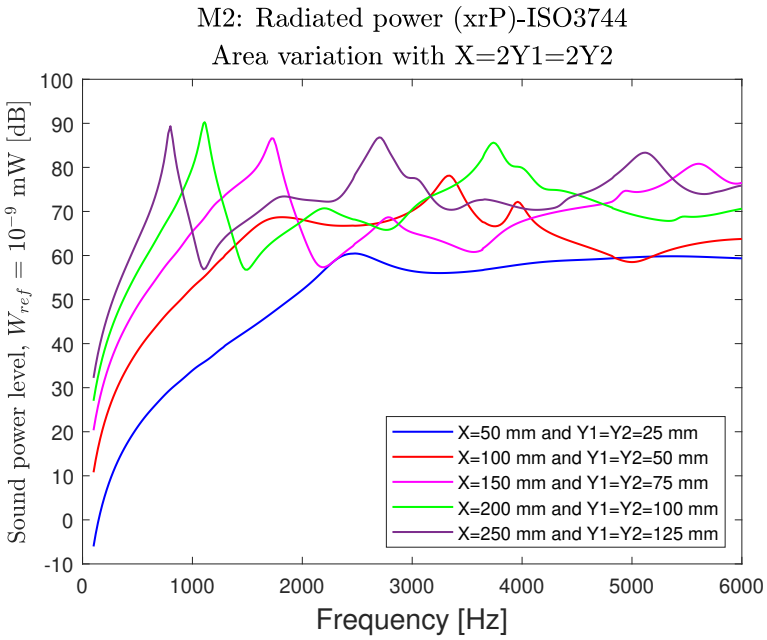

Figure 4.31: Radiated power for M2 single for area variation with X=2Y1=2Y2.

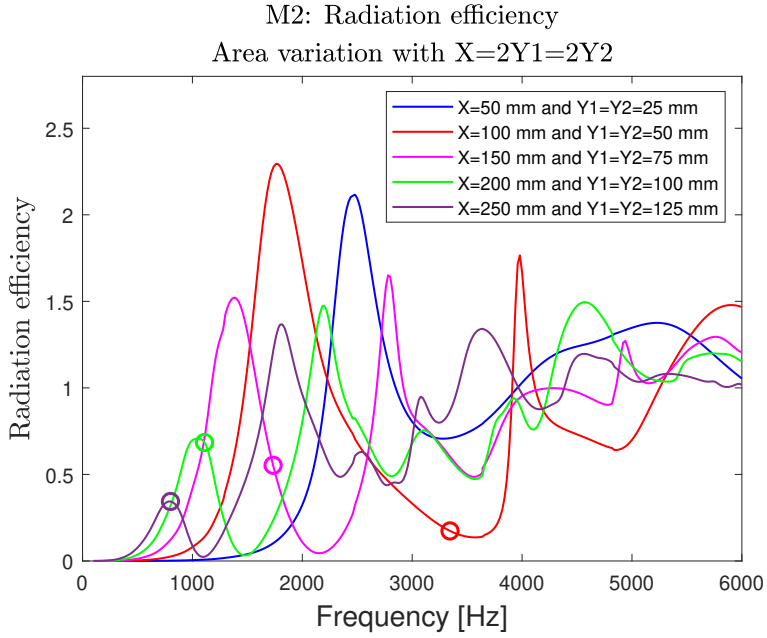

Figure 4.32: Radiation efficiency for M2 single for area variation with X=2Y1=2Y2. With the frequency of the corresponding first bending modes marked with circles.

As the results from Model 1 single rib area variation, larger ribs radiate more than smaller ribs. One thing to note, similar to model 1 single rib, is that X=200 mm, Y1=Y2=100 mm has a slightly higher radiated power than the larger rib, X=250 mm, Y1=Y2=125 mm. This is because there is a better match between the first bending mode and the peak in radiation efficiency, see Figure 4.32. This also explains why the smallest rib (X=50 mm and Y1=Y2=25 mm) has such a low radiated power since the frequency of the first bending (13490 Hz) mode is outside of the frequency range.

4.3.2 Constant area

To investigate the acoustic performance of ribs with the same area but different dimensions, three areas were tested: 7200 mm^2 (same as the base model), 3600 mm^2, and 12800 mm^2.

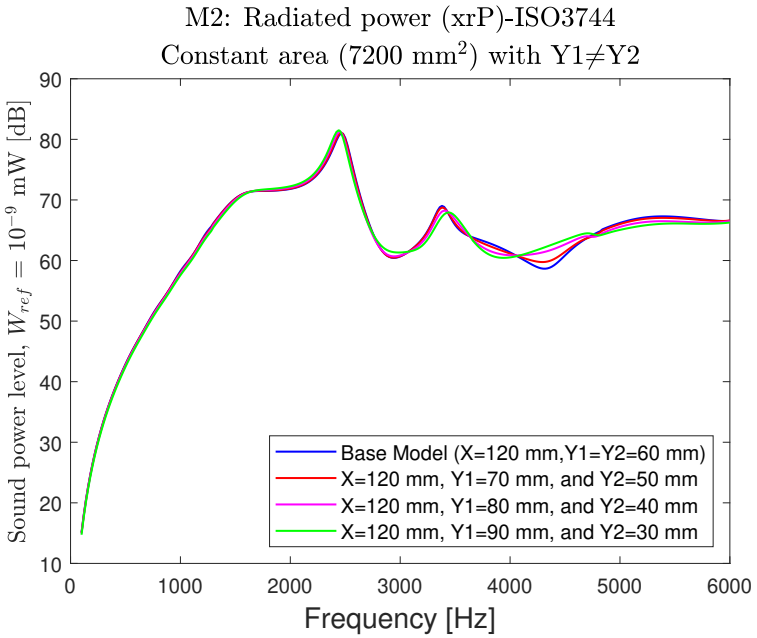

Figure 4.33: Radiated power for M2 single with constant area, 7200 mm^2, with Y1≠Y2.

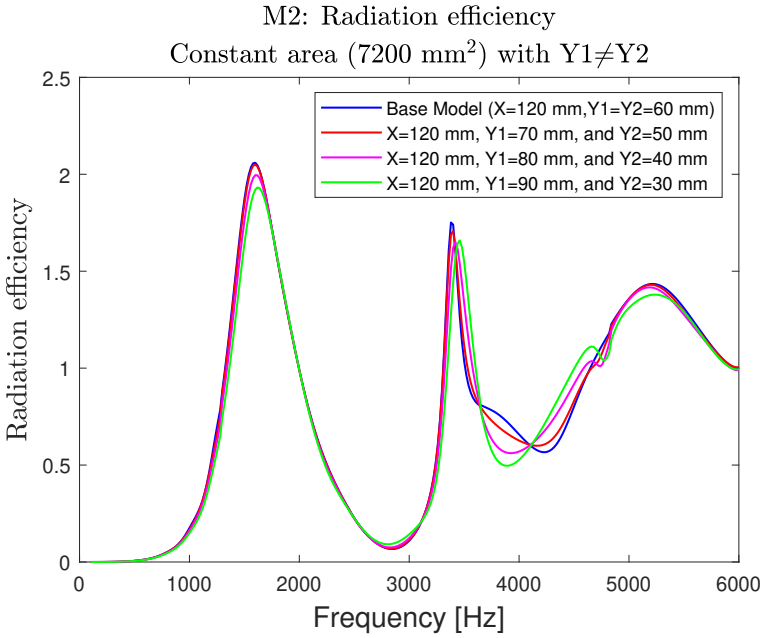

Figure 4.34: Radiation efficiency for M2 single with constant area, 7200 mm^2, with Y1≠Y2.

From Figure 4.33 and 4.34, it can be observed that the different ribs that have the same area behave similarly and there are no ribs that deviate from the base model. Both the radiated power and radiation efficiency have very similar values for the whole frequency range. This behavior can also be seen for 12800 mm^2, see A.4.4.2.

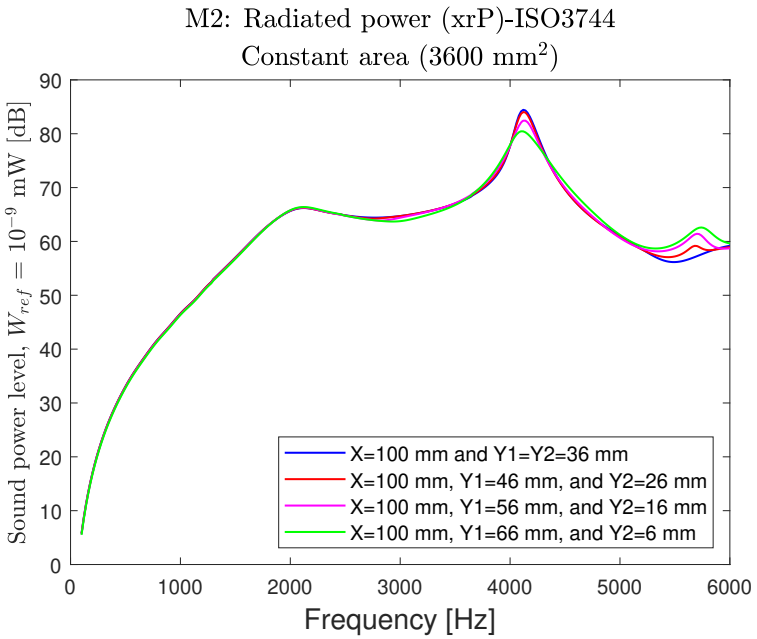

Figure 4.35: Radiated power for M2 single with constant area, 3600 mm^2, with Y1≠Y2.

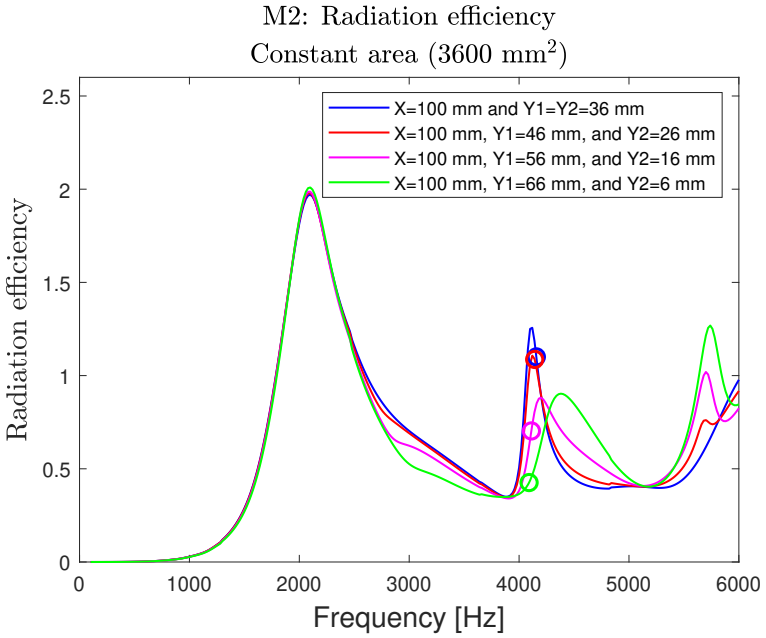

Figure 4.36: Radiation efficiency for M2 single with constant area, 3600 mm^2, with Y1≠Y2. With the frequency of the corresponding first bending modes marked with circles.

It can be seen in Figure 4.35, that the peaks of the rib with dimensions of X=100 mm and Y1=Y2=36 mm deviate with around 4 dB from the rib with dimensions of X=100 mm and Y1=Y2=6 mm. This is explained by the fact that the radiation efficiency is lower for the corresponding frequency of the first bending mode. This is the case for each of the ribs except the rib X=100 mm and Y1=Y2=36 mm, see Figure 4.36. Furthermore, the mean square velocities also differs for the different ribs, which can be seen in Figure A.57.

4.3.3 R variation

To investigate how a curvature on the outer edge affects the acoustic performance, seven different curvatures were tested on the base model, X=120 mm and Y1=Y2=60 mm.

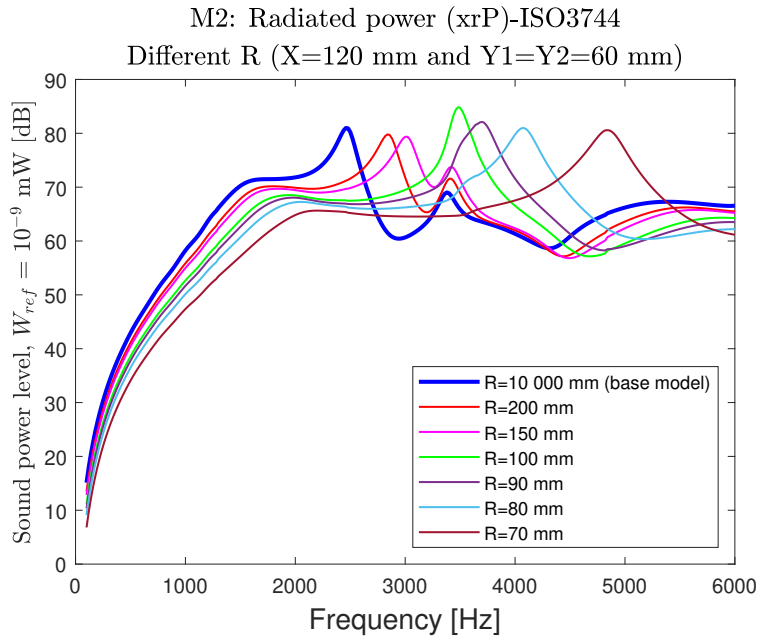

Figure 4.37: Radiated power for M2 single with variation of curvature on the outer edge.

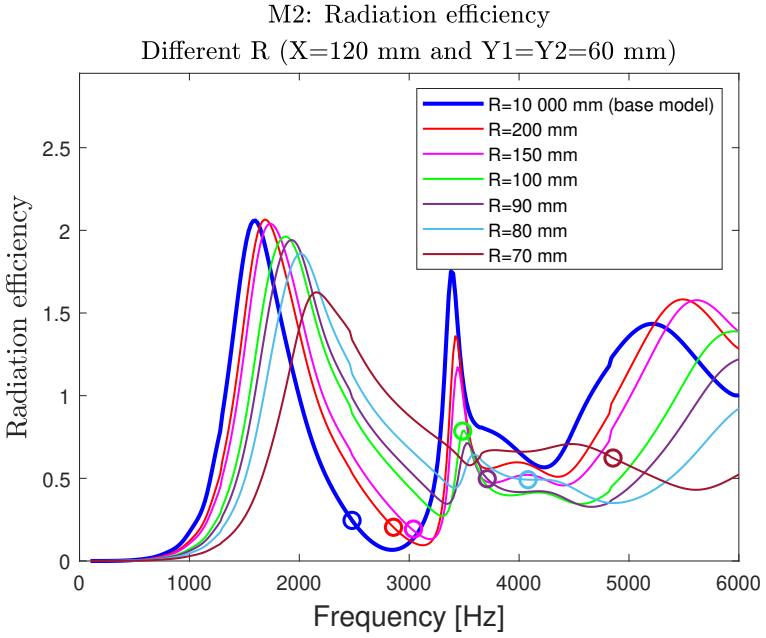

Figure 4.38: Radiation efficiency for M2 single with variation of curvature on the outer edge. With the frequency of the corresponding first bending modes marked with circles.

From Figure 4.37 it can be observed, similar to M1 single, see Figure 4.13, that a small curvature can decrease the radiated power by about 1.5 dB. However, like model 1 single rib, a larger curvature (small R) increases the radiated power which is due to a better match between the first bending mode and the radiation efficiency, see Figure 4.38. It is also notable that the frequency of the peaks for both the radiated power and the radiation efficiency increases for smaller radii.

4.4 Model 1- Double rib (M1 double)

Every model has a distance of 40 mm and an angle of 0.01 degrees between the ribs unless explicitly stated.

4.4.1 Area variation

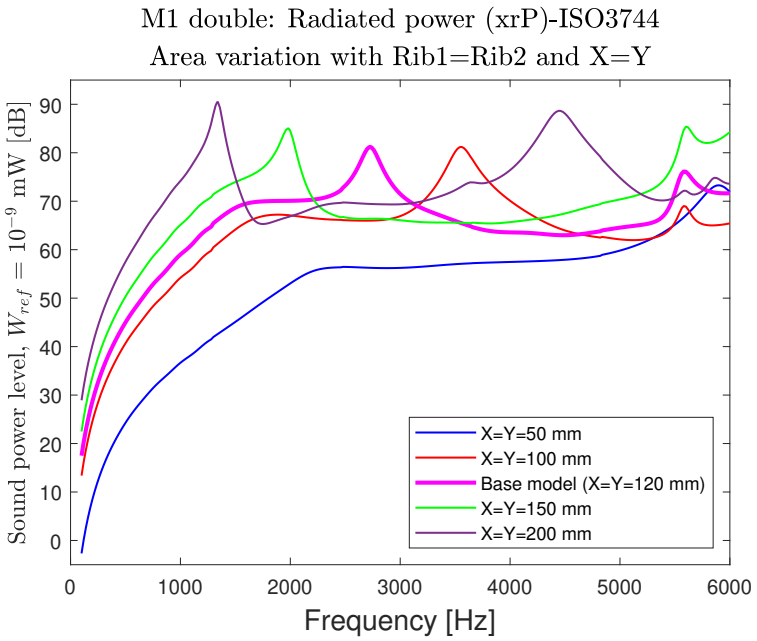

Figure 4.39: Radiated power for M1 double for area variation with Rib1=Rib2 and X=Y.

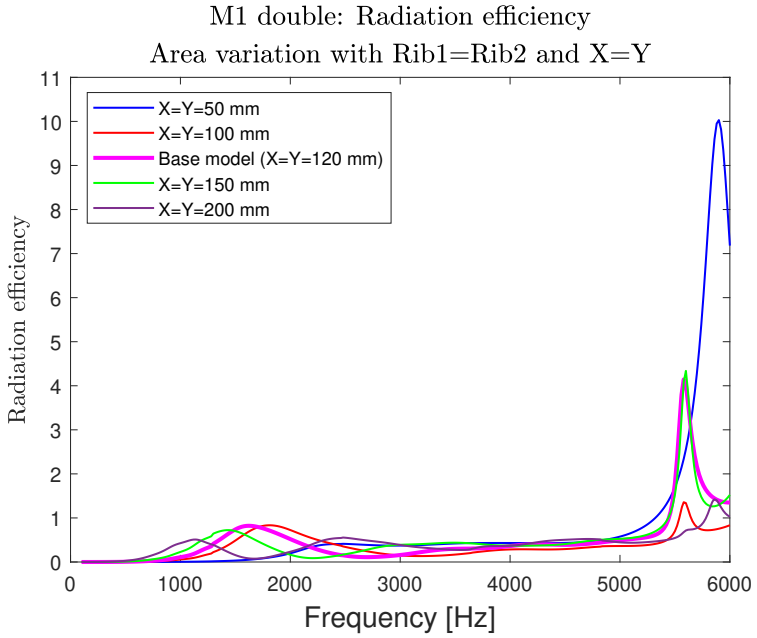

Figure 4.40: Radiation efficiency for M1 double for area variation with Rib1=Rib2 and X=Y.

When the area changes, the same trend as for M1 single and M2 single can be observed, a larger area results in an increased radiated power, see Figure 4.39. Notable from the radiation efficiency, see Figure 4.40, is that the ribs, X=Y=50 mm, increase significantly at about 5800 Hz, this causes the radiated power to increase to a level which is comparable to the other ribs. However, since this is at such a high frequency, it can still be concluded that the smallest ribs perform best from an acoustic point of view. Since the results from the M1 single and M1 double are so similar, the radiated power for ribs with dimensions X=Y=120 mm and X=Y=200 mm were plotted together, see Figure 4.41 below:

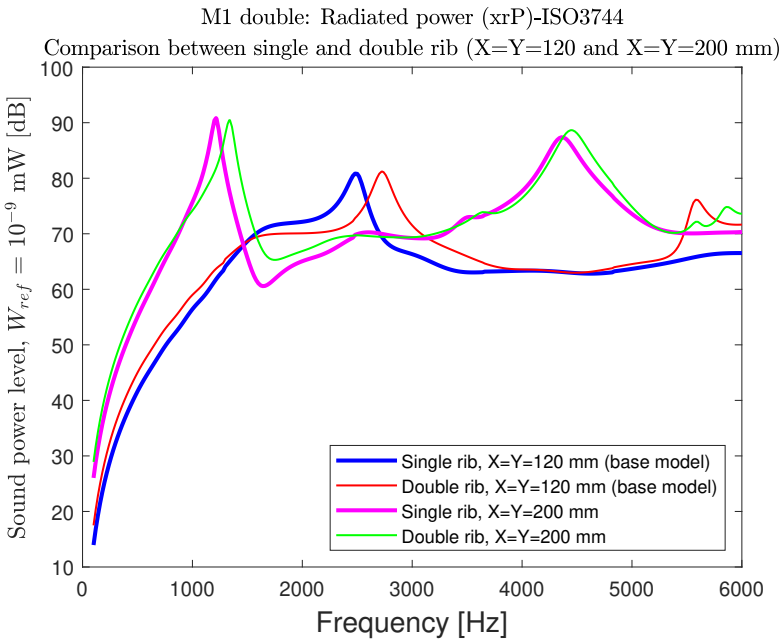

Figure 4.41: Comparison between the radiated power for M1 single and M1 double for ribs with dimensions X=Y=120 mm and X=Y=200 mm.

From Figure 4.41, it been observed that the radiated power does not deviate significantly between the single and double ribs. However, there is an increase in the frequency of the peaks, this is likely caused by the increased stiffness of the structure by adding a second rib. It is important to note that the distance between the ribs for the double variants is 40 mm. How the results change by simulating with different distances is shown in Figure 4.57.

4.4.2 Area variation with Rib1≠Rib2

4.4.2.1 Rib1: X=Y=120 mm

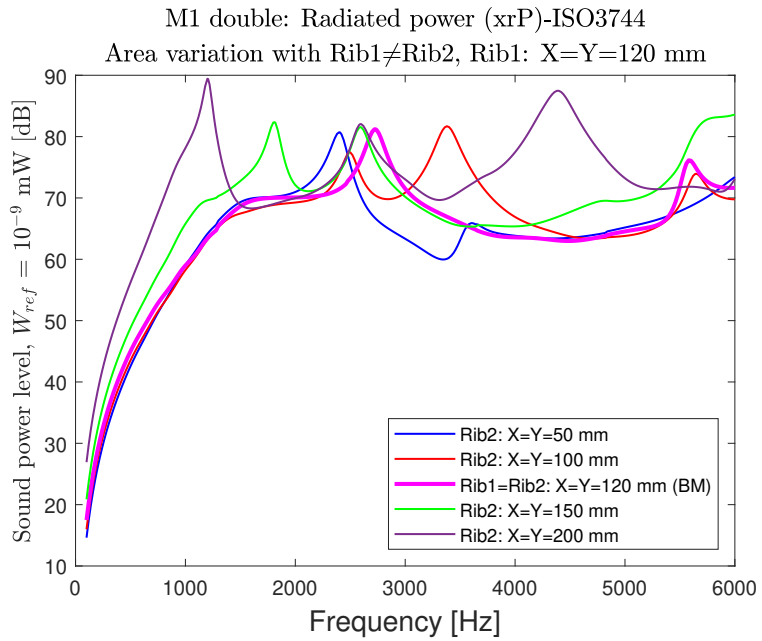

Figure 4.42: Radiated power for M1 double for area variation with Rib1≠Rib2 and Rib1: X=Y=120 mm.

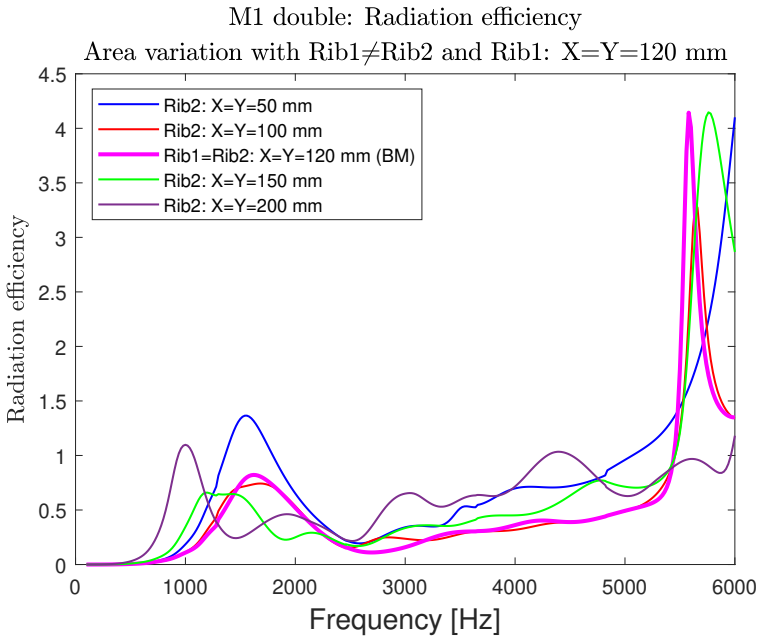

Figure 4.43: Radiation efficiency for M1 double for area variation with Rib1≠Rib2 and Rib1: X=Y=120 mm.

4.4.2.2 Rib1: X=Y=50 mm

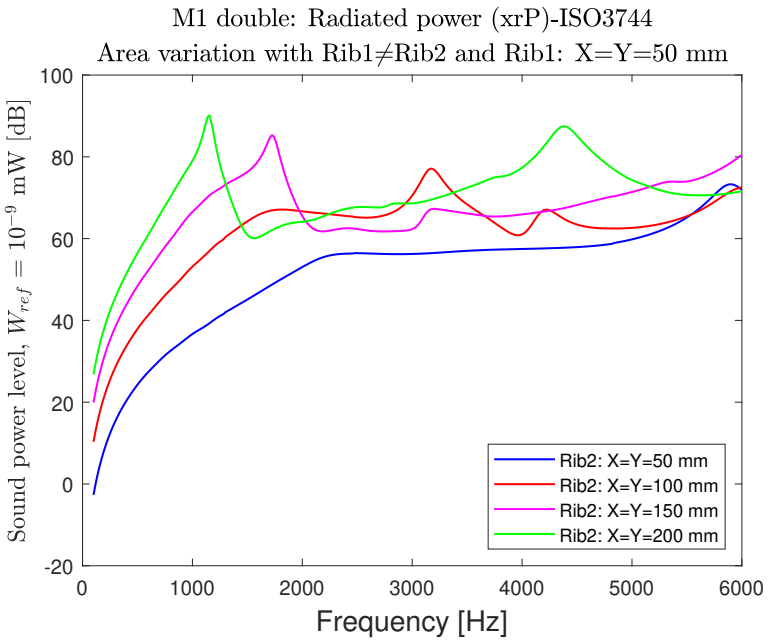

Figure 4.44: Radiated power for M1 double for area variation with Rib1≠Rib2 and Rib1: X=Y=50 mm.

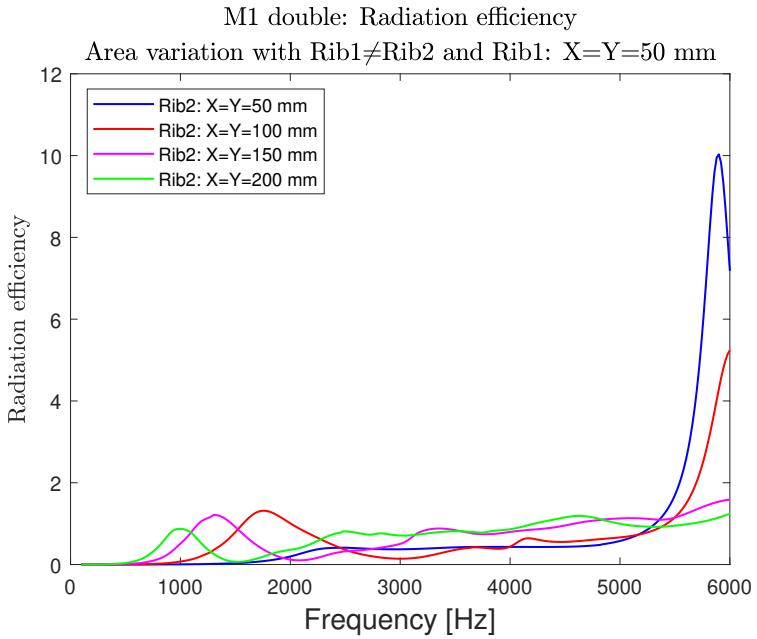

Figure 4.45: Radiation efficiency for M1 double for area variation with Rib1≠Rib2 and Rib1: X=Y=50 mm.

4.4.2.3 Rib1: X=Y=200 mm

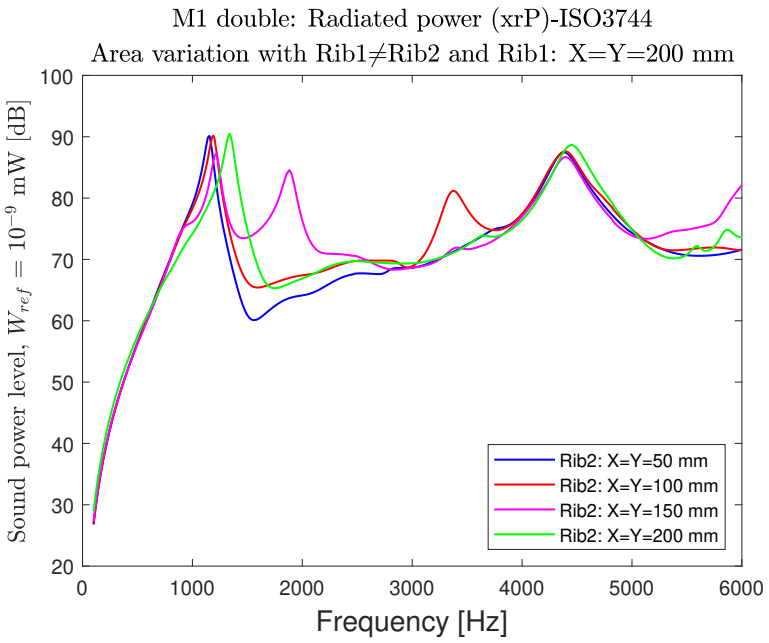

Figure 4.46: Radiated power for M1 double for area variation with Rib1≠Rib2 and Rib1: X=Y=200 mm.

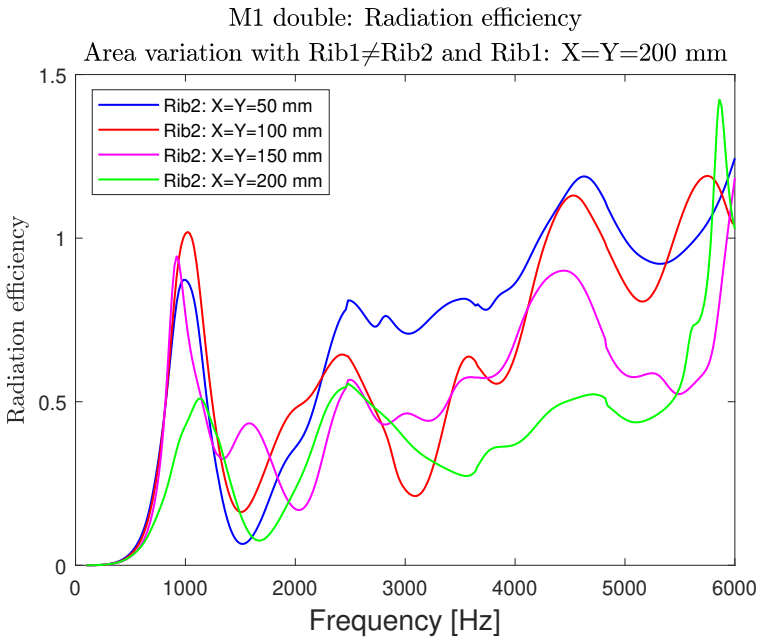

Figure 4.47: Radiation efficiency for M1 double for area variation with Rib1≠Rib2 and Rib1: X=Y=200 mm.

From Figure 4.42 - 4.47 it can be noted that there is often an extra peak in the radiated power. This happens for the ribs that do not have the same dimensions,

resulting in two different first bending modes for the ribs. However, as for the area variation, it can be observed that for the cases with at least one large rib, the radiated power increases significantly compared to the smaller ribs, for example, X=Y=50 mm.

4.4.3 R variation

4.4.3.1 Rib1=Rib2

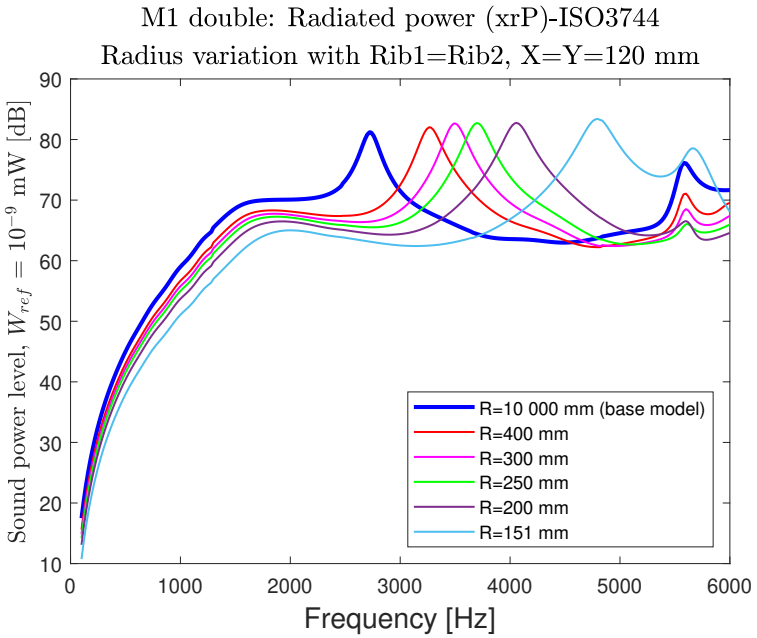

Figure 4.48: Radiated power of M1 double for variation of the curvature R, where Rib1=Rib2.

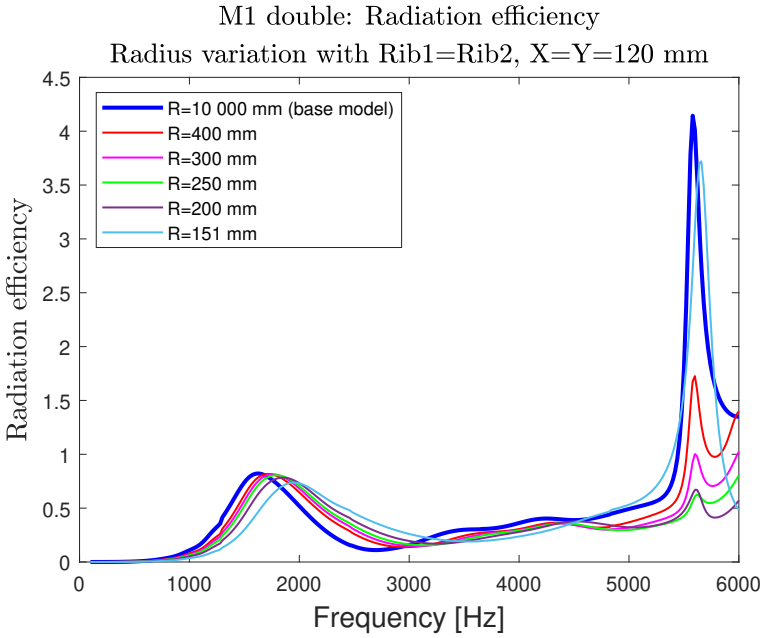

Figure 4.49: Radiation efficiency of M1 double for variation of the curvature R, where Rib1=Rib2.

4.4.3.2 Rib1≠Rib2, Rib1: R=151 mm

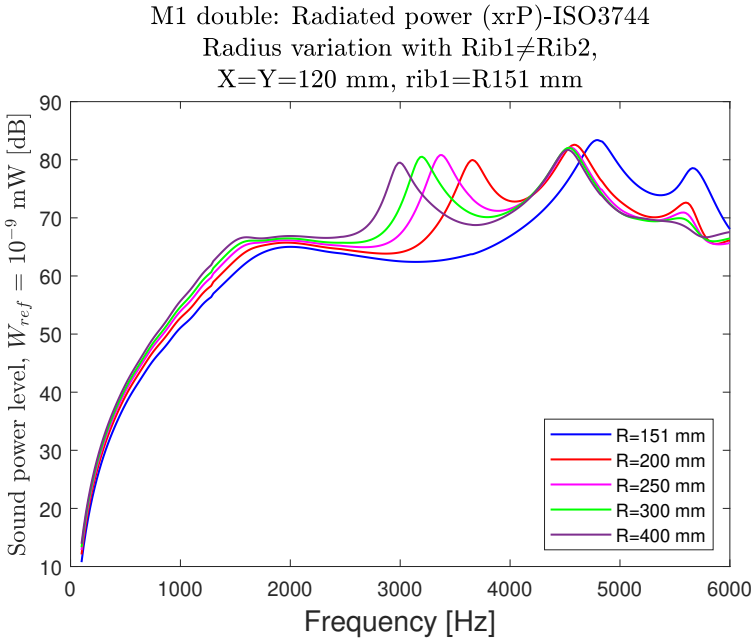

Figure 4.50: Radiated power of M1 double for variation of the curvature R, where Rib1≠Rib2 and R for Rib1=151 mm.

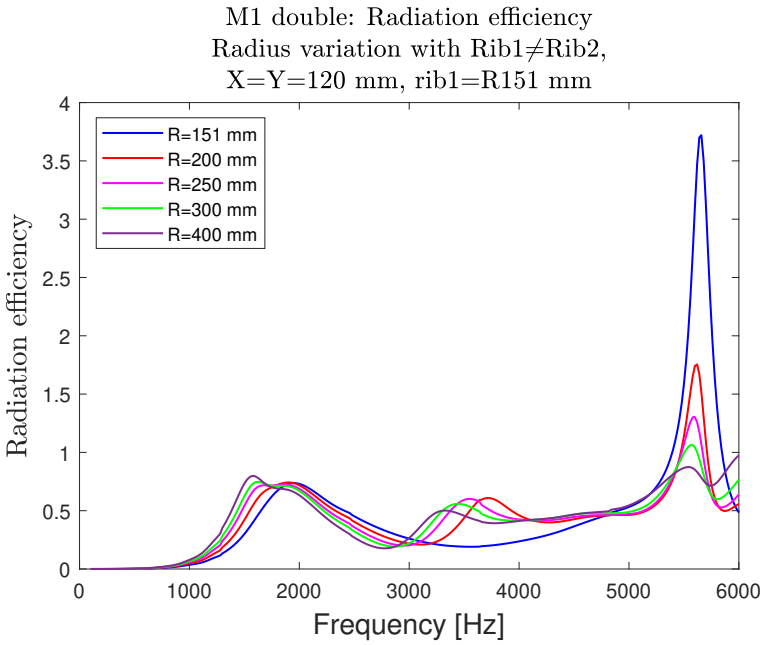

Figure 4.51: Radiation efficiency of M1 double for variation of the curvature R, where Rib1≠Rib2 and R for Rib1=151 mm.

4.4.3.3 Rib1≠Rib2, Rib1: R=10 000 mm

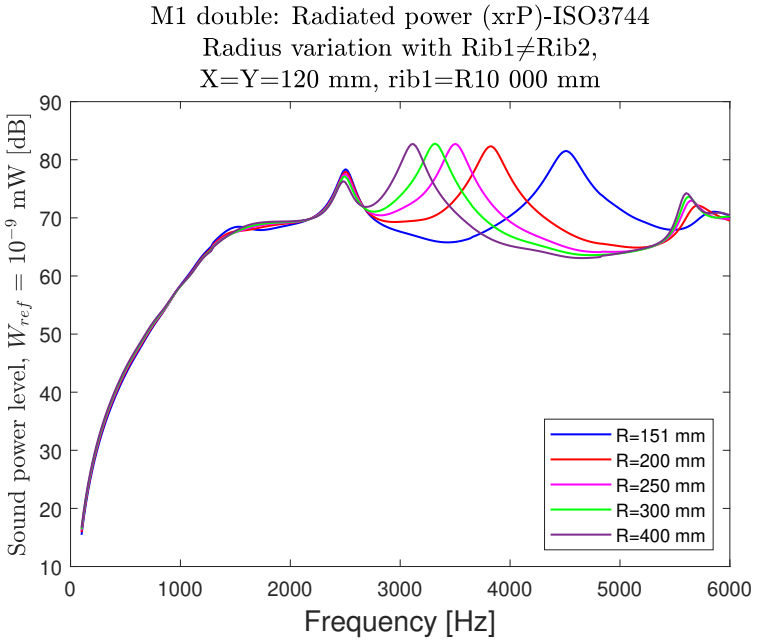

Figure 4.52: Radiated power of M1 double for variation of the curvature R, where Rib1≠Rib2 and R for Rib1=10 000 mm.

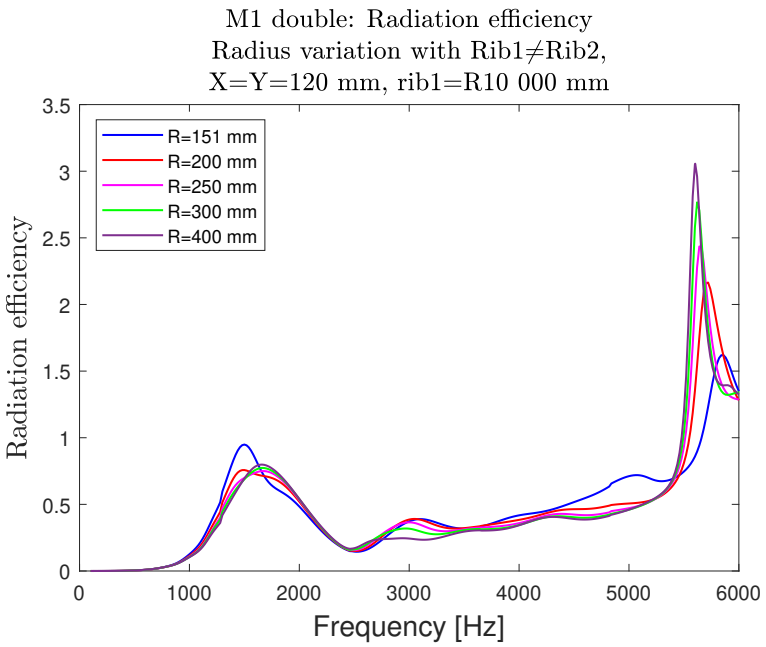

Figure 4.53: Radiation efficiency of M1 double for variation of the curvature R, where Rib1≠Rib2 and R for Rib1=10 000 mm.

From Figure 4.48, it can not be said that adding a small curvature to the ribs decreases the radiated sound as for M1 single, see Figure 4.13, and M2 single, see Figure 4.37. However, in Figures 4.50 and 4.52, it can be observed that the lowest peak radiated power is achieved using a small curvature like for M1 single and M2 single.

4.4.4 Variation of the distance between the ribs

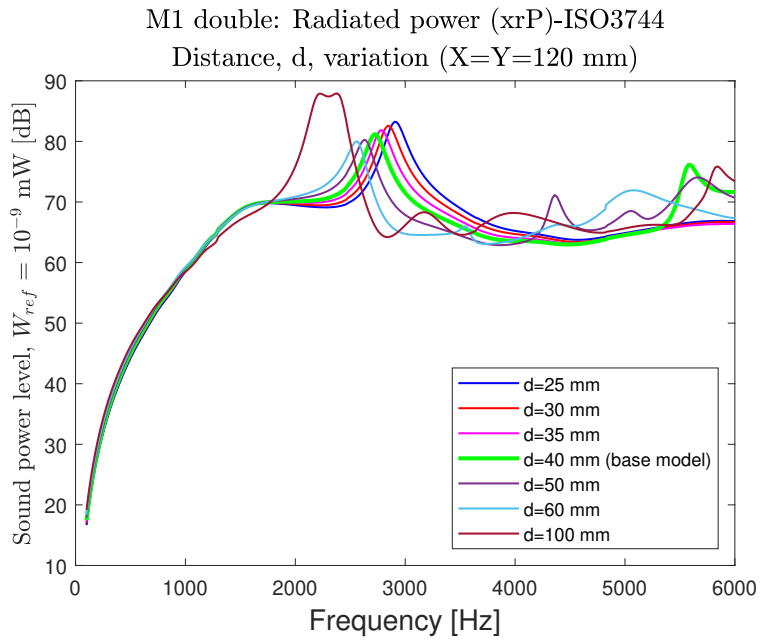

Figure 4.54: Radiated power for M1 double for the distance between the ribs variation.

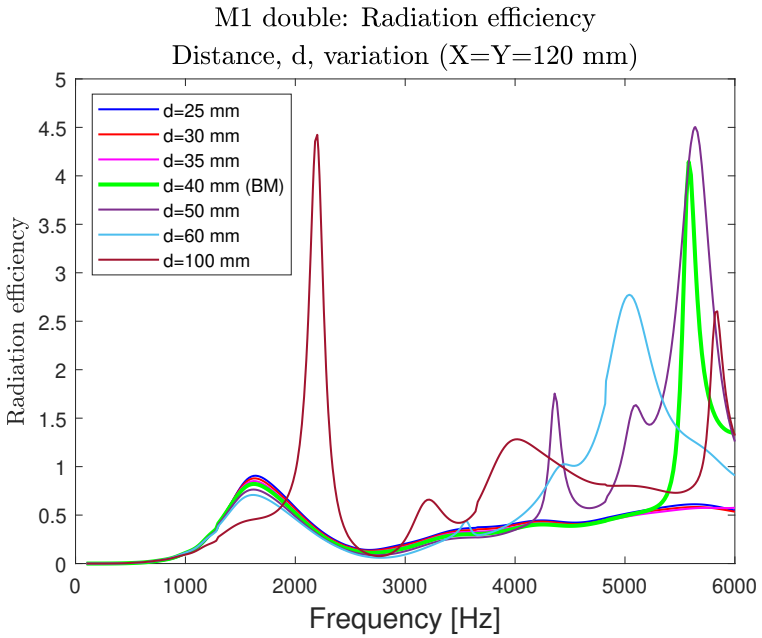

Figure 4.55: Radiation efficiency for M1 double for the distance between the ribs variation.

It can be observed in Figure 4.54, that for a distance of 100 mm between the ribs the radiated power increases significantly. This is the same case for the radiation

efficiency, see Figure 4.55, where 100 mm has a significantly higher efficiency than the other ribs. There is not a match with the radiation efficiency and the first bending modes but the radiated power still increases substantially compared to the other ribs. This could potentially be explained by the fact that acoustic resonance occurs at this distance. To find at what distance between the ribs this occurs, a few extra distances were investigated, see Figure 4.56 below:

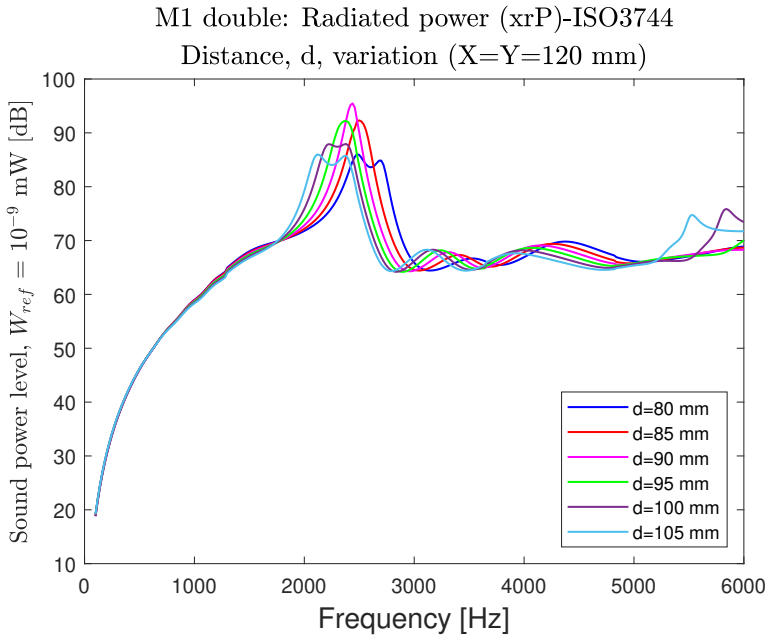

Figure 4.56: Radiated power for M1 double for the distance between the ribs variation.

It can be concluded from Figure 4.56 that 90 mm results in an increased radiated power compared to 100 mm. Note that these results are based on ribs with dimensions X=Y=120 mm, the base model. To further test how the distance between the ribs affects the results, two other dimensions, X=Y=150 mm and X=Y=200 mm, were also tested. These results were not as clear for the distances tested as the base mode, but a trend can still be observed, see Figures A.76 and A.77. Finally, when comparing a single rib to a double, as was done in Figure 4.41, there was no significant difference between the single and double ribs. With the results from Figures 4.56 and A.77, a second comparison was done, see Figure 4.57 below:

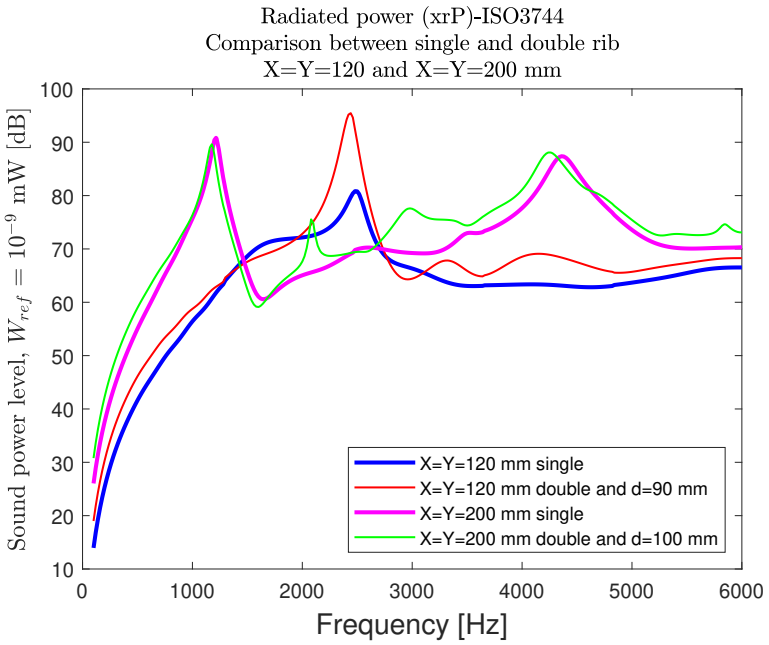

Figure 4.57: Comparison between the radiated power for M1 single and M1 double for ribs with dimensions X=Y=120 mm and X=Y=200 mm.

From Figure 4.57, it can be observed that when choosing the distance between the ribs, some distance increases the radiated power. This is especially notable for the ribs X=Y=120 mm, where there is a difference in power of about 15 dB. For the ribs X=Y=200 mm, the difference is not as large, especially not in the peak corresponding to the first bending mode. However, the power is higher for the double rib between around 1500 Hz and 4000 Hz.

4.4.5 Variation of the angle between the ribs

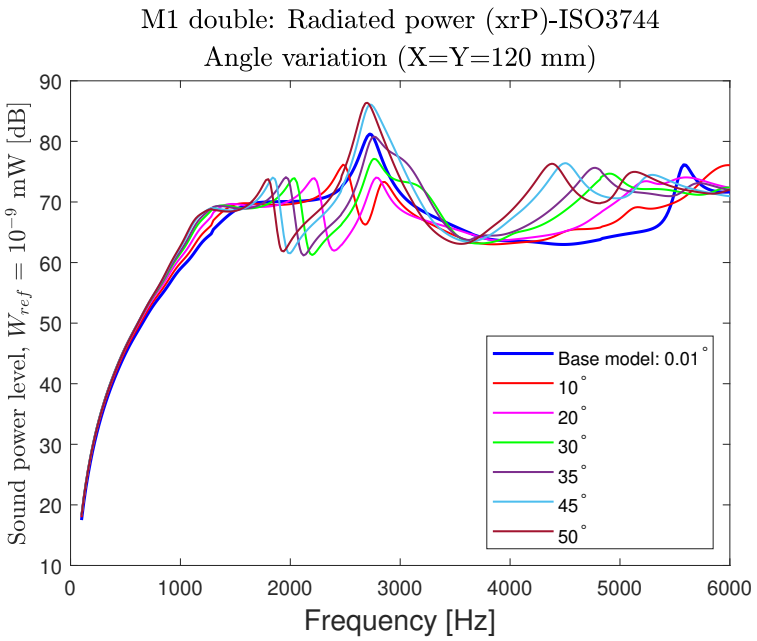

Figure 4.58: Radiated power for M1 double for the angle between the ribs variation.

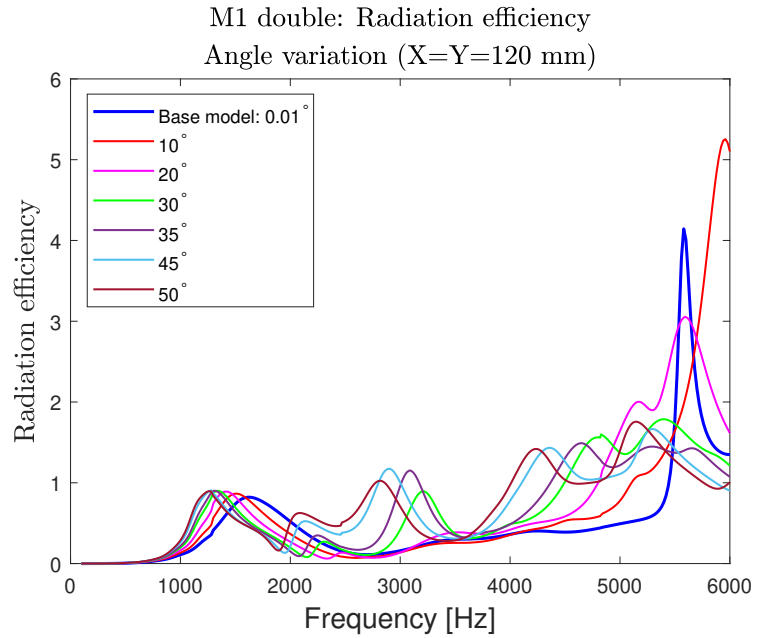

Figure 4.59: Radiation efficiency for M1 double for the angle between the ribs variation.

From Figure 4.58, it can be observed that the radiated power decreases for some angles compared to the base model, the same case as for the distance.

4.4.6 Constant volume between the ribs

For these simulations, the volume between the ribs is kept constant by changing the area (X and Y) of the ribs and the distance (d). Both ribs are always the same size. The idea behind these tests was to investigate how the radiated power behaves if the volume between the ribs is kept constant, similar to a constant area.

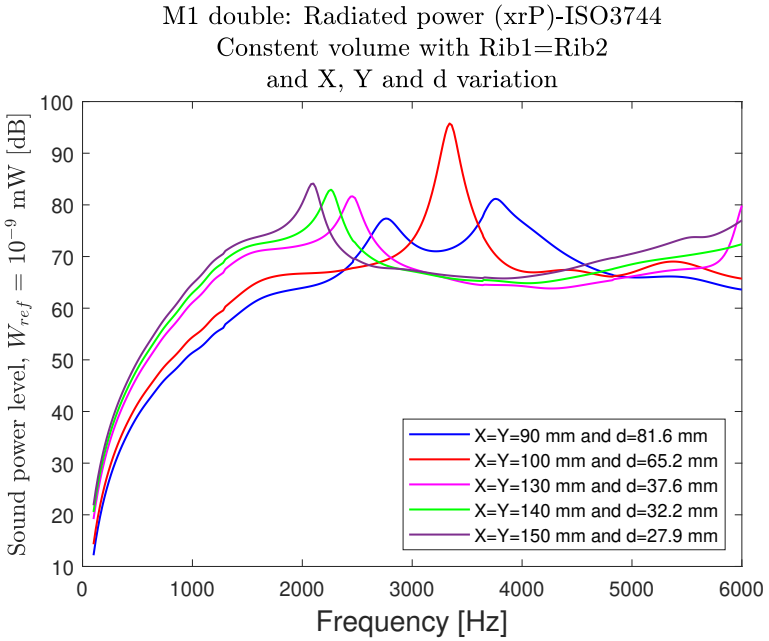

Figure 4.60: Radiated power of M1 double with constant volume between the ribs.

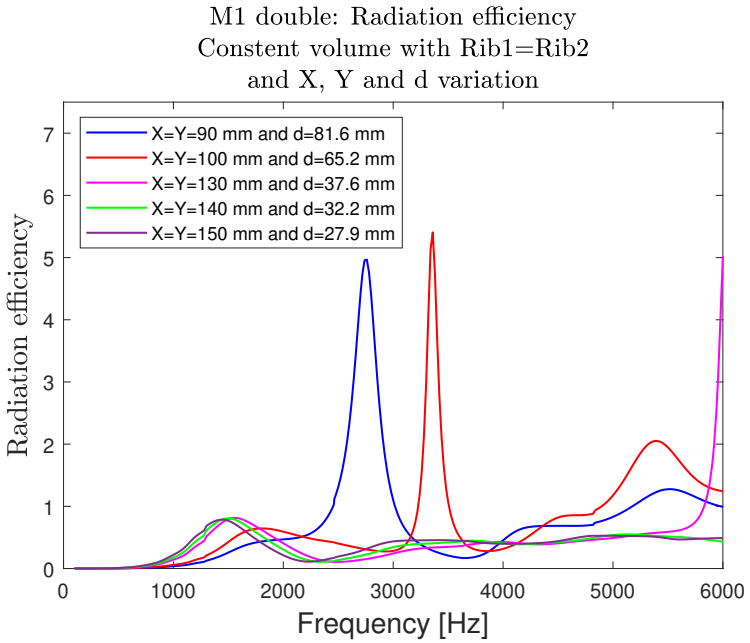

Figure 4.61: Radiation efficiency of M1 double with constant volume between the ribs.

The result from keeping the air volume between the ribs constant, see Figure 4.60, is similar to the results from both the distance and angle variations, see Figures 4.54 and 4.58. The distance differs from the previous results, which indicates that the distance that causes the power to increase significantly is dependent on the dimensions of the rib.

5
Discussion

This chapter will discuss the results from the simulations more generally compared to the previous chapter and the methodology. Finally, the research questions will be answered, along with recommendations for future research.

5.1 Discussion of the results

Different geometries have been shown to affect the frequency of the first bending mode. For the simulations performed in this thesis, all of the frequencies have the same level of excitation, this is not the case for a real EDU. The knowledge of how to shift the frequency of the first bending mode could be used to replace the first bending mode at a frequency with a lower excitation level. With such a shift, it would be possible to lower the radiated sound since the impact of the first bending mode would be decreased.

As mentioned earlier in the report, the radiated power is highly dependent on the mean square velocity and radiation efficiency, as shown in Equation 2.16. The radiation efficiency is difficult to predict before performing simulations, but the velocity does show some patterns. One of these patterns is at which frequency the first peak occurs, as mentioned in the beginning of Chapter 4. The first peak in velocity, often the only peak, always occurs at the first bending mode, which also results in the first peak in the radiated power.

The thickness of the rib has been observed to affect the velocity, where a thicker rib has a higher velocity than a thinner rib, this can be seen in Figures A.22, A.24, A.29, A.33, and A.37. It is important to note that the velocity that is being discussed is the velocity at the first bending mode. This result is due to the velocity boundary condition, if it were instead a distributed force over the boundary, the velocity would most likely be the other way around, i.e., the thicker the rib becomes, the lower the velocity becomes. This will be discussed further in Chapter 5.2.1.

The peak velocity seems to correlate with total length, e.g., X+Y for Model 1 single rib or $X+Y_1+Y_2$ for Model 2 single rib and the area. The velocity seems to decrease if the ratio between the area and the total length decreases. Two good figures to showcase this are Figure A.16 where the area decreases while the length is constant and Figure A.20 where the area is constant and the length is increased. This reasoning can be used on most plots, but it can be difficult to see the effect

from it due to the draft angle on the rib in most simulations. The draft angle increases the thickness and acts in the y-direction, which, for a longer length in the y-direction, increases the average thickness of the rib. As mentioned earlier, a thicker rib increases the velocity, which can sometimes be counteractive. There are, however, some cases where this relation is not true, see Figure 5.1 below.

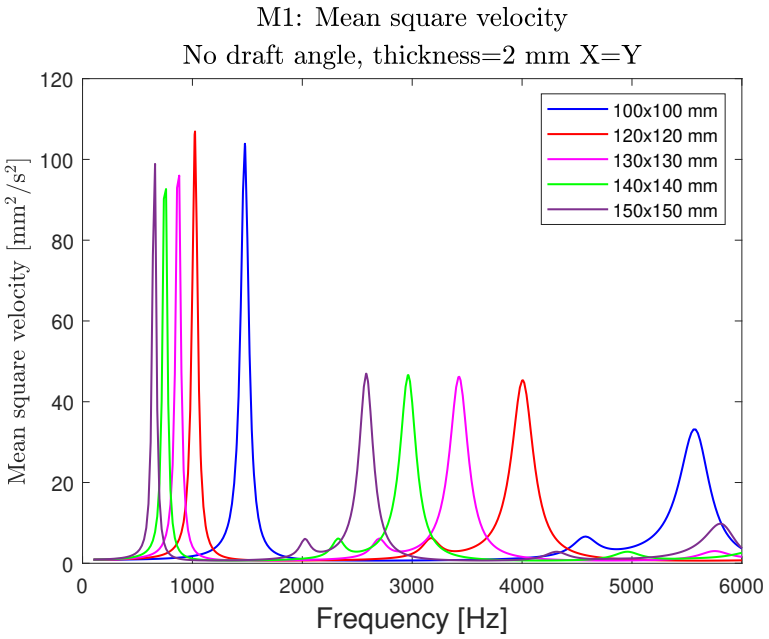

Figure 5.1: Mean square velocity of M1 single rib with different areas and with a constant thickness of 2mm with no draft angle.

It can also be noted that there are two velocity peaks in Figure 5.1 compared to most other cases where there is only one peak. There seems to be a trend that when the rib gets large compared to the thickness, i.e., flexible or less stiff, the results get more difficult to predict. A lower stiffness results in more bending modes within the frequency range, which is why there are two peaks in Figure 5.1. This is also the reason why all results for model 1 corner- single rib, in sub-chapter 4.2, are difficult to draw any conclusions from.

Even though it is difficult to predict the outcome of the radiation efficiency, some minor patterns can be observed. The previously mentioned ratio, the area divided by total length, seems to affect the frequency at which the peak occurs. If a rib's ratio increases by decreasing the area or increasing the difference between X and Y, see Figure 4.4 and 4.6, the frequency of the peak increases. There is, however, the case of constant area with different R, see Figure 4.16, where the ratio decreases but the frequency still increases. A decrease in the area of the rib seems to increase the peak value, this can be observed in e.g., Figure 4.4 and 4.12. However, there are some cases where this does not seem to be true. The ribs with the smallest area have an decrease in peak value in most cases, this can be seen in Figure 4.4, 4.12 and 4.32. There is also the case for model 2 single rib when using a smaller R, hence smaller area, results in a lower peak value for the radiation efficiency, see Figure

4.38. Important to note is that there is still no clear pattern on how the radiation efficiency relates to the bending modes.

5.2 Methodology

In this sub-chapter, the methodology will be discussed, along with the strengths and weaknesses of the thesis work. This includes the prototype models, choice of boundary conditions, and simulations.

5.2.1 Prototype models and boundary conditions

The four prototype models with parametrization were chosen to represent as many types of ribs as possible. However, the geometry of an actual rib on an EDU housing is highly dependent on the surrounding structure and can, therefore, have many different shapes that are not fully recreated in the prototype models. An example of this is the back of the rib structure, which is curved on an EDU since the housing is cylindrical, which was straight for all of the models. Including this curvature into the back would most likely affect the results, but since a singular rib is small compared to the EDU, adding this curvature would not change the structure significantly. For this reason, the curvature of the housing was not included in the rib models. Another aspect is that the results from the simulations are based on the radiated power of the rib and not the whole structure, which makes the comparisons between the rib variations valid since the back is kept the same for all the variations. In summary, as long as the back of the rib structure is kept the same for each geometric variation, comparisons can be made to compare the different designs. There are also shapes of the rib that have not been taken into account, mainly due to the limited time. However, this does not make the current results incorrect but rather something that should be looked at in future research, which is discussed in Chapter 5.4.

Some simplifications were made to the models to minimize the number of models that were needed. One of these simplifications was to put R=10 000 mm instead of completely straight. As shown in Figure 3.10, the results are almost identical, which makes it a good approximation. There is, however, no such verification for using a small (0.01°) angle between the ribs for model 1 double rib. The impact of the small angle is, therefore, unknown but most likely very small. Even if there is a small impact on the results, it is still consistent throughout all simulations and will have the same impact on all results since it is the relative differences of the results that are being compared, therefore it should not affect the results.

The choice of boundary condition, an infinitely stiff boundary, is not an exact representative of reality since physical objects always have a finite stiffness. The rib structures that were studied represent a cut-out of an EDU housing and removing it from the complete structure. The stiffness of the boundary should, therefore, be higher than a standalone rib structure. This can be motivated by the fact that it should compensate for the fact that the back of the rib is no longer part of a larger

structure, the EDU housing. However, it would be more representative to assign a higher but finite stiffness, but what value to use was unclear.

As mentioned in Chapter 5.1, the choice of boundary condition has an impact on the velocity results. The velocity boundary condition increases the velocity at resonance, i.e., peak velocity, for increased thickness of the rib. This is because the weight-to-stiffness ratio is increased, which increases the displacement and, therefore, the velocity. An analogy could be a spring with a weight at the bottom of the spring, if that weight is increased the displacement and the speed would increase. The velocity does not represent reality completely since, in reality, the velocity is frequency-dependent and can act in different directions. However, to be able to compare the characteristics between different ribs, the input needs to be the same. As mentioned in Chapter 3.2.2, using a distributed load would affect the results for each rib type differently due to the difference in mass, according to Newton's second law, which would make the velocity dependent on the mass. However, since the weight of the model is small compared to the rest of the EDU, the velocity boundary condition is the better option.

5.2.2 Simulations

The simulations were performed using four different programs: CATIA, ANSA, NASTRAN, and Actran, which could introduce errors since an error in the model in one program will be transferred to the next. However, since both CATIA and ANSA are industry standards when it comes to CAE applications, these two programs are compatible with each other. From ANSA, the model is exported in the NASTRAN format, which means that the output format is in the correct format, which means that NASTRAN will interpret the model from ANSA as expected. Finally, both Actran and NASTRAN were developed by the same company and are capable of reading the NASTRAN format as well. There are likely no errors when the model is imported to Actran either.

Errors could also be introduced when the CAD model is meshed in ANSA since an automatic meshing function is used. However, the settings of this function, which generates the mesh, have been checked to capture the geometry of the structure accurately, and the mesh elements are of a size appropriate for the acoustic simulations, see Figures 3.14 and 3.15. By using the same setting for all the models, each model is meshed in the same way, which makes the comparisons between the models valid, even if there are imperfections in the meshing process.

NASTRAN is used to calculate the nodal displacement of the surface nodes of the model and the eigenmodes, the results were saved as an op2 file and a NASTRAN punch file (pch). The reason for splitting the result into two different files is to separate the displacements and the eigenmodes since it was required for BC mesh in Actran. It could be possible to use BC mesh with both the displacement and the eigenmodes, but after encountering issues due to limited knowledge and time, this was not investigated further. However, the disadvantage of a pch file is that they

are very large ($\sim$ 1 GB) compared to an op2 file, which can cause storage problems since a pch file is not binary as the op2 file.

In Actran, the nodal displacements of the surface nodes calculated in NASTRAN are imported and mapped to the acoustic mesh using the function BC mesh, which places a mesh a small distance from the surface mesh of the model. If the model has a complex geometry or small features, this second mesh may not capture the geometry correctly if the tolerances are not set correctly. However, since the models used in this project do not have such complex shapes, the errors from using BC mesh in this case are low, see Figure 5.2 below.

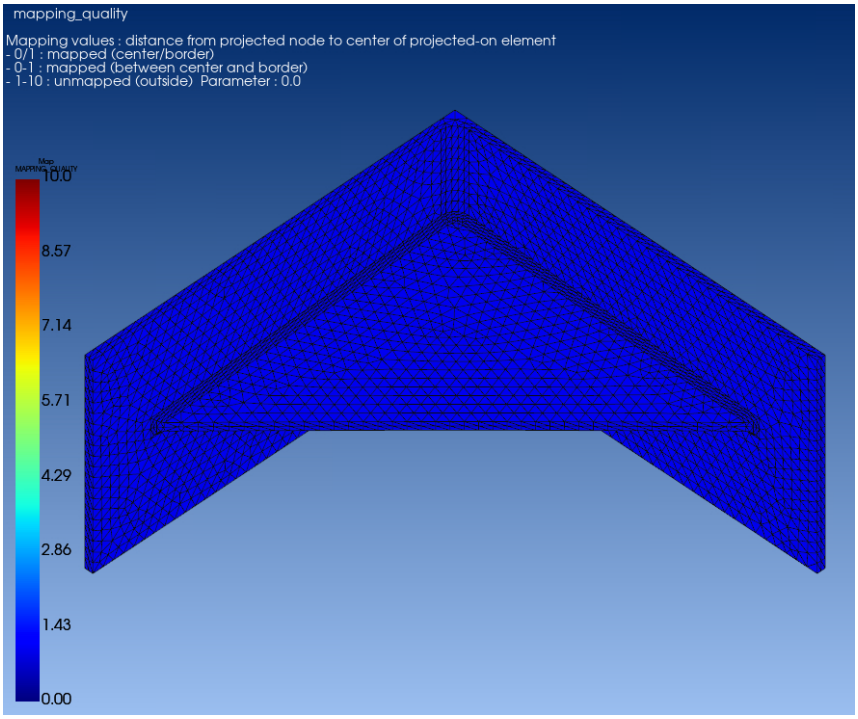

Figure 5.2: Mapping quality of BC mesh in Actran of a rib of type M1 single.

From Figure 5.2, it can be observed that the mapping quality of BC mesh is high (represented in blue) for all nodes on the surface of a rib of type M1 single. Finally, there is also the fact that the comparisons between the different models are based on the relative differences and not strictly the actual simulated values, which means that the comparisons can be done.

5.3 Research questions

Which acoustic variables affect the radiated sound power from a vibrating rib structure?

An equation that describes the radiated sound from a vibrating rib structure based on several factors can be formulated:

$$W_{ac} = \sigma W_{ERP} = \frac{1}{2}\sigma\rho_0 c_0 S v^2 \tag{2.16}$$

This equation, Equation 2.16, has proved to be essential to investigate the radiated power from a vibrating structure since this equation contains several important factors, see Chapter 2.2.3 for more details. The two most important factors are the radiation efficiency, σ, and the mean square velocity of the vibrating structure, v^2. However, it was difficult to find general trends for the radiation efficiency, but it can still be concluded that the geometry of the structure affects the efficiency. This means the radiation efficiency must be calculated or simulated for each case. Furthermore, v^2 only affects the radiated power when it increases significantly i.e., at the first bending mode of the structure, this makes it difficult to estimate as the radiation efficiency is frequency dependent. Because of these factors, the equation can not simply be applied to an arbitrary rib structure to calculate the radiated power without performing simulations beforehand. However, some rules of thumb can formulated, for example, the bending stiffness of the rib structure will determine the frequency of the largest peak of the radiated power. But, if the mean square velocity and the radiation efficiency are known as a function of frequency, the radiated power can be calculated using Equation 2.16. The usefulness of this equation is to explain differences in the radiated power in terms of the radiation efficiency and the mean square velocity.

How should acoustic simulations of vibrating rib structures be performed?

Acoustic simulations of a vibrating rib structure can be performed in many ways and with different boundary conditions. Which boundary condition to use was investigated during this thesis and a velocity condition was found to be the most representative of what a rib is exposed to in a real application. This can be motivated by the fact that from a complete EDU's point of view, a rib is a small part of the whole housing, both in terms of dimension and mass. A Model 1 rib with dimensions X=Y=250 mm and a thickness of 4 mm (no draft angle) has a volume of 125 000 mm^3, which corresponds to a weight of about 338 g. This means that a single rib does not influence the movement of the housing significantly, and this approximation can be done. This is because a complete EDU housing can weigh up to about 50 kg, which means that a rib that weighs 338 g is less than 0.7% of the total weight. Furthermore, the stiffness from a rib is in the x- and y-direction, in this case, and not in the z-direction in which they move, according to the velocity boundary condition. Since the stiffness does not act in the same direction

as the movement, this aspect will not affect the movement significantly either. The pros and cons of other boundary conditions are discussed in Chapters 3.2.2 and 5.2.1.

In terms of what program to use to perform the simulations, most finite element solver programs can likely be used, but they may lack some functionality found in Actran. The main reason for using Actran was the function Exterior Acoustic, which automatically generates the acoustic mesh with different mesh element sizes for different wavelengths. Such a function does not exist in every program, nor does it have the ability to get the radiation efficiency directly from the simulations. The efficiency is possible to calculate from the fraction between the acoustic radiated power, W_{ac}, and the equivalent radiated power, W_{ERP}, as shown in Equation 2.15, but this adds an extra step when analyzing the results. Finally, Actran is a finite element solver focused on acoustics, making it convenient for this type of analysis but not a requirement.

How do different geometrical properties of ribs, such as dimensions and curvatures, affect the radiated sound?

The geometrical property that affects the radiated sound the most has been observed to be the area of the rib structure. This was expected since the radiated power is proportional to the area of the vibrating structure, $W_{ac} \propto S$, according to Equation 2.16. This effect can be observed for the area variation of M1 single, where there is a difference of almost 31 dB in the radiated power between the largest and smallest rib. A reduction of 30 dB is equivalent to one-thousandth of the original power. This is a huge improvement if the goal is to minimize the radiated sound of a structure, but the ribs have other requirements that need to be met, such as a specified stiffness. However, the conclusion can still be drawn: *a smaller rib is better from an acoustic perspective than a larger rib.* With this knowledge in mind, the goal should be to design a rib that has the smallest area possible while meeting all the other requirements of that specific rib.

As discussed above, the area is the geometrical property that affects the radiated sound the most, however, other properties were shown to affect the radiated sound as well. An example of this is adding a small curvature to the outer edge which can reduce the maximum radiated power by about 3 dB, see Figure 4.13, note that this is for a rib size of X=Y=150 mm, it will be different for other sizes. This may not seem like a significant improvement, but a reduction of 3 dB equals a reduction in sound power of 50%. In summary, adding a small curvature to the outer edge can decrease the radiated sound, this applies to both M1 single and M2 single. This is an important finding since a small curvature does not affect the area of the rib significantly or the stiffness of the rib.

Finally, a trend between the dimensions of the ribs and the thickness of the ribs on the radiated power was observed for M1 single when no draft angle was applied. It was found that some thicknesses resulted in a higher peak in the radiated power compared to other thicknesses. For example, a rib with X=Y=120 mm and

a thickness of 4 mm, which is often used, resulted in a maximum radiated power of 85.1 dB. While a thickness of 6 mm resulted in a maximum value of 83.1 dB, and a thickness of 2 mm has a maximum value of 71.6 dB, see Figure 4.22. Using a thickness of 2 mm will give the best acoustic performance but would likely make the stiffness of the rib too low. For this particular rib, increasing the thickness to 6 mm would be beneficial, resulting in a reduction of 2 dB. If looking at a different dimension, X=Y=100 mm, a thickness of 3 mm is instead the worst, see Figure 4.20. This seems to be the trend, if the dimension of the rib increases then the thickness which radiates the most sound also increases, see also A.26, A.30 and A.34. How a draft angle would affect this relationship has not been investigated, but it is likely to produce the same effect but different values since the draft angle increases the average thickness of the rib. Finally, these results give an insight into the relation between the thickness of a rib and the dimension. This calls for an investigation of each rib to find the optimal thickness.

Can adjacent ribs interact acoustically with each other?

In Figures 4.54, 4.58, and 4.60, it can be observed that for some distances and angles that the radiated power increases significantly compared to other values. From these observations, it is clear that, in this case, two ribs can interact and produce what could be classified as an acoustic resonator. This indicates that when designing an EDU housing with two ribs in close proximity, analysis should be done beforehand to ensure that the distance or angle between the ribs does not cause resonance. Since this thesis did not find a direct relationship between the dimensions of the ribs and the angle or distance between the ribs, this should be done for each case.

5.4 Recommendations for future research

For future research, it would be interesting to verify the findings of the thesis by performing acoustic measurements on physical models, ideally using the ISO3744 standard. Since the simulations were done using a velocity boundary condition, which is not possible to perform experimentally, the results will not be directly comparable but may show the same reduction in the radiated sound as observed in the simulations. To make the experiments more comparable to the simulations done in this thesis, a point load, which is similar to a knock test, could be used instead of the velocity boundary condition. Furthermore, it could also be beneficial to investigate the other boundary conditions mentioned in this thesis and see how this would affect the result. In terms of the stiffness of the boundary, it would also be beneficial to find a representative value instead of using an infinite stiffness. Finally, a clear relationship between the geometrical properties and the radiation efficiency could not be observed. To understand this relationship better, a closer study of how the radiation efficiency depends on the geometry should be conducted. By having a better understanding, it could be possible to design the rib so that the peak in radiation efficiency occurs at a frequency outside a specified frequency range. Similarly, avoid a match between the frequency of the first bending mode and a peak in the radiation efficiency.

Another recommendation is to investigate more models or other variations of the ones investigated in this thesis. An example of this could be a version of M2 single with a cylinder that could be moved along the length of the rib. This is visualized in Figure 5.3 below:

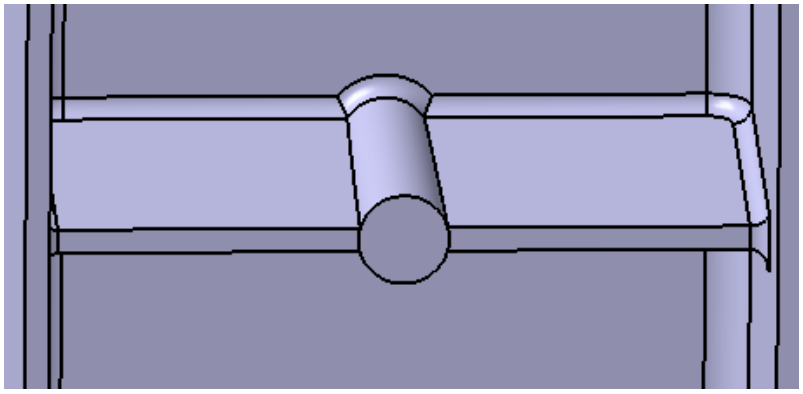

Figure 5.3: Example of a new version of M2 with a cylinder that can split the rib into two smaller ribs.

The theory behind this example model is that the cylinder can split the rib into two smaller ribs which could reduce the radiated power for some positions along the rib. This is based on the fact that the dimensions of the rib can affect the radiation efficiency [10], so dividing the rib into two smaller ribs could help reduce the radiated power. A similar split could be done for M1 double, with a third rib in the middle that divides the cavity between the ribs into two smaller cavities. This example is visualized in Figure 5.4 below:

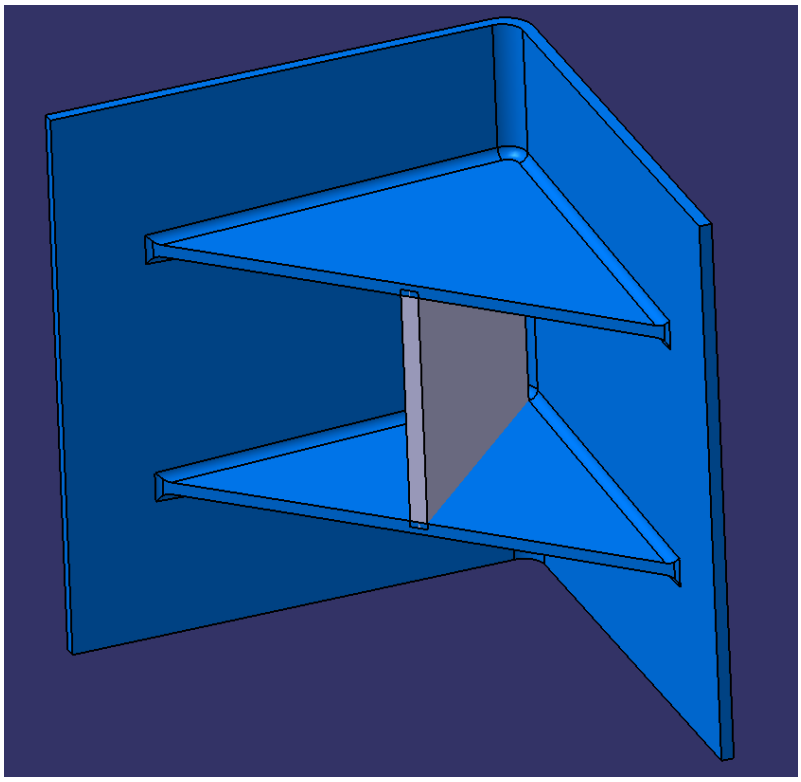

Figure 5.4: Example of a new version of M1 double with a rib that connects the two ribs with a third rib, marked in gray, in the middle.

Dividing the cavity between the ribs into two smaller cavities could reduce the radiated sound in cases where acoustics resonance occurs. If it can be concluded that placing a third rib between the ribs reduces the radiated sound, this design could be implemented since it would likely increase the stiffness compared to two parallel ribs. It would also be interesting to investigate the effect of different types of sound-deadening materials, such as foams, placed in the cavity between the ribs and simulate how this would affect the radiated power. This could be useful in cases when two ribs are required to be placed adjacent to each other.

Furthermore, it would be interesting to perform similar simulations as the angle variations for M1 double, but keeping one of the ribs straight, no angle, as illustrated in Figure 5.5 below:

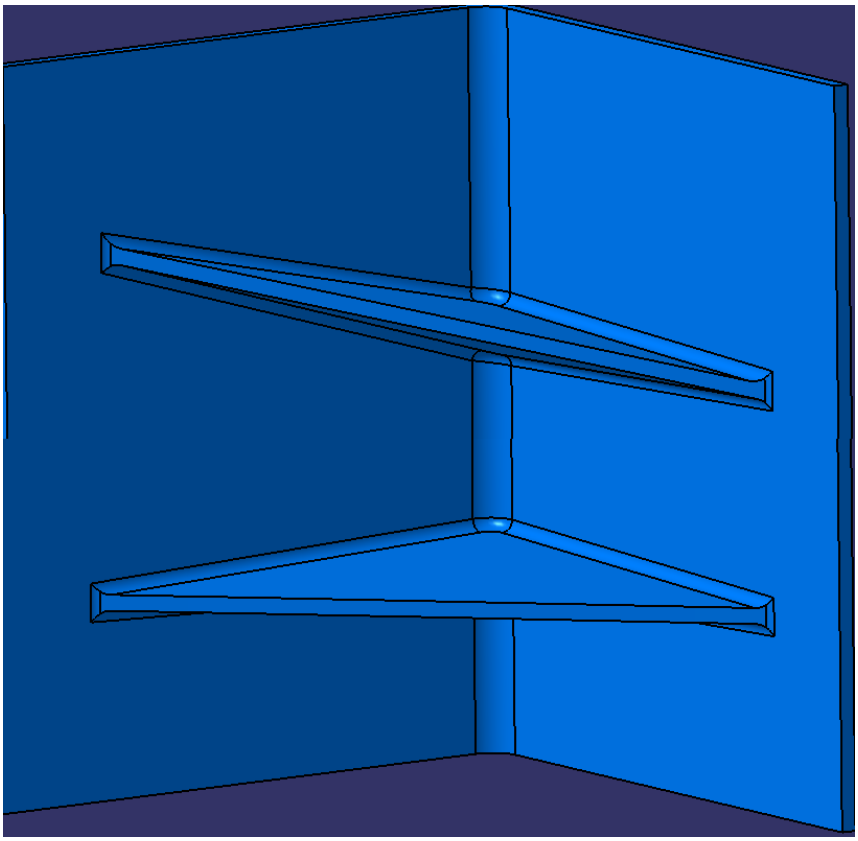

Figure 5.5: Example of a new version of M1 double, where one rib is kept straight, no angle, and the other can have a different angle.

The results from such a model would be interesting because if it can be shown that some angles reduce the radiated sound, it would be easier to implement in the design of a housing. This is due to the fact that it is easier to only move one of the ribs compared to changing the position of both ribs. Furthermore, it could be interesting to investigate how ribs of different sizes interact in this context.

Finally, it could be beneficial to investigate how three or more ribs would interact with each other. For this model, it would be possible to vary the angle and distance between the ribs separately, which would give more combinations to simulate, which could generate interesting results. By performing these simulations, an optimal combination could be found regarding how to place the ribs in relation to each other. A model like this would represent the existing ribs, which can be seen in the figure below:

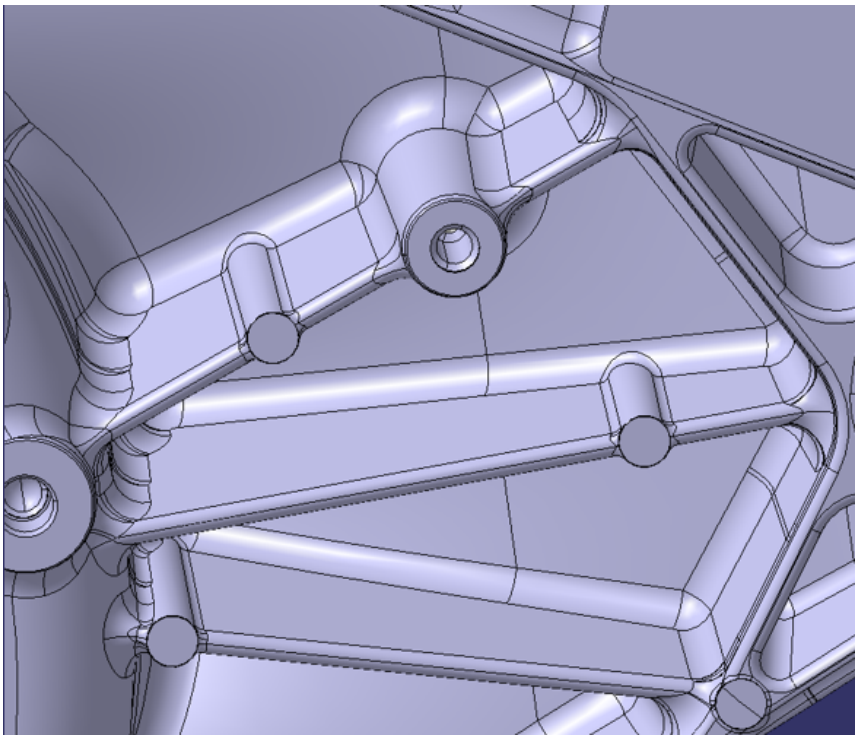

Figure 5.6: Example of a new model with three or more ribs to investigate the interaction between more than two ribs.

In terms of the simulation of the different parameters, it would be interesting to investigate a combination of the different parameters applied to a rib. For example, increasing the ratio between X and Y for M1 single makes the rib elongated while adding a curvature to the outer edge. By combining the effect of different variations at the same time, it could be possible to further decrease the peak in the radiated power.

6
Conclusion

The purpose of this thesis was to investigate how the geometrical proprieties of ribs affect the acoustics of the ribs. The main objective was to find relationships between different rib design concepts and how these concepts can be used to minimize the radiated sound.

One observation that could be made for each type of rib geometry variation is that the frequency of the first bending mode is highly dependent on the geometry, which affects the bending stiffness. Meanwhile, radiation efficiency seems to be more dependent on the geometry of the structure rather than on the stiffness. The fact that the frequency of the first bending mode is highly dependent on the geometry is an important aspect since the first bending mode can be shifted in frequency to a frequency with a lower excitation level. This would be beneficial since the effect of the mode would be decreased, resulting in a lower radiated power. In this thesis, we have used a constant level of excitation across the whole frequency range, which means that this aspect could not be investigated. If a high excitation level cannot be avoided, effort should be put into placing the frequency of the first bending mode on excitation frequencies associated with high-speed driving. At higher speeds, the ambient sound level is higher due to increased tire and wind noise, which will help mask the sound from the EDU, and therefore, the problem is minimized. In summary, the frequency of the first bending mode should be outside of the excitation frequencies associated with cruising speed since it is at this speed that the vehicle is typically operated. Therefore, it is especially crucial not to have any unwanted sounds in this situation. Finally, by moving the first bending mode in frequency, high radiation efficiency values can be avoided. This was something that was done in Figure 4.13, which reduced the radiated sound.

Using simple parameterized models, several different rib geometries can be created, and their acoustic performance can be compared. The benefit of parameterized models is that several variations can be performed quickly. With a few adjustable parameters, several geometrical properties can be investigated.

It is recommended to use a velocity boundary condition of the structure to perform acoustic simulations of rib structures to ensure that each rib has an equivalent excitation regardless of geometry or mass. Contrary to other boundary conditions, such as a distributed load, which causes different ribs to have different displacements, The reason why the displacements differ for different ribs is the fact that for a constant force, the mass of the rib will affect the acceleration. Furthermore, a velocity

condition is more representative of how a rib moves in relation to a complete EDU, which is due to the low mass of the rib compared to the EDU. For example, the small mass of a single rib does not significantly affect the movement of the complete EDU, which is why this assumption can be made.

The two factors that affect the radiated power the most are the mean square velocity and the radiation efficiency. It was found that the velocity only affects the power significantly at the frequency of the first bending mode since, at the mode, the velocity increases significantly. Regarding radiation efficiency, it was difficult to find any pattern between the geometry of the rib and where the peak occurred. However, it can be concluded that the efficiency differs between geometry variations, and for this reason, it was found that the efficiency affects the radiated power more than the velocity. Due to the difficulties finding patterns in the radiation efficiency, a closer study should be conducted.

In terms of reducing the radiated sound, it was found that some rib geometries can be utilized to reduce the sound in some cases. The property that affects the radiated power the most is the area of the rib since the power is proportional to the area. For the area variation of M1 single, it was found that there is a difference of almost 31 dB in the radiated power between the largest and the smallest rib. It was also shown that adding a small curvature to the outer edge of the rib can, in some cases, reduce the radiated sound for both M1 single and M2 single. This effect was greater for larger ribs than the same implementation on smaller ribs. This is an important finding since a small curvature does not significantly affect the area of the rib or the rib's stiffness. Finally, there seems to be a relation between the dimensions of the rib and the thickness. It was shown that some thickness increases the radiated power while other thicknesses reduce the power. With this information, it is important to investigate what thickness to use for each rib to find the optimal thickness that both reduces the radiated power as well as meets the other requirements.

Bibliography

[1] Wikipedia (2009). *A-weighting*. Retrieved from: https://commons.wikimedia.org/wiki/File:Acoustic_weighting_curves_(1).svg?uselang=en#Licensing (retrieved: 2024-02-23).

[2] Folkhälsomyndigheten (2019). *Om ljud och buller*. Retrieved from: https://www.folkhalsomyndigheten.se/publikationer-och-material/publikationsarkiv/o/om-ljud-och-buller-/?pub=60517, (2024-02-29).

[3] SIEMENS (2019). *Sound Fields: Free versus Diffuse Field, Near versus Far Field*. Retrieved from: https://community.sw.siemens.com/s/article/sound-fields-free-versus-diffuse-field-near-versus-far-field (retrieved: 2024-02-17).

[4] Bill Webster (2021). *First-Order vs. Second-Order Elements In FEA*. Retrieved from: https://community.sw.siemens.com/s/article/sound-fields-free-versus-diffuse-field-near-versus-far-field, (2024-02-26).

[5] Volvo Cars (2021). *Volvo Cars to be fully electric by 2030*. Retrieved from: https://www.media.volvocars.com/global/en-gb/media/pressreleases/277409/volvo-cars-to-be-fully-electric-by-2030 (retrieved: 2024-05-10).

[6] Hexagon AB. *Actran 2023.2 User's Guide Vol. 1*. Hexagon AB, November 23, 2023.

[7] *Acoustics - Determination of sound power levels and sound energy levels of noise sources using sound pressure - Engineering methods for an essentially free field over a reflecting plane (ISO 3744:2010)*. Retrieved from: https://www.sis.se/produkter/maskinsakerhet-3f1691ec/buller-och-matmetod/sseniso37442010/ (retrieved:2024-05-01).

[8] R.D. Blevins. *Formulas for natural frequency and mode shape (Reprint ed.)* Krieger Pub Co, 2001.

[9] J. Österman C. Nordling. *Physics Handbook for Science and Engineering*. Studentlitteratur AB, 2006. ISBN: 9789144044538.

[10] J.B. Fahnline and S. Hambric. *Structural Acoustics Tutorial—Part 2: Sound—Structure Interaction*. 2007. DOI: 10.1121/1.2961152.

[11] F. Jacobsen. *An elementary introduction to acoustics*. 2011.

[12] W. Kropp. *Progagation and radiation borne sound*. 2015.

[13] Paul M. Kurowski. *Finite Element Analysis for Design Engineers (3rd Edition)*. SAE International, 2023. ISBN: 978-1-4686-0535-8.

[14] R.G. White. *Noise and Vibration*. Halsted Press, 1982.

A

Appendix 1

A.1 NASTRAN header

```
SOL 111 $Modal frequency response
CEND
$$$$$$$$$$$$$$$$$$$$
SPC=11
METHOD=10
SDAMPING=200
SUBCASE 1
ANALYSIS=MODES $Calculates the modes
DISP(PLOT)=ALL
SUBCASE 2
DISP(PUNCH)=44 $Nodal displacement of Set with ID=44, all surface nodes.
FREQ=12
DLOAD=13
$$$$$$$$$$$$$$$$$$$$
BEGIN BULK
TABDMP1,200,CRIT,
+,0.,0.03,2500.,0.03,ENDT $Definies the material damping of 3%.
SPC1,11,123456,1.
$Defines the velocity condition, in direction 3 (z) with magnitude=1.
$Node ID=1 refers to the RBE2
SPCD,30,1,3,1.0
RLOAD1         13      30                      1.               VELO
FREQ1          12    100.     20.     295
FREQ4          12   1000.   6000.     0.1       5
$Calculates 5 extra points around the modes within 10% of the frequency of the mode.
EIGRL          10    100.  10000.               0                MASS
MDLPRM,HDF5,0
PARAM,POST,1
```

Figure A.1: The NASTRAN header used for the displacement calculations.

A.2 Actran model

A.2.1 Analysis tree

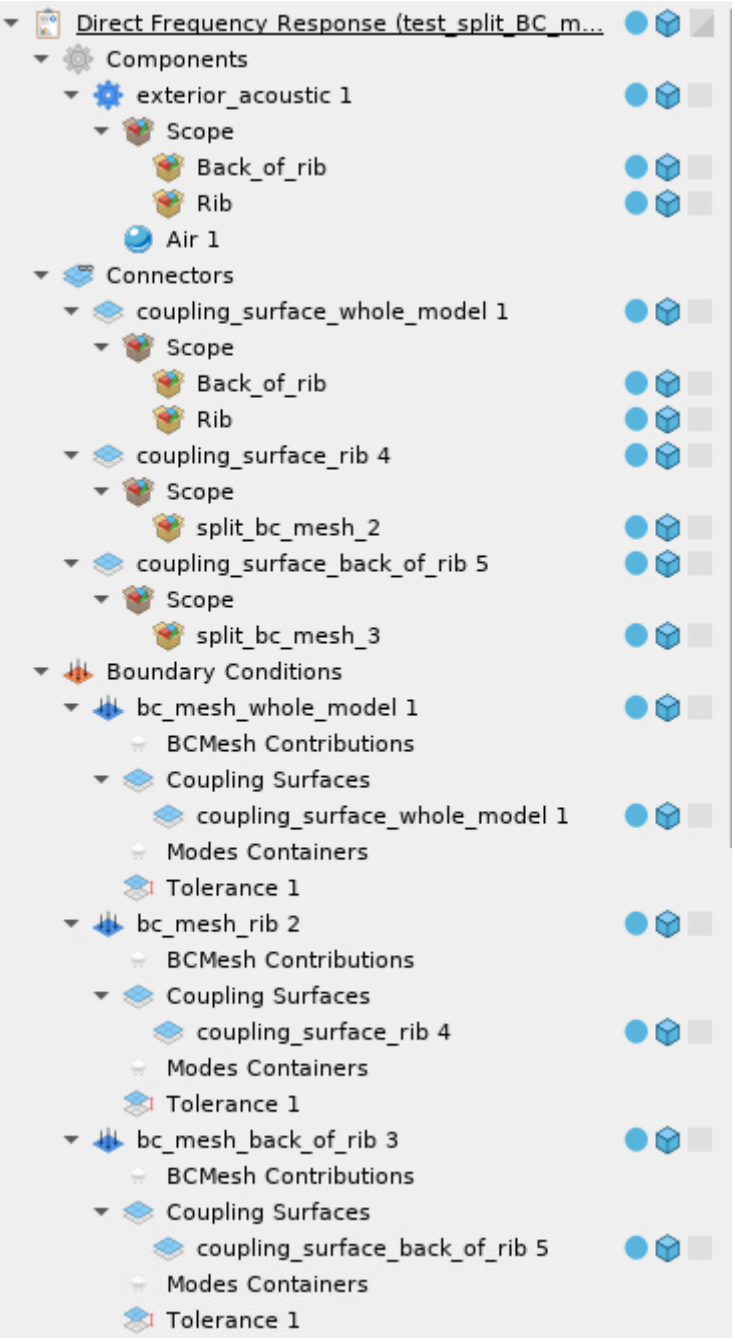

Figure A.2: Analysis tree in Actran.

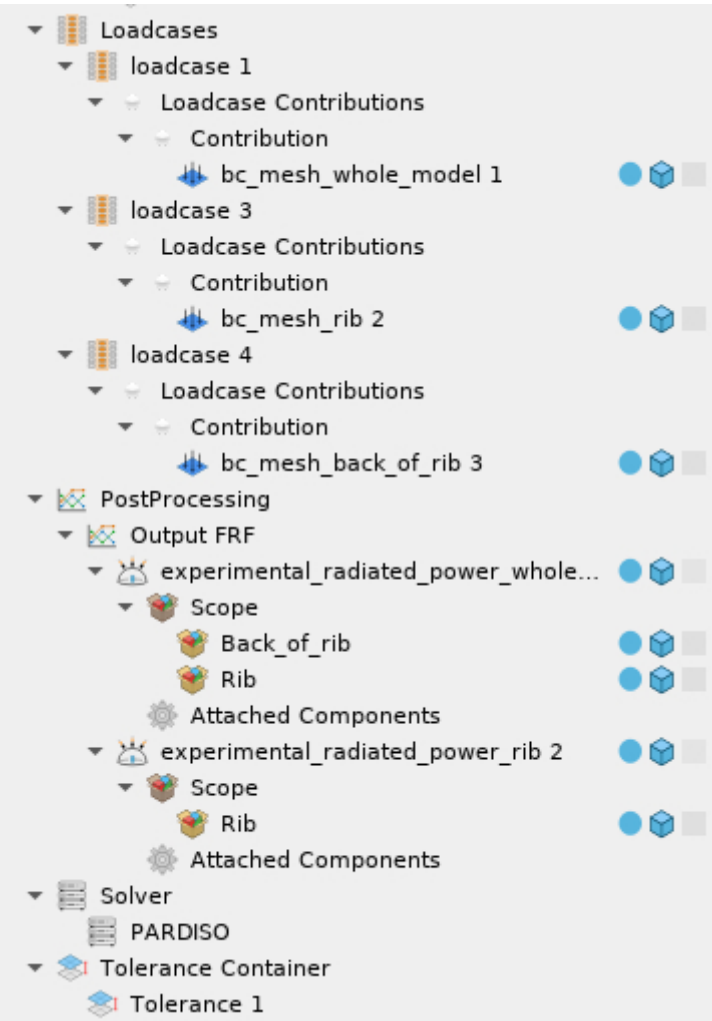

Figure A.3: Analysis tree in Actran.

A.2.2 Exterior acoustics

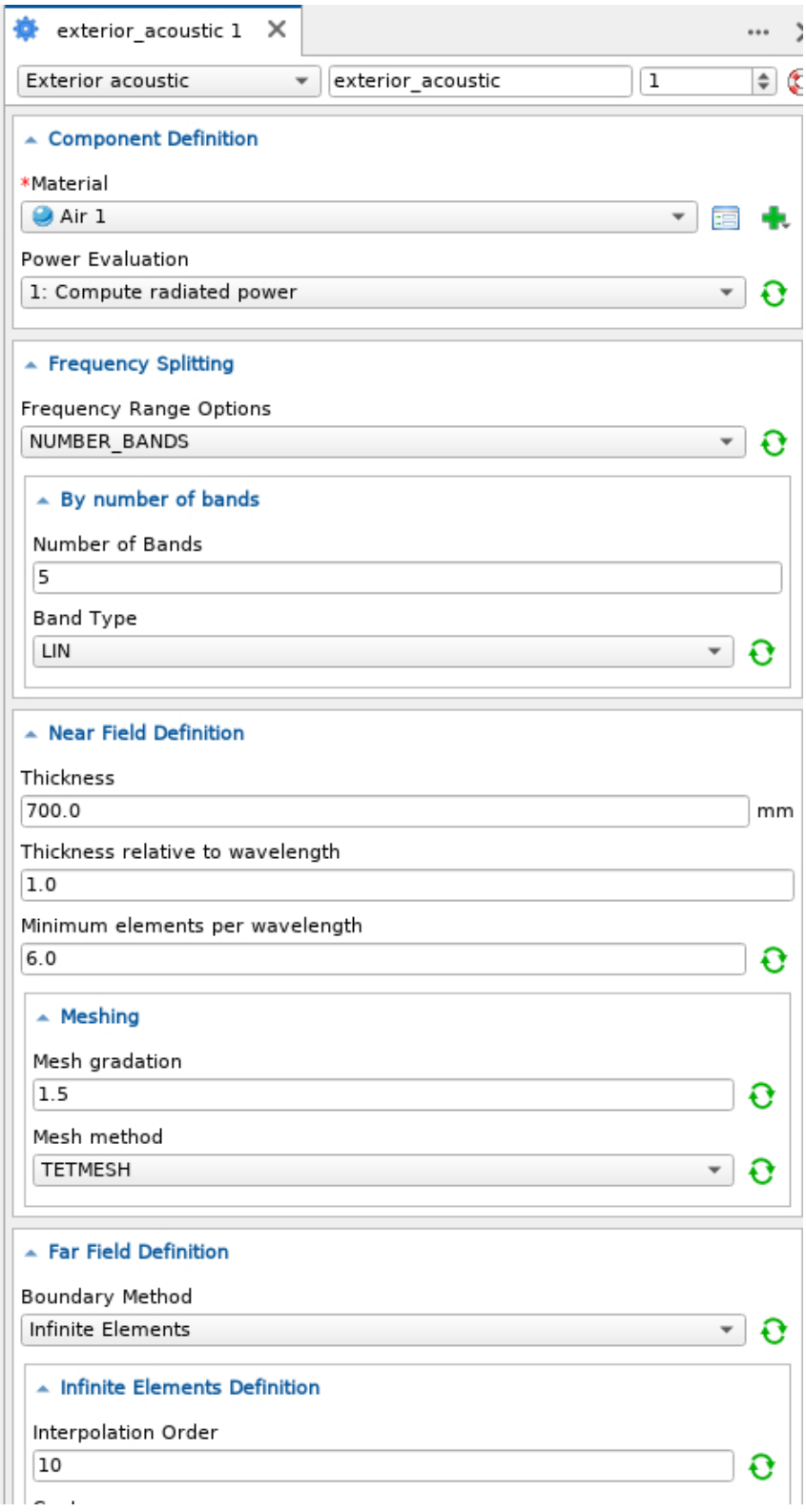

Figure A.4: Settings used for the exterior acoustics in Actran.

A.2.3 BC mesh

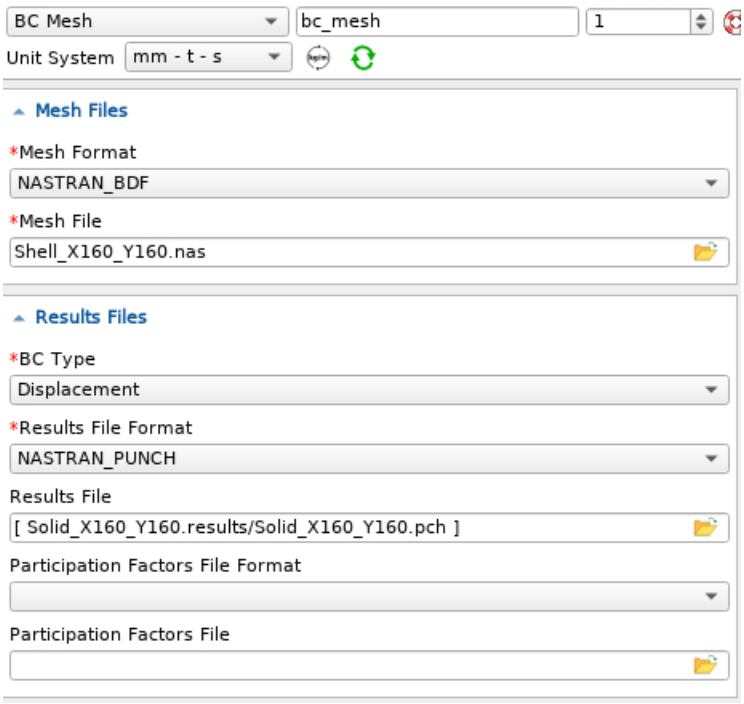

Figure A.5: Settings used for the BC mesh in Actran.

A.2.4 Experimental radiated power (ISO3744)

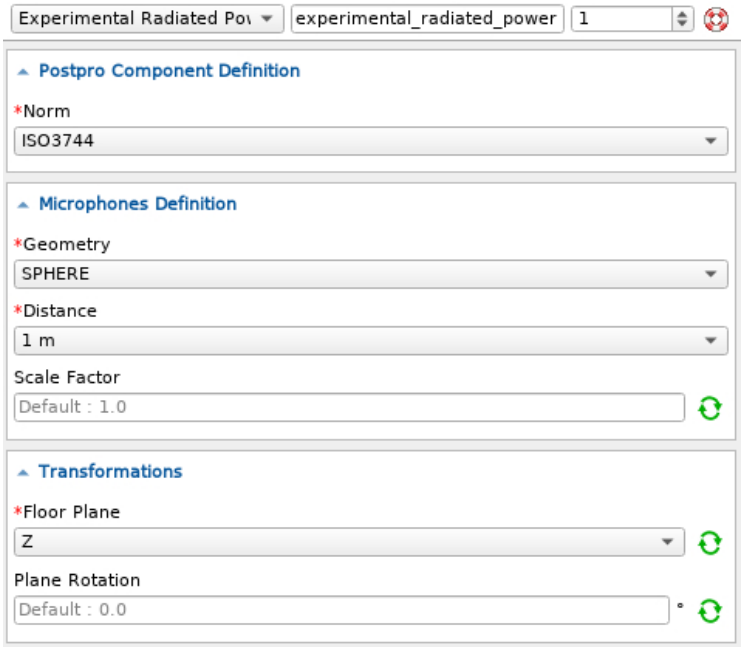

Figure A.6: Settings used for the experimental radiated power (ISO3744) in Actran.

A.2.5 Definition of rib surface

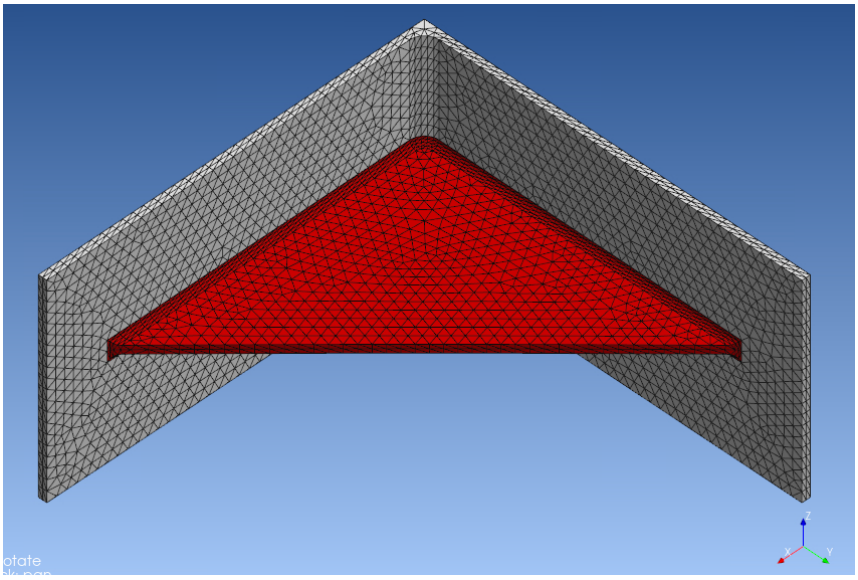

Figure A.7: Definition of rib surface in Actran. The surface marked in red represents the area S in Equation 2.16.

A.3 Bending modes for each model

In the tables below, the fist three bending modes are presented. The modes which has a frequency above 10 000 Hz or was difficult to classify, are denoted as "-".

A.3.1 Model 1-Single rib (M1 single)

The base model, X=Y=120 mm and R=10 000 mm, has the following first three bending modes: mode 1 at 2512 Hz, mode 2 at 4791 Hz and mode 3 at 6866 Hz.

A.3.1.1 Area variation with X=Y and no curvature (R=10 000 mm) on the outer edge

Table A.1: Bending modes for area variation with X=Y and no curvature (R=10 000 mm) on the outer edge

Dimensions	First mode	Second mode	Third mode
X=Y=50 mm	7613 Hz	8320 Hz	-
X=Y=75 mm	4080 Hz	6732 Hz	7838 Hz
X=Y=100 mm	3258 Hz	5933 Hz	7625 Hz
X=Y=110 mm	2836 Hz	5324 Hz	7239 Hz
X=Y=120 mm (base model)	2512 Hz	4791 Hz	6866 Hz
X=Y=130 mm	2226 Hz	4276 Hz	6269 Hz
X=Y=140 mm	2001 Hz	3856 Hz	5744 Hz
X=Y=150 mm	1814 Hz	3497 Hz	5251 Hz
X=Y=200 mm	1215 Hz	2319 Hz	3501 Hz
X=Y=250 mm	902 Hz	1698 Hz	2545 Hz

A.3.1.2 Constant area with X≠Y and no curvature (R=10 000 mm) on the outer edge

Table A.2: Bending modes for constant area, 7200 mm^2 based on the base model (X=Y=120 mm), with X≠Y and no curvature (R=10 000 mm) on the outer edge..

Dimensions	First mode	Second mode	Third mode
X=Y=120 mm (base model)	2512 Hz	4791 Hz	6866 Hz
X=60 mm and Y=240 mm	3665 Hz	5610 Hz	6774 Hz
X=80 mm and Y=180 mm	3015 Hz	5186 Hz	6862 Hz
X=100 mm and Y=144 mm	2669 Hz	4944 Hz	6889 Hz

Table A.3: Bending modes for constant area, 7200 mm^2 based on the base model (X=Y=120 mm), with X≠Y and no curvature (R=10 000 mm) on the outer edge (no draft angle).

Dimensions	First mode	Second mode	Third mode
X=Y=120 mm (base model)	1739 Hz	3686 Hz	5945 Hz
X=60 mm and Y=240 mm	2190 Hz	3615 Hz	5084 Hz
X=80 mm and Y=180 mm	1873 Hz	3535 Hz	5352 Hz
X=100 mm and Y=144 mm	1764 Hz	3631 Hz	5501 Hz

Table A.4: Bending modes for constant area, 3600 mm^2, with X≠Y and no curvature (R=10 000 mm) on the outer edge.

Dimensions	First Mode	Second mode	Third mode
X=50 mm and Y=144 mm	4894 Hz	6864 Hz	8390 Hz
X=60 mm and Y=120 mm	4559 Hz	6930 Hz	8324 Hz
X=72 mm and Y=100 mm	4288 Hz	6913 Hz	8256 Hz
X=80 mm and Y=90 mm	4175 Hz	6865 Hz	8212 Hz
X=Y=84.85 mm	4127 Hz	6827 Hz	8178 Hz

Table A.5: Bending modes for constant area, 12800 mm^2, with X≠Y and no curvature (R=10 000 mm) on the outer edge.

Dimensions	First Mode	Second mode	Third mode
X=80 mm and Y=320 mm	2644 Hz	4257 Hz	5691 Hz
X=100 mm and Y=256 mm	2189 Hz	3782 Hz	5375 Hz
X=128 mm and Y=200 mm	1839 Hz	3421 Hz	5102 Hz
X=160 mm and Y=160 mm	1656 Hz	3189 Hz	4808 Hz

A.3.1.3 Curvature on outer edge (R) variation with X=Y=120 mm

Table A.6: Bending modes for curvature on outer edge (R) variation with X=Y=120 mm.

Dimensions	First Mode	Second mode	Third mode
R=151 mm	4348 Hz	6325 Hz	7145 Hz
R=200 mm	3687 Hz	5960 Hz	7105 Hz
R=250 mm	3370 Hz	5705 Hz	7066 Hz
R=300 mm	3186 Hz	5534 Hz	7032 Hz
R=400 mm	2981 Hz	5325 Hz	6982 Hz

A.3.1.4 Constant area, 9750 mm^2, by changing R with X=Y

Table A.7: Bending modes for constant area, 9750 mm^2, by changing R with X=Y.

Dimensions	First Mode	Second mode	Third mode
X=Y=150 mm and R=532 mm	2141 Hz	3958 Hz	5691 Hz
X=Y=160 mm and R=327 mm	2262 Hz	4054 Hz	5676 Hz
X=Y=165 mm and R=287.5 mm	2315 Hz	4099 Hz	5679 Hz
X=Y=170 mm and R=262.7 mm	2361 Hz	4119 Hz	5684 Hz

A.3.1.5 Thickness, T, variation for different dimensions with X=Y and no draft angle

Table A.8: Bending modes for thickness, T, variation for X=Y=100 mm and no draft angle.

Dimensions	First mode	Second mode	Third mode
T=2 mm	1478 Hz	3195 Hz	5580 Hz
T=3 mm	2036 Hz	4282 Hz	-
T=4 mm	2437 Hz	4967 Hz	-
T=5 mm	2703 Hz	5415 Hz	-
T=6 mm	2881 Hz	5779 Hz	-

Table A.9: The first three bending modes for thickness, T, variation for X=Y=120 mm and no draft angle.

Dimensions	First mode	Second mode	Third mode
T=2 mm	1024 Hz	2222 Hz	4009 Hz
T=3 mm	1430 Hz	3065 Hz	5245 Hz
T=4 mm	1739 Hz	3686 Hz	5945 Hz
T=5 mm	1957 Hz	4137 Hz	6518 Hz
T=6 mm	2109 Hz	4495 Hz	-

Table A.10: The first three bending modes for thickness, T, variation for X=Y=130 mm and no draft angle.

Dimensions	First mode	Second mode	Third mode
T=2 mm	872 Hz	1893 Hz	4641 Hz
T=3 mm	1224 Hz	2634 Hz	4616 Hz
T=4 mm	1497 Hz	3199 Hz	5390 Hz
T=5 mm	1694 Hz	3622 Hz	5978 Hz
T=6 mm	1835 Hz	3962 Hz	6537 Hz

Table A.11: The first three bending modes for thickness, T, variation for X=Y=140 mm and no draft angle.

Dimensions	First mode	Second mode	Third mode
T=2 mm	751 Hz	1633 Hz	2966 Hz
T=3 mm	1060 Hz	2286 Hz	4058 Hz
T=4 mm	1303 Hz	2798 Hz	4839 Hz
T=5 mm	1482 Hz	3190 Hz	5437 Hz
T=6 mm	1611 Hz	3507 Hz	5982 Hz

Table A.12: The first three bending modes for thickness, T, variation for X=Y=150 mm and no draft angle.

Dimensions	First mode	Second mode	Third mode
T=2 mm	654 Hz	1421 Hz	2584 Hz
T=3 mm	926 Hz	2001 Hz	3580 Hz
T=4 mm	1144 Hz	2466 Hz	4331 Hz
T=5 mm	1307 Hz	2826 Hz	4920 Hz
T=6 mm	1426 Hz	3120 Hz	5446 Hz

A.3.2 Model 2-Single rib (M2 single)

The base model, X=120, Y1=Y2=60 mm, and R=10 000 mm, has the following three first bending modes: mode 1 at 2480 Hz, mode 2 at 5197 Hz and mode 3 at 7814 Hz.

A.3.2.1 Area variation with X=2Y1=2Y2

Table A.13: Area variation with X=2Y1=2Y2 and no curvature (R=10 000 mm) on the outer edge, the three first bending modes.

Dimensions	First mode	Second mode	Third mode
X=50 mm and Y1=Y2=25 mm	-	-	-
X=100 mm and Y1=Y2=50 mm	3344 Hz	6829 Hz	-
X=150 mm and Y1=Y2=75 mm	1734 Hz	3640 Hz	6170 Hz
X=200 mm and Y1=Y2=100 mm	1111 Hz	2302 Hz	3995 Hz
X=250 mm and Y1=Y2=125 mm	797 Hz	1629 Hz	2817 Hz

A.3.2.2 Constant area with Y1≠Y2 and no curvature (R=10 000 mm) on the outer edge

Table A.14: Constant area with X=120 mm, Y1≠Y2, and no curvature (R=10 000 mm) on the outer edge. 7200 mm^2, same area as the base model, the three first bending modes.

Dimensions	First mode	Second mode	Third mode
X=120 mm and Y1=Y2=60 mm (base model)	2480 Hz	5197 Hz	7814 Hz
X=120 mm, Y1=70 mm, and Y2=50 mm	2475 Hz	5171 Hz	7808 Hz
X=120 mm, Y1=80 mm, and Y2=40 mm	2462 Hz	5099 Hz	7759 Hz
X=120 mm, Y1=90 mm, and Y2=30 mm	2450 Hz	4996 Hz	7616 Hz

Table A.15: Constant area with X=100 mm, Y1≠Y2, and no curvature on the outer edge (R=10 000 mm), 3600 mm^2, the three first bending modes.

Dimensions	First mode	Second mode	Third mode
X=100 mm, Y1=Y2=36 mm	4157 Hz	7781 Hz	-
X=100 mm, Y1=46 mm, and Y2=26 mm	4142 Hz	7591 Hz	-
X=100 mm, Y1=56 mm, and Y2=16 mm	4112 Hz	7230 Hz	-
X=100 mm, Y1=66 mm, and Y2=6 mm	4091 Hz	7091 Hz	-

Table A.16: Constant area with X=160 mm, Y1≠Y2, and no curvature (R=10 000 mm) on the outer edge, 12800 mm^2, the three first bending modes.

Dimensions	First mode	Second mode	Third mode
X=160 mm, Y1=Y2=80 mm	1567 Hz	3282 Hz	5627 Hz
X=1 mm, Y1=46 mm, and Y2=26 mm	4142 Hz	7591 Hz	-
X=100 mm, Y1=56 mm, and Y2=16 mm	4112 Hz	7230 Hz	-
X=100 mm, Y1=66 mm, and Y2=6 mm	4091 Hz	7091 Hz	-

A.3.2.3 Curvature on outer edge (R) variation with X=120 mm and Y1=Y2=60 mm

Table A.17: Bending modes for curvature on outer edge (R) variation with X=120 mm and Y1=Y2=60 mm, the three first bending modes.

Dimensions	First Mode	Second mode	Third mode
R=62 mm	6419 Hz	7466 Hz	-
R=70 mm	4855 Hz	6674 Hz	7657 Hz
R=80 mm	4081 Hz	6206 Hz	7668 Hz
R=90 mm	3710 Hz	5978 Hz	7681 Hz
R=100 mm	3486 Hz	5839 Hz	7690 Hz
R=150 mm	3024 Hz	5553 Hz	7731 Hz
R=200 mm	2857 Hz	5449 Hz	7751 Hz

A.3.2.4 Constant area, 5000 mm^2, by changing R with X=2Y1=2Y2

Table A.18: Constant area, 5000 mm^2, by changing R with X=2Y1=2Y2, the three first bending modes.

Dimensions	First mode	Second mode	Third mode
X=110 mm, Y1=Y2=55 mm, and R=268.72 mm	3131 Hz	6117 Hz	8130 Hz
X=120 mm, Y1=Y2=60 mm, and R=105.93	3392 Hz	5780 Hz	7697 Hz
X=140 mm, Y1=Y2=70 mm, and R=80.72 mm	4027 Hz	5472 Hz	7034 Hz
X=160 mm, Y1=Y2=80 mm, and R=83.74 mm	4705 Hz	5460 Hz	6701 Hz

A.3.3 Model 1-Single rib corner (M1 single corner)

The base model, X=240 mm, Y=120 mm,$\alpha_1 = \alpha_2 = 80°$, and R=50 mm, has the following first three bending modes: mode 1 at 815 Hz, mode 2 at 1423 Hz, and mode 3 at 2418 Hz.

A.3.3.1 α_1 variation with X=240 mm, Y=120 mm, α_2=80°, and R=50 mm

Table A.19: α_1 variation with X=240 mm, Y=120 mm, α_2=80°, and R=50 mm, the first three bending modes.

Dimensions	First mode	Second mode	Third mode
$\alpha_1 = 28°$	1362 Hz	2482 Hz	3777 Hz
$\alpha_1 = 30°$	1245 Hz	2337 Hz	3602 Hz
$\alpha_1 = 35°$	1039 Hz	2149 Hz	3414 Hz
$\alpha_1 = 40°$	942 Hz	1997 Hz	3167 Hz
$\alpha_1 = 45°$	892 Hz	1846 Hz	3046 Hz
$\alpha_1 = 55°$	847 Hz	1638 Hz	2832 Hz
$\alpha_1 = 70°$	822 Hz	1480 Hz	2544 Hz
Base model: $\alpha_1 = 80°$	815 Hz	1423 Hz	2418 Hz

A.3.3.2 α_2 variation with X=240 mm, Y=120 mm, $\alpha_1 = 80°$, and R=50 mm

Table A.20: α_2 variation with X=240 mm, Y=120 mm, α_1=80°, and R=50 mm, the first three bending modes.

Dimensions	First mode	Second mode	Third mode
$\alpha_1 = 90°$	595 Hz	1258 Hz	2246 Hz
$\alpha_1 = 75°$	980 Hz	1614 Hz	2575 Hz
$\alpha_1 = 70°$	1171 Hz	1968 Hz	2946 Hz
Base model: $\alpha_1 = 80°$	815 Hz	1423 Hz	2418 Hz

A.3.3.3 R variation with X=240 mm, Y=120 mm, and $\alpha_1 = \alpha_2 = 80°$

Table A.21: R variation with X=240 mm, Y=120 mm, and $\alpha_1 = \alpha_2 = 80°$, the first three bending modes.

Dimensions	First mode	Second mode	Third mode
R=116 mm	847 Hz	1578 Hz	2634 Hz
R=90 mm	832 Hz	1509 Hz	2541 Hz
R=70 mm	823 Hz	1462 Hz	2475 Hz
Base model: R=50 mm	815 Hz	1423 Hz	2418 Hz
R=40 mm	812 Hz	1406 Hz	2393 Hz
R=20 mm	807 Hz	1382 Hz	2354 Hz

A.3.4 Model 1-Double rib (M1 double)

The base model, X1=X2=Y1=Y2=120 mm, R1=R2=10 000 mm, and d=40 mm, has the following first three bending modes where the ribs move in the same direction: mode 1 at 2727 Hz, mode 2 at 5381 Hz, and 6993 Hz. The first three bending modes where the ribs move in the opposite directions has the following frequencies: mode 1 at 2378 Hz, mode 2 at 4670 Hz, and mode 3 at 6779 Hz.

A.3.4.1 Area variation with X=Y and no curvature (R=10 000 mm) on the outer edge with Rib1=Rib2

Table A.22: Area variation with X=Y and no curvature (R=10 000 mm) on the outer edge with Rib1=Rib2. The first three bending modes where the ribs move in the same direction.

Dimensions	First mode	Second mode	Third mode
X=Y=50 mm	8188 Hz	-	-
X=Y=100 mm	3550 Hz	6971 Hz	7611 Hz
X=Y=150 mm	1987 Hz	3943 Hz	5512 Hz
X=Y=200 mm	1342 Hz	2137 Hz	5274 Hz

Table A.23: Area variation with X=Y and no curvature (R=10 000 mm) on the outer edge with Rib1=Rib2. The first three bending modes where the ribs move in the opposite direction.

Dimensions	First mode	Second mode	Third mode
X=Y=50 mm	7503 Hz	-	-
X=Y=100 mm	3103 Hz	5858 Hz	7787 Hz
X=Y=150 mm	1724 Hz	4639 Hz	5159 Hz
X=Y=200 mm	1154 Hz	2286 Hz	4631 Hz

A.3.4.2 Area variation with X=Y and no curvature (R=10 000 mm) on the outer edge with Rib1≠Rib2 and Rib1: X=Y=120 mm

Table A.24: Area variation with X=Y and no curvature (R=10 000 mm) on the outer edge with Rib1≠Rib2 and Rib1: X=Y=120 mm. The first three bending modes where the ribs move in the same direction.

Dimensions	First mode	Second mode	Third mode
Rib2: X=Y=50 mm	2409 Hz	4962 Hz	-
Rib2: X=Y=100 mm	3379 Hz	4891 Hz	-
Rib2: X=Y=150 mm	2593 Hz	5062 Hz	-
Rib2: X=Y=200 mm	1207 Hz	2209 Hz	3041 Hz

Table A.25: Area variation with X=Y and no curvature (R=10 000 mm) on the outer edge with Rib1≠Rib2 and Rib1: X=Y=120 mm. The first three bending modes where the ribs move in the opposite direction.

Dimensions	First mode	Second mode	Third mode
Rib2: X=Y=50 mm	-	-	-
Rib2: X=Y=100 mm	2496 Hz	6493 Hz	-
Rib2: X=Y=150 mm	1814 Hz	3638 Hz	5454 Hz
Rib2: X=Y=200 mm	2589 Hz	2758 Hz	-

A.3.4.3 Area variation with X=Y and no curvature (R=10 000 mm) on the outer edge with Rib1≠Rib2 and Rib1: X=Y=50 mm

Table A.26: Area variation with X=Y and no curvature (R=10 000 mm) on the outer edge with Rib1≠Rib2 and Rib1: X=Y=50 mm. The first three bending modes where the ribs move in the same direction.

Dimensions	First mode	Second mode	Third mode
Rib2: X=Y=50 mm	8188 Hz	-	-
Rib2: X=Y=100 mm	3168 Hz	6105 Hz	-
Rib2: X=Y=150 mm	1734 Hz	3005 Hz	5354 Hz
Rib2: X=Y=200 mm	1154 Hz	2227 Hz	2790 Hz

Table A.27: Area variation with X=Y and no curvature (R=10 000 mm) on the outer edge with Rib1≠Rib2 and Rib1: X=Y=50 mm. The first three bending modes where the ribs move in the opposite direction.

Dimensions	First mode	Second mode	Third mode
Rib2: X=Y=50 mm	7503 Hz	-	-z
Rib2: X=Y=100 mm	-	-	-
Rib2: X=Y=150 mm	-	-	-
Rib2: X=Y=200 mm	-	-	-

A.3.4.4 Area variation with X=Y and no curvature (R=10 000 mm) on the outer edge with Rib1≠Rib2 and Rib1: X=Y=200 mm

Table A.28: Area variation with X=Y and no curvature (R=10 000 mm) on the outer edge with Rib1≠Rib2 and Rib1: X=Y=200 mm. The first three bending modes where the ribs move in the same direction.

Dimensions	First mode	Second mode	Third mode
Rib2: X=Y=50 mm	1154 Hz	2227 Hz	2790 Hz
Rib2: X=Y=100 mm	1192 Hz	2224 Hz	2891 Hz
Rib2: X=Y=150 mm	1887 Hz	3691 Hz	5365 Hz
Rib2: X=Y=200 mm	1342 Hz	2137 Hz	5274 Hz

Table A.29: Area variation with X=Y and no curvature (R=10 000 mm) on the outer edge with Rib1≠Rib2 and Rib1: X=Y=200 mm. The first three bending modes where the ribs move in the opposite direction.

Dimensions	First mode	Second mode	Third mode
Rib2: X=Y=50 mm	-	-	-
Rib2: X=Y=100 mm	-	-	-
Rib2: X=Y=150 mm	1216 Hz	2651 Hz	3400 Hz
Rib2: X=Y=200 mm	-	-	-

A.3.4.5 R variation with X=Y=120 and Rib1=Rib2

Table A.30: R variation with X=Y=120 and Rib1=Rib2. The three first three modes where the ribs move in the same direction.

Dimensions	First mode	Second mode	Third mode
R=151 mm	4791 Hz	-	-
R=200 mm	4057 Hz	-	-
R=250 mm	3700 Hz	-	-
R=300 mm	3494 Hz	6538 Hz	-
R=400 mm	3268 Hz	6195 Hz	-

Table A.31: R variation with X=Y=120 and Rib1=Rib2. The three first three modes where the ribs move in the opposite direction.

Dimensions	First mode	Second mode	Third mode
R=151 mm	4123 Hz	6338 Hz	-
R=200 mm	3500 Hz	5890 Hz	-
R=250 mm	3200 Hz	5615 Hz	-
R=300 mm	3026 Hz	5437 Hz	-
R=400 mm	2832 Hz	5224 Hz	-

A.3.4.6 R variation with X=Y=120, Rib1 ≠Rib2, and Rib1 with R1=151 mm

Table A.32: R variation with X=Y=120, Rib1 ≠Rib2, and Rib1 with R1=151 mm. The first three bending modes where the ribs move in the same direction.

Dimensions	First mode	Second mode	Third mode
R2=151 mm	4791 Hz	-	-
R2=200 mm	4587 Hz	-	-
R2=250 mm	4553 Hz	-	-
R2=300 mm	4539 Hz	-	-
R2=400 mm	4528 Hz	-	-

Table A.33: R variation with X=Y=120, Rib1 ≠Rib2, and Rib1 with R1=151 mm. The first three bending modes where the ribs move in the opposite direction.

Dimensions	First mode	Second mode	Third mode
R2=151 mm	4123 Hz	6338 Hz	-
R2=200 mm	3654 Hz	6055 Hz	-
R2=250 mm	3365 Hz	5838 Hz	-
R2=300 mm	3184 Hz	5680 Hz	-
R2=400 mm	2984 Hz	5479 Hz	-

A.3.4.7 R variation with X=Y=120, Rib1 ≠Rib2, and Rib1 with R1=10 000 mm

Table A.34: R variation with X=Y=120, Rib1 ≠Rib2, and Rib1 with R1=10 000 mm. The first three bending modes where the ribs move in the same direction.

Dimensions	First mode	Second mode	Third mode
R2=151 mm	4511 Hz	-	-
R2=200 mm	3826 Hz	6725 Hz	-
R2=250 mm	3502 Hz	6367 Hz	-
R2=300 mm	3318 Hz	6146 Hz	-
R2=400 mm	3116 Hz	5898 Hz	-

Table A.35: R variation with X=Y=120, Rib1 ≠Rib2, and Rib1 with R1=10 000 mm. The first three bending modes where the ribs move in the opposite direction.

Dimensions	First mode	Second mode	Third mode
R2=151 mm	2507 Hz	4919 Hz	-
R2=200 mm	2506 Hz	4902 Hz	-
R2=250 mm	2501 Hz	4883 Hz	-
R2=300 mm	2495 Hz	4866 Hz	-
R2=400 mm	2434 Hz	4837 Hz	-

A.3.4.8 Constant area and volume between the ribs, Rib1=Rib2, by changing R

Table A.36: Constant area and volume between the ribs, Rib1=Rib2, by changing R. The first three bending modes where the ribs move in the same direction.

Dimensions	First mode	Second mode	Third mode
X=Y=150 mm and R=532 mm	2350 Hz	4489 Hz	5885 Hz
X=Y=160 mm and R=327 mm	2488 Hz	4628 Hz	5599 Hz
X=Y=165 mm and R=287.5 mm	2548 Hz	4689 Hz	6596 Hz
X=Y=170 mm and R=262.7 mm	2599 Hz	4741 Hz	6532 Hz

Table A.37: Constant area and volume between the ribs, Rib1=Rib2 and X=Y, by changing R. The first three bending modes where the ribs move in the opposite direction.

Dimensions	First mode	Second mode	Third mode
X=Y=150 mm and R=532 mm	2033 Hz	3871 Hz	5567 Hz
X=Y=160 mm and R=327 mm	2145 Hz	3957 Hz	5618 Hz
X=Y=165 mm and R=287.5 mm	2194 Hz	3999 Hz	5607 Hz
X=Y=170 mm and R=262.7 mm	2237 Hz	4035 Hz	5607 Hz

A.3.4.9 Angle, α, variation (angle between the ribs)

Table A.38: Angle, α, variation (angle between the ribs). The three first three modes where the ribs move in the same direction.

Dimensions	First mode	Second mode	Third mode
α=0° (base model)	2727 Hz	5381 Hz	6993 Hz
α=10°	2500 Hz	5133 Hz	6073 Hz
α=20°	2243 Hz	4723 Hz	-
α=30°	2753 Hz	-	-
α=40°	2730 Hz	-	-
α=50°	2686 Hz	-	-

Table A.39: Angle, α, variation (angle between the ribs). The first three bending modes where the ribs move in the opposite direction.

Dimensions	First mode	Second mode	Third mode
α=0° (base model)	2378 Hz	4670 Hz	6779 Hz
α=10°	2319 Hz	4342 Hz	5869 Hz
α=20°	2285 Hz	3839 Hz	4877 Hz
α=30°	2263 Hz	-	-
α=40°	2249 Hz	-	-
α=50°	2243 Hz	-	-

A.3.4.10 Distance between the ribs, d, variation with Rib1=Rib2 and X=Y=120 mm

Table A.40: Distance between the ribs, d, variation with Rib1=Rib2 and X=Y=120 mm. The first three bending modes where the ribs move in the same direction.

Dimensions	First mode	Second mode	Third mode
d=40 mm (base model)	2727 Hz	5381 Hz	6993 Hz
d=20 mm	2951 Hz	4126 Hz	6965 Hz
d=25 mm	2908 Hz	3877 Hz	7001 Hz
d=30 mm	2845 Hz	3601 Hz	7012 Hz
d=35 mm	2782 Hz	3347 Hz	7007 Hz
d=50 mm	2638 Hz	5121 Hz	6944 Hz
d=60 mm	2571 Hz	4963 Hz	6867 Hz
d=100 mm	2409 Hz	4538 Hz	5621 Hz

Table A.41: Distance between the ribs, d, variation with Rib1=Rib2 and X=Y=120 mm. The first three bending modes where the ribs move in the opposite direction.

Dimensions	First mode	Second mode	Third mode
d=40 mm (base model)	2378 Hz	4670 Hz	6779 Hz
d=20 mm	2598 Hz	5020 Hz	7214 Hz
d=25 mm	2508 Hz	4896 Hz	7115 Hz
d=30 mm	2451 Hz	4807 Hz	7032 Hz
d=35 mm	2410 Hz	4735 Hz	6933 Hz
d=50 mm	2328 Hz	4539 Hz	6217 Hz
d=60 mm	2283 Hz	4380 Hz	5082 Hz
d=100 mm	2009 Hz	5091 Hz	7084 Hz

A.3.4.11 Distance between the ribs, d, variation with Rib1=Rib2 and X=Y=150 mm

Table A.42: Distance between the ribs, d, variation with Rib1=Rib2 and X=Y=150 mm. The first three bending modes where the ribs move in the same direction.

Dimensions	First mode	Second mode	Third mode
d=20	2159 Hz	3256 Hz	5564 Hz
d=40 mm	1987 Hz	3943 Hz	5512 Hz
d=50 mm	1917 Hz	3709 Hz	5448 Hz
d=60 mm	1867 Hz	3597 Hz	5386 Hz
d=100 mm	1753 Hz	3401 Hz	4907 Hz

Table A.43: Distance between the ribs, d, variation with Rib1=Rib2 and X=Y=150 mm. The first three bending modes where the ribs move in the opposite direction.

Dimensions	First mode	Second mode	Third mode
d=20	1890 Hz	3630 Hz	5475 Hz
d=40 mm	1724 Hz	3428 Hz	5159 Hz
d=50 mm	1692 Hz	3375 Hz	4984 Hz
d=60 mm	1668 Hz	3323 Hz	-
d=100 mm	1557 Hz	3852 Hz	5488 Hz

A.3.4.12 Constant volume between the ribs (288 000 mm^3), Rib1=Rib2 and X=Y, by changing the distance, d, between the ribs

Table A.44: Constant volume between the ribs (288 000 mm^3), Rib1=Rib2 and X=Y, by changing the distance, d, between the ribs. The first three bending modes where the ribs move in the same direction.

Dimensions	First mode	Second mode	Third mode
X=Y=90 mm and d=81.63 mm	3746 Hz	-	-
X=Y=100 mm and d=65.23 mm	3316 Hz	6244 Hz	-
X=Y=130 mm and d=37.56 mm	2456 Hz	4894 Hz	-
X=Y=140 mm and d=32.19 mm	2265 Hz	4725 Hz	6071 Hz
X=Y=150 mm and d=27.89 mm	2101 Hz	3091 Hz	5578 Hz

Table A.45: Constant volume between the ribs (288 000 mm^3), Rib1=Rib2 and X=Y, by changing the distance, d, between the ribs. The first three bending modes where the ribs move in the opposite direction.

Dimensions	First mode	Second mode	Third mode
X=Y=90 mm and d=81.63 mm	3004 Hz	-	-
X=Y=100 mm and d=65.23 mm	3304 Hz	4983 Hz	-
X=Y=130 mm and d=37.56 mm	2130 Hz	4211 Hz	-
X=Y=140 mm and d=32.19 mm	1944 Hz	3840 Hz	5797 Hz
X=Y=150 mm and d=27.89 mm	1792 Hz	3517 Hz	5328 Hz

A.4 Complementary result plots

A.4.1 Model 1 single rib

A.4.1.1 Area variation

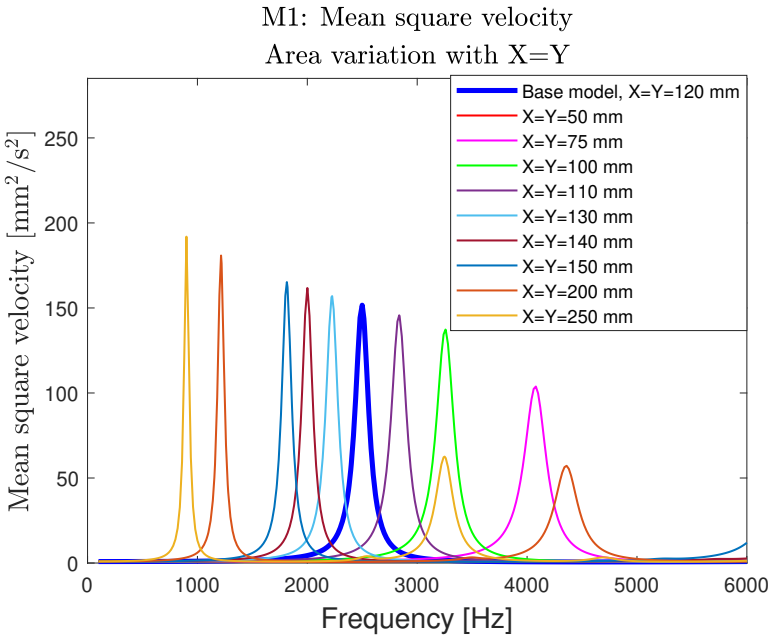

Figure A.8: Mean square velocity of M1 single with different areas.

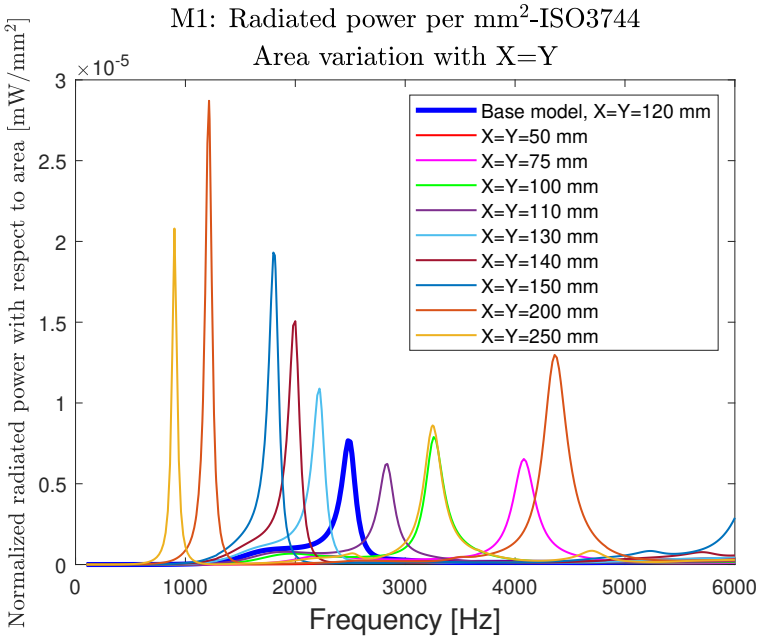

Figure A.9: Radiated power normalized by the area of the rib structure for M1 single with different areas.

A.4.1.2 Constant area

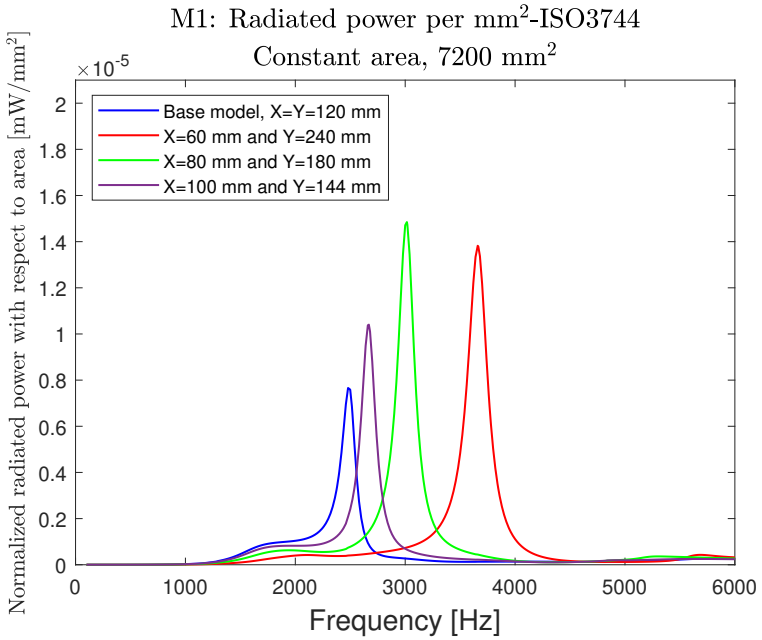

Figure A.10: Radiated power normalized by the area of the rib structure for M1 single with the constant area of 7200 mm^2.

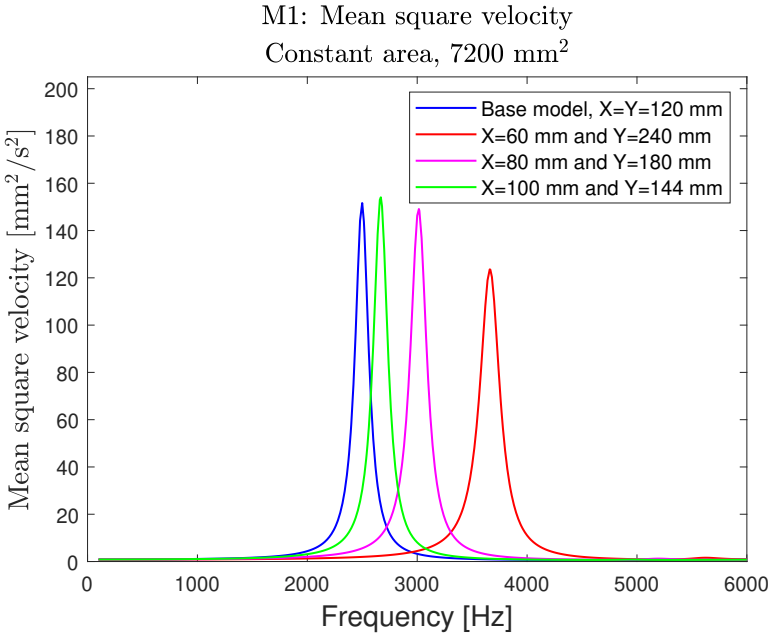

Figure A.11: Mean square velocity of M1 single with the constant area of 7200 mm^2.

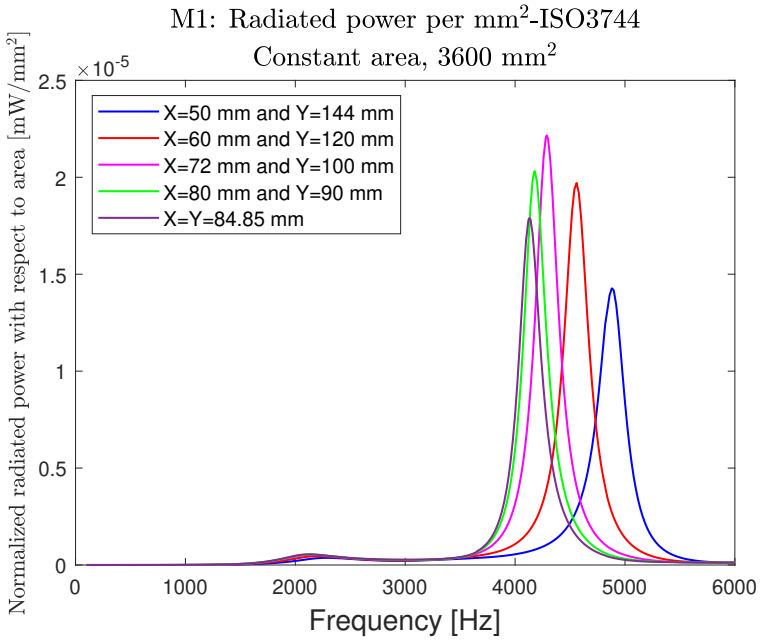

Figure A.12: Radiated power normalized by the area of the rib structure for M1 single with the constant area of 3600 mm^2.

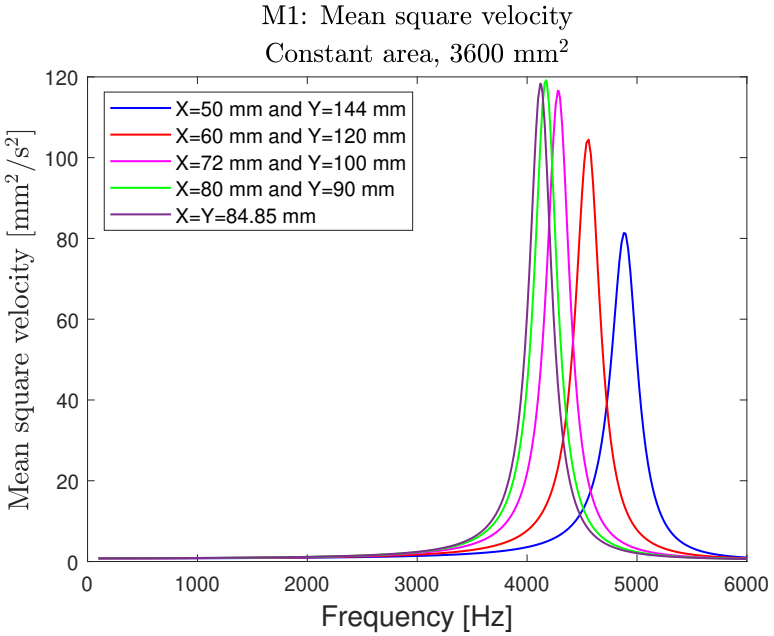

Figure A.13: Mean square velocity of M1 single with the constant area of 3600 mm^2.

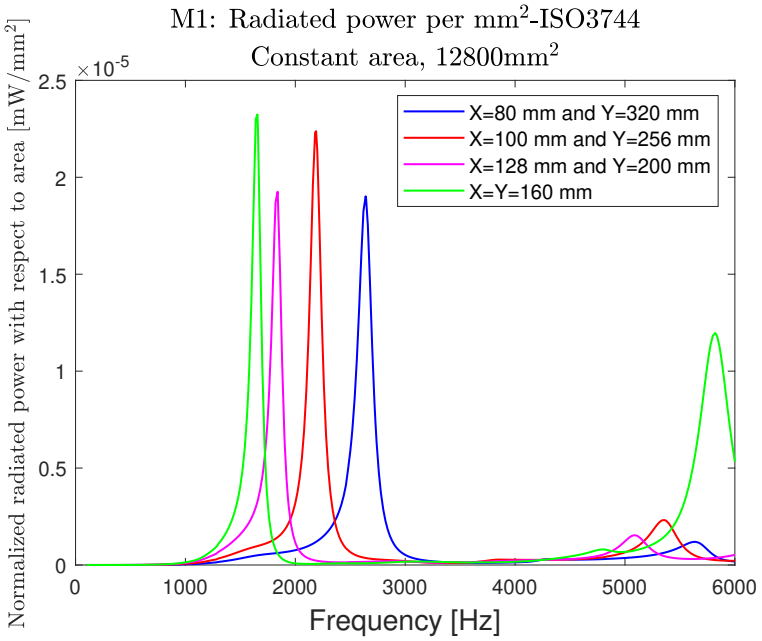

Figure A.14: Radiated power normalized by the area of the rib structure for M1 single with the constant area of 12 800 mm^2.

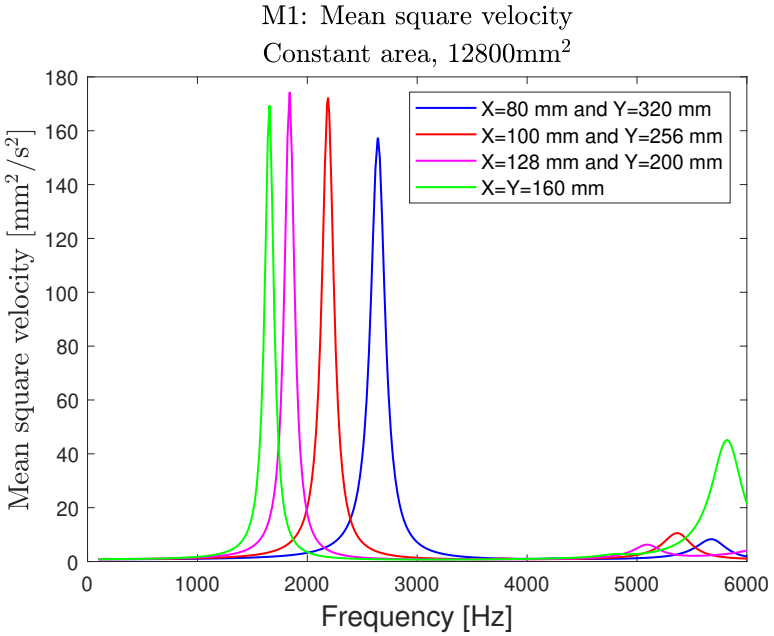

Figure A.15: Mean square velocity of M1 single with the constant area of 12 800 mm^2.

A.4.1.3 R variation

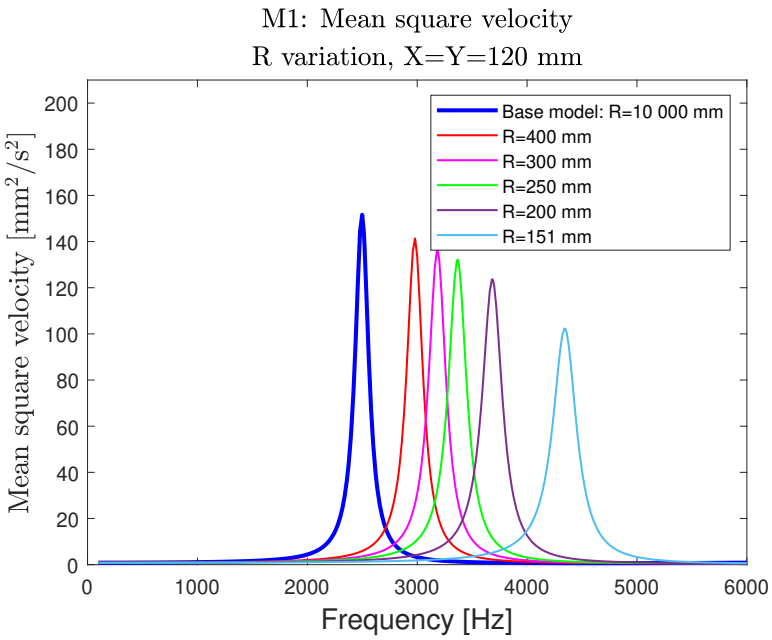

Figure A.16: Mean square velocity of M1 single with different R.

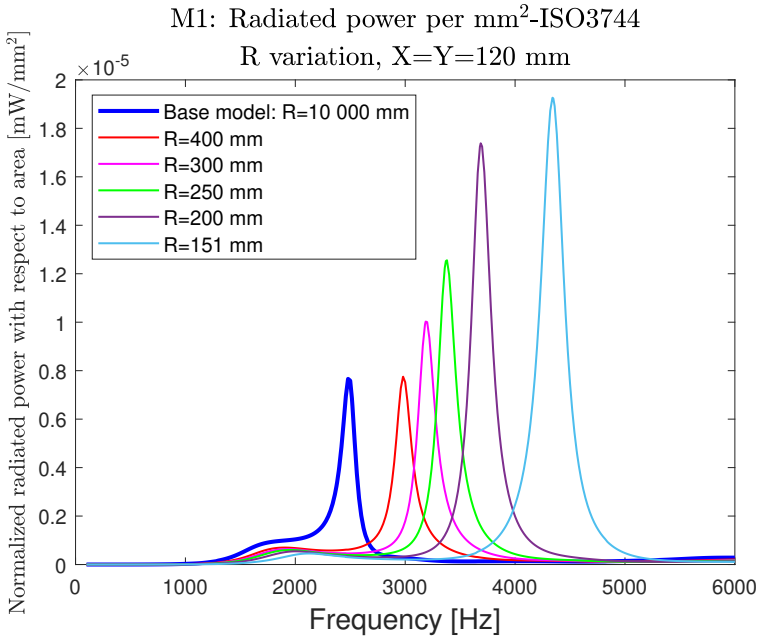

Figure A.17: Radiated power normalized by the area of the rib structure for M1 single with different R.

A.4.1.4 Constant area different R

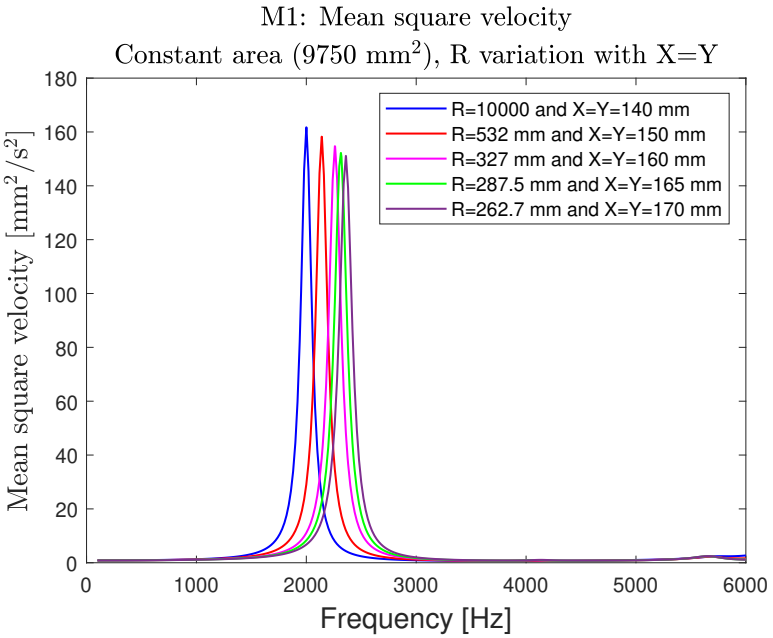

Figure A.18: Mean square velocity of M1 single with constant area and different R.

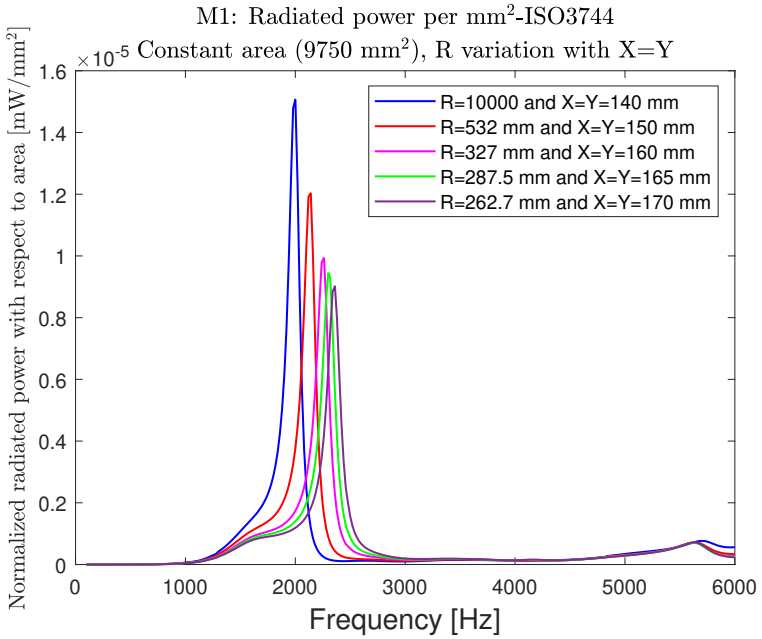

Figure A.19: Radiated power normalized by the area of the rib structure for M1 single with constant area and different R.

A.4.1.5 Constant area, 7200 mm^2, with no draft angle

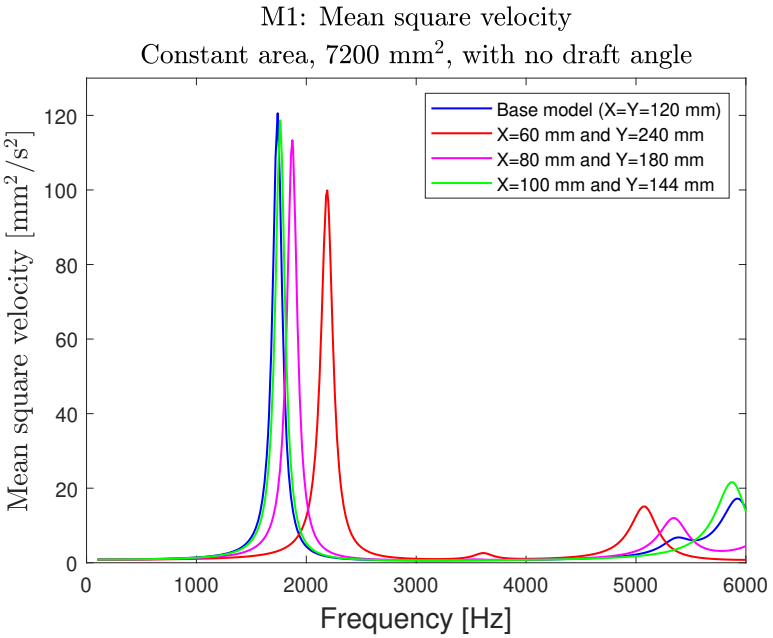

Figure A.20: Mean square velocity of M1 single with constant area and no draft angle.

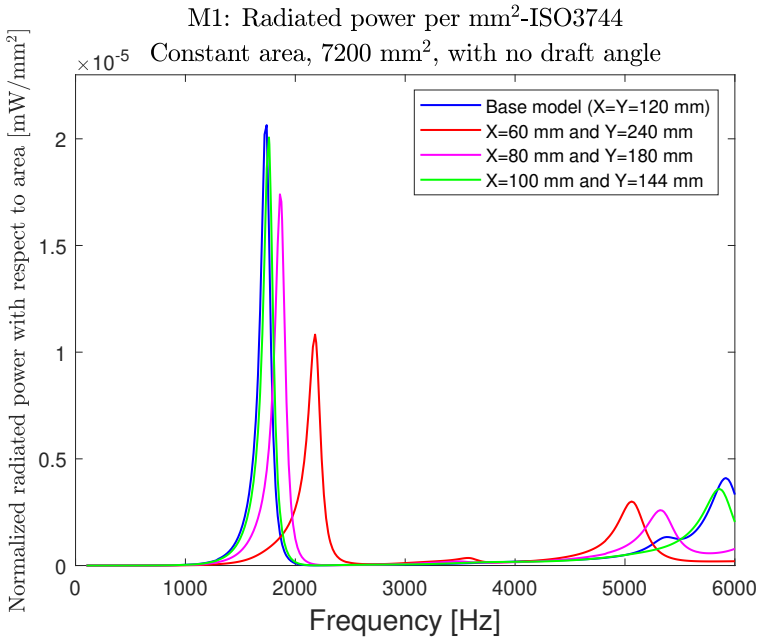

Figure A.21: Radiated power normalized by the area of the rib structure for M1 single with constant area and no draft angle.

A.4.2 Thickness variation of rib with no draft angle

A.4.2.1 X=Y=100 mm

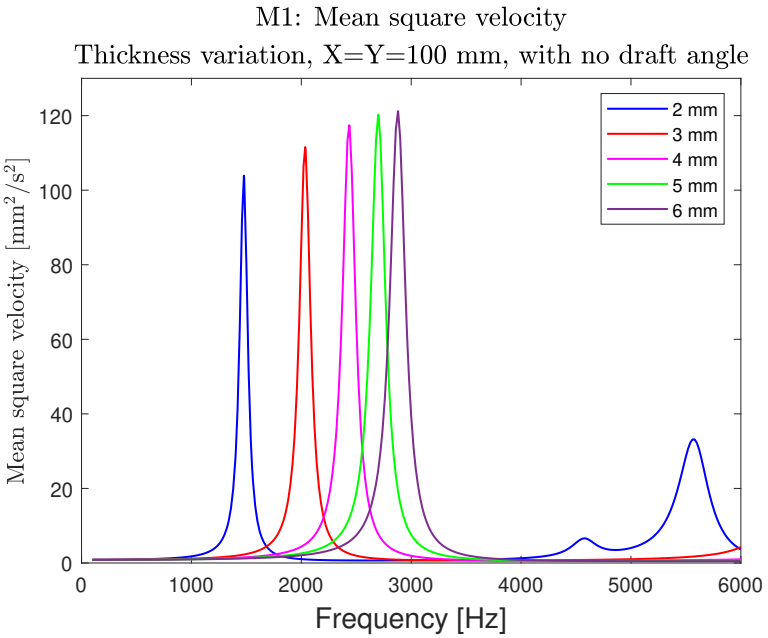

Figure A.22: Mean square velocity of M1 single with different thickness of rib and no draft angle, X=Y=100 mm.

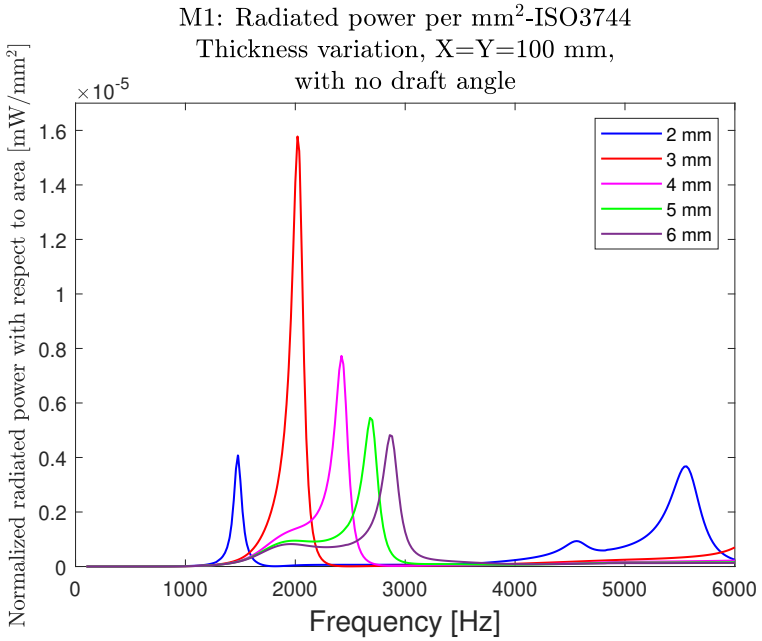

Figure A.23: Radiated power normalized by the area of the rib structure for M1 single with different thickness of rib and no draft angle, X=Y=100 mm.

A.4.2.2 X=Y=120 mm

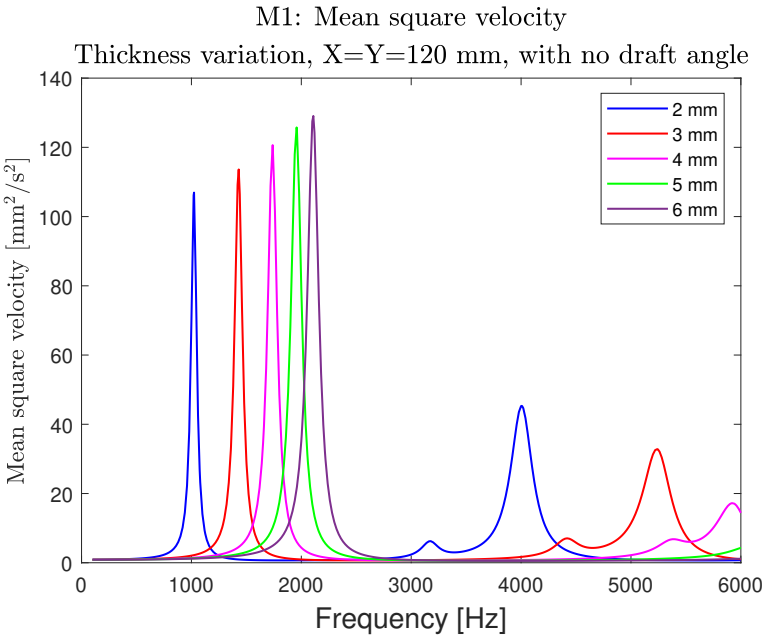

Figure A.24: Mean square velocity of M1 single with different thickness of rib and no draft angle, X=Y=120 mm.

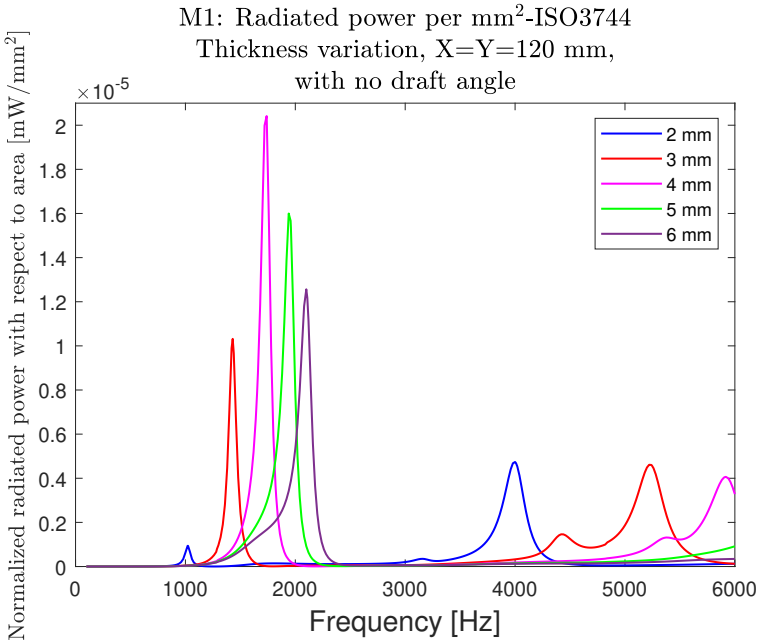

Figure A.25: Radiated power normalized by the area of the rib structure for M1 single with different thickness of rib and no draft angle, X=Y=120 mm.

A.4.2.3 X=Y=130 mm

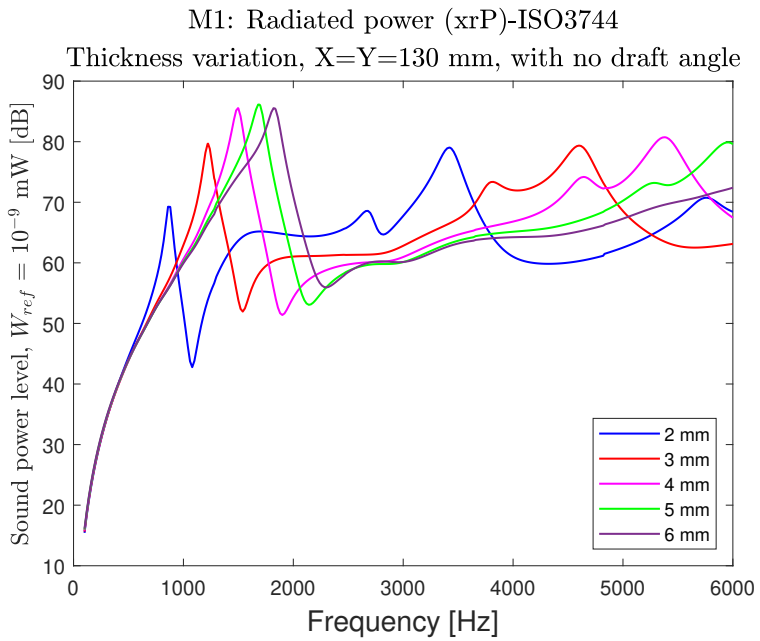

Figure A.26: Radiated power for M1 single with X=Y=130 mm with varying thickness and no draft angle.

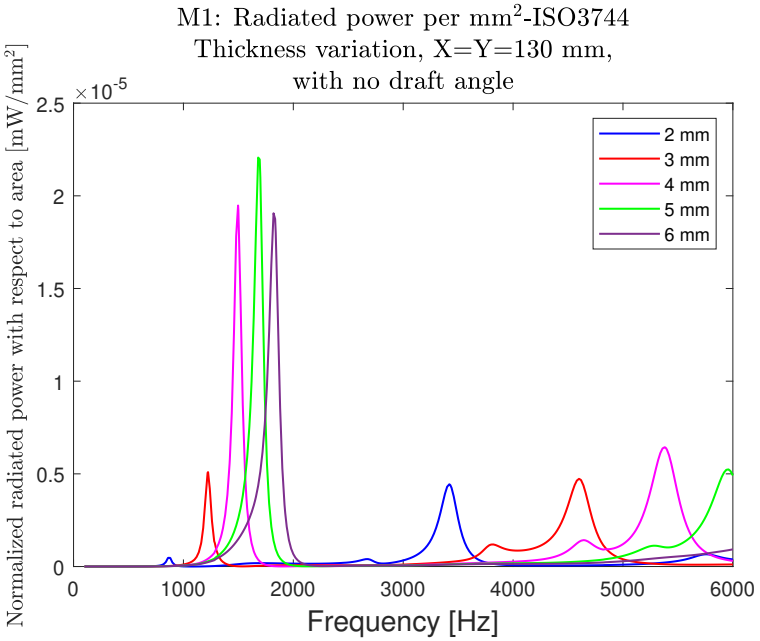

Figure A.27: Radiated power normalized by the area of the rib structure for M1 single with different thickness of rib and no draft angle, X=Y=130 mm.

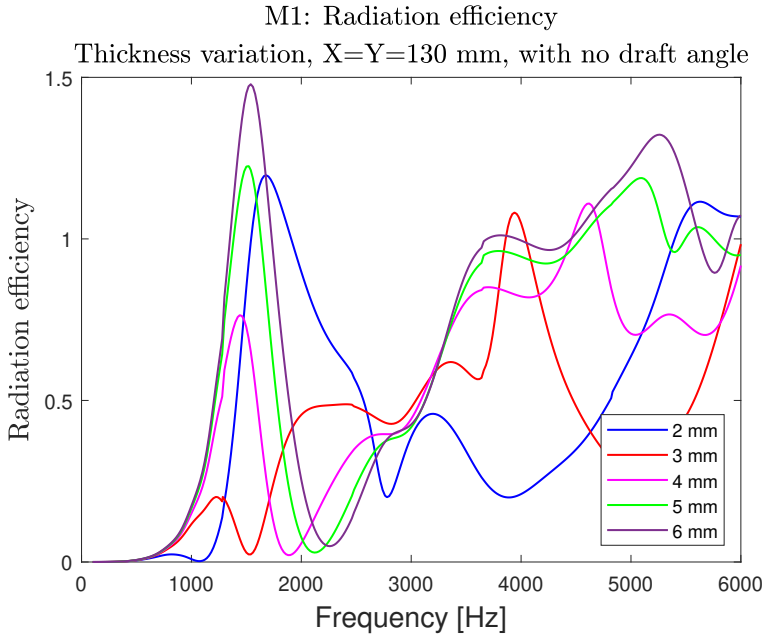

Figure A.28: Radiation efficiency for M1 single with X=Y=130 mm with varying thickness and no draft angle.

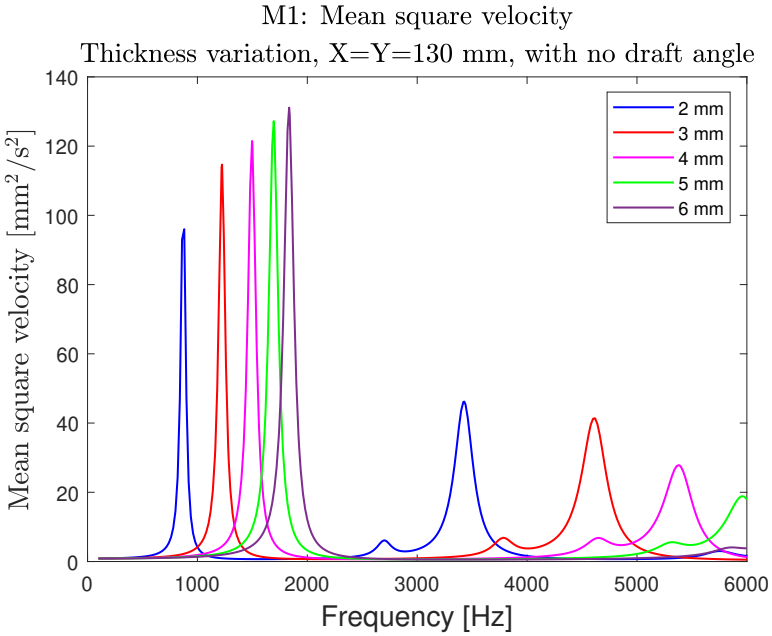

Figure A.29: Mean square velocity of M1 single with different thickness of rib and no draft angle, X=Y=130 mm.

A.4.2.4 X=Y=140 mm

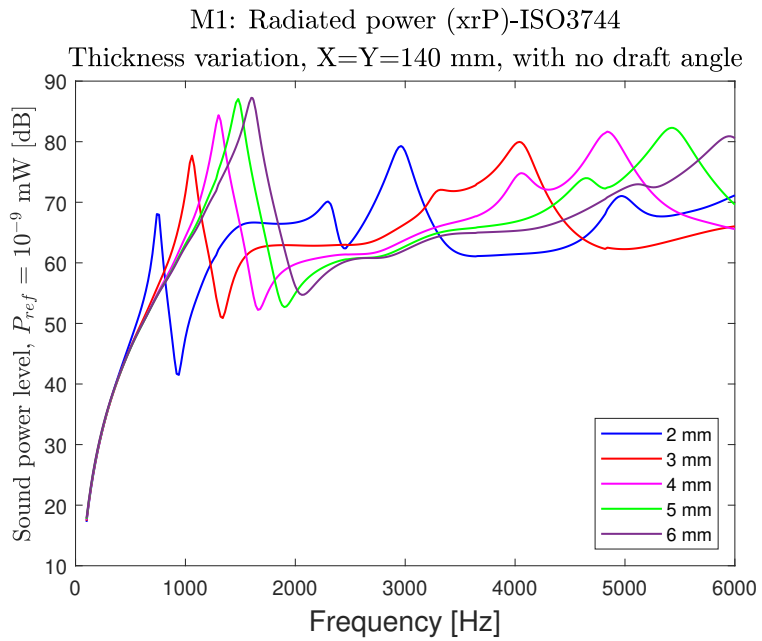

Figure A.30: Radiated power for M1 single with X=Y=140 mm with varying thickness and no draft angle.

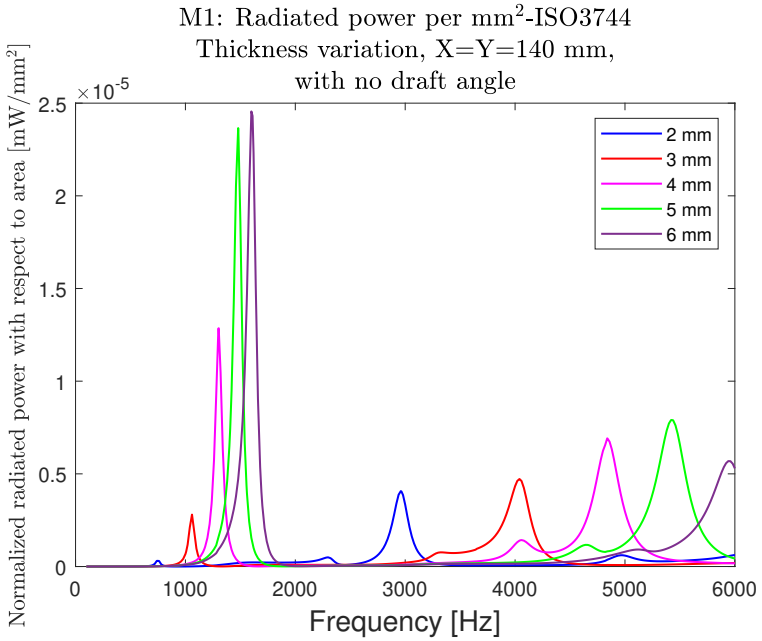

Figure A.31: Radiated power normalized by the area of the rib structure for M1 single with different thickness of rib and no draft angle, X=Y=140 mm.

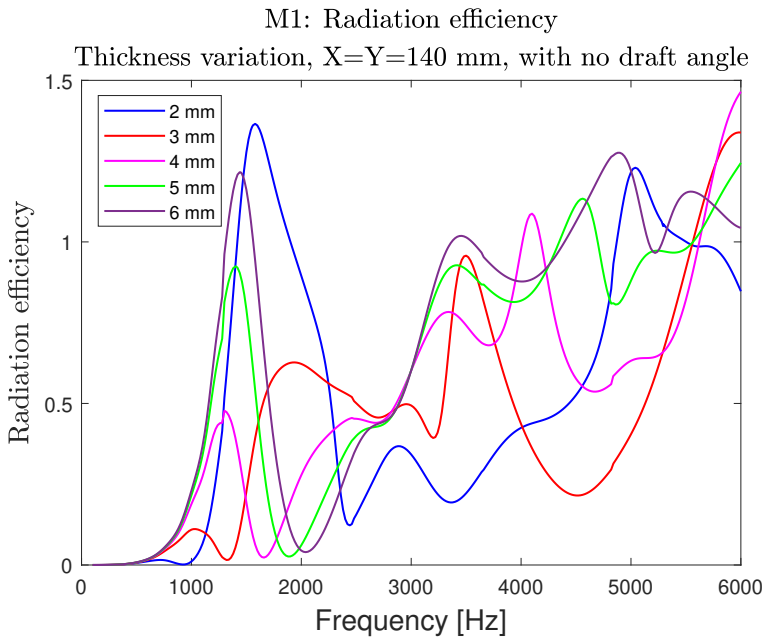

Figure A.32: Radiation efficiency for M1 single with X=Y=140 mm with varying thickness and no draft angle.

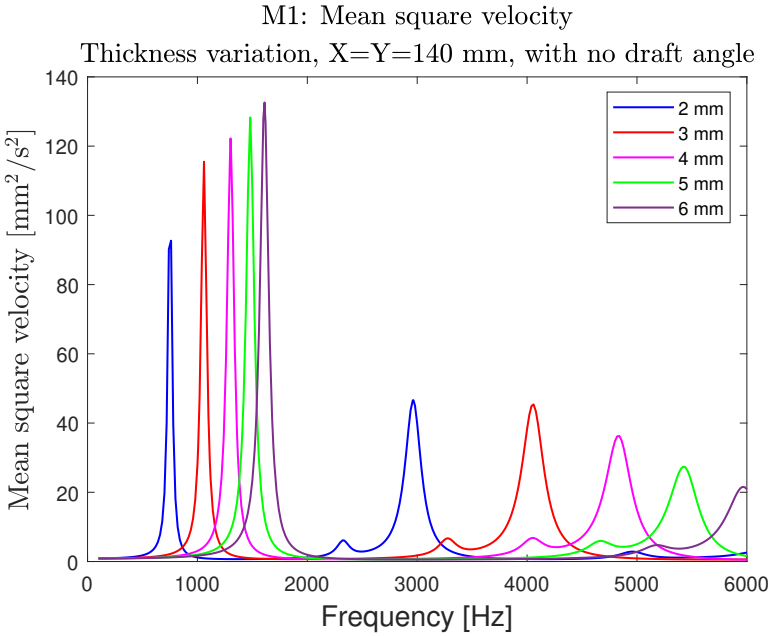

Figure A.33: Mean square velocity of M1 single with different thickness of rib and no draft angle, X=Y=140 mm.

A.4.2.5 X=Y=150 mm

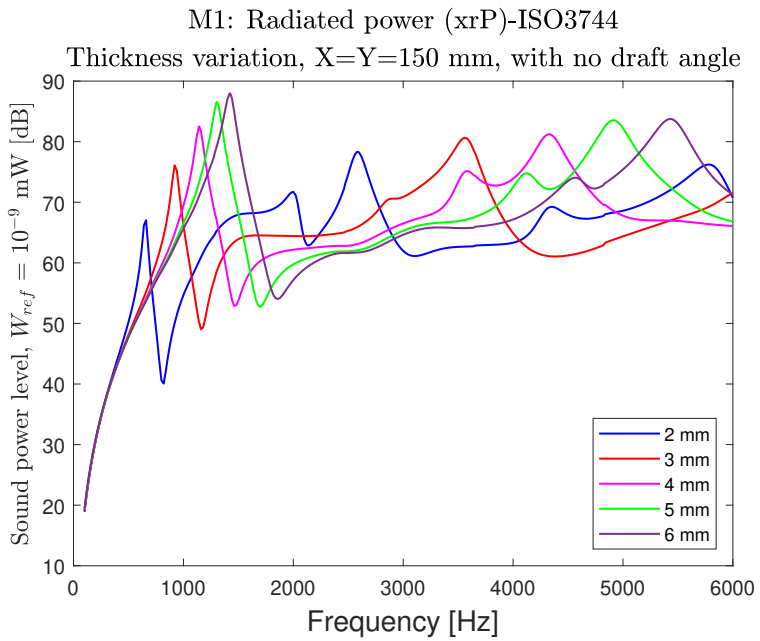

Figure A.34: Radiated power for M1 single with X=Y=150 mm with varying thickness and no draft angle.

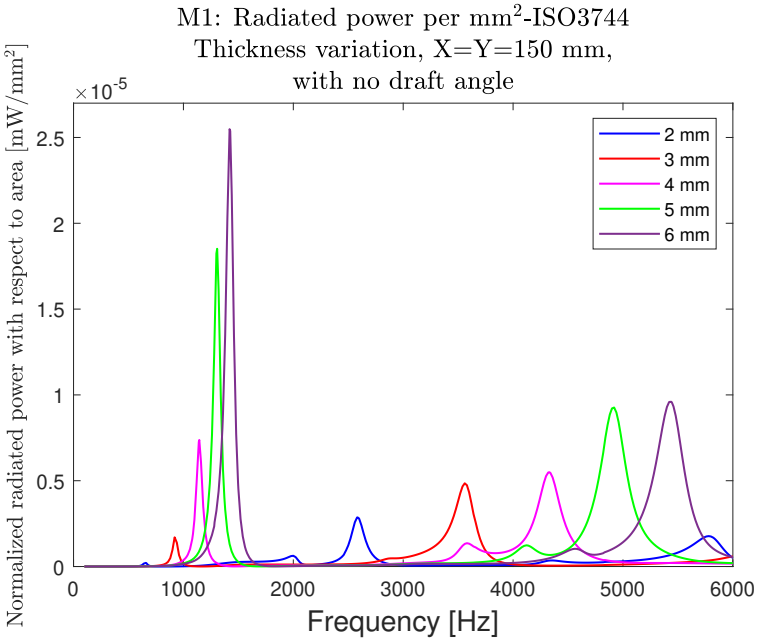

Figure A.35: Radiated power normalized by the area of the rib structure for M1 single with different thickness of rib and no draft angle, X=Y=150 mm.

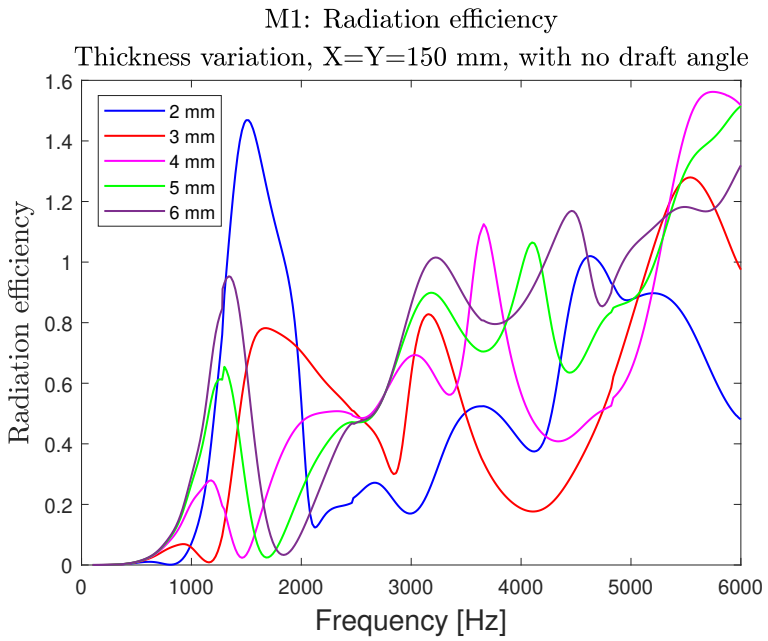

Figure A.36: Radiation efficiency for M1 single with X=Y=150 mm with varying thickness and no draft angle.

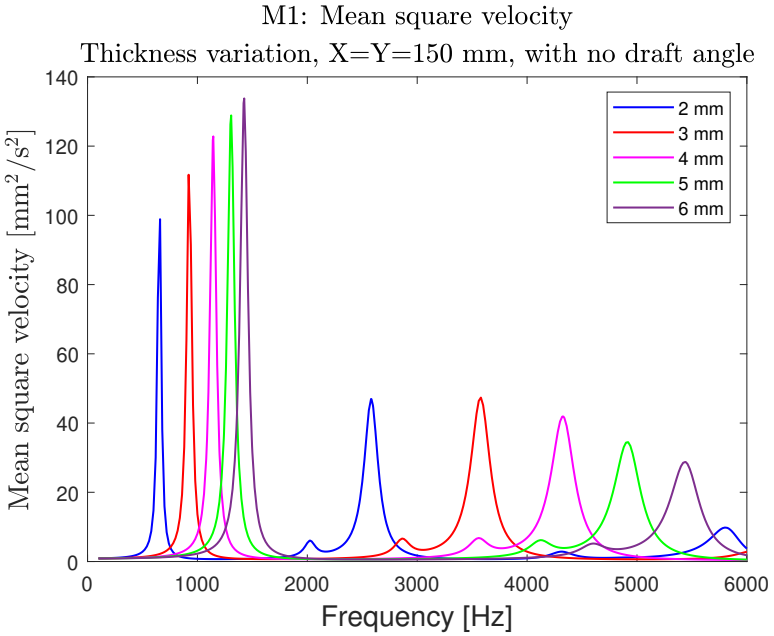

Figure A.37: Mean square velocity of M1 single with different thickness of rib and no draft angle, X=Y=150 mm.

A.4.3 Model 1 corner- single rib

A.4.3.1 α_1 variation

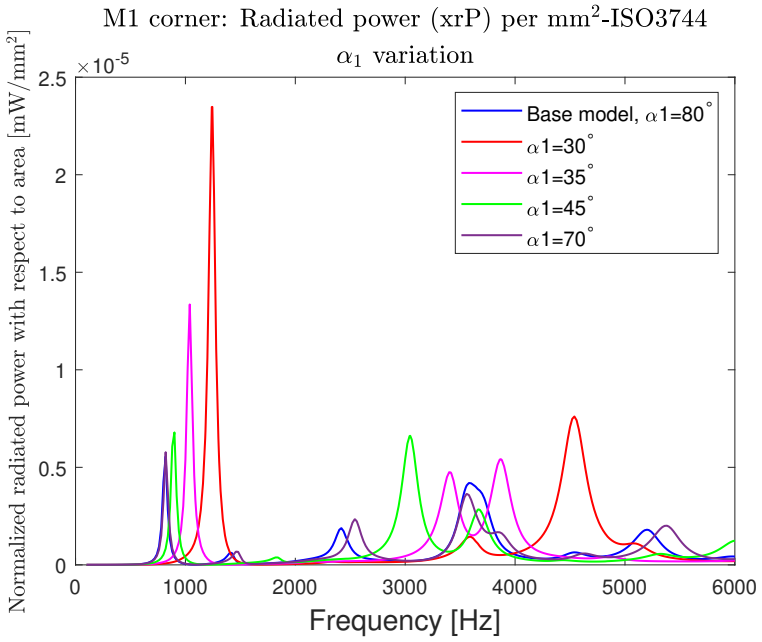

Figure A.38: Radiated power per mm^2 of M1 corner single for α_1 variation.

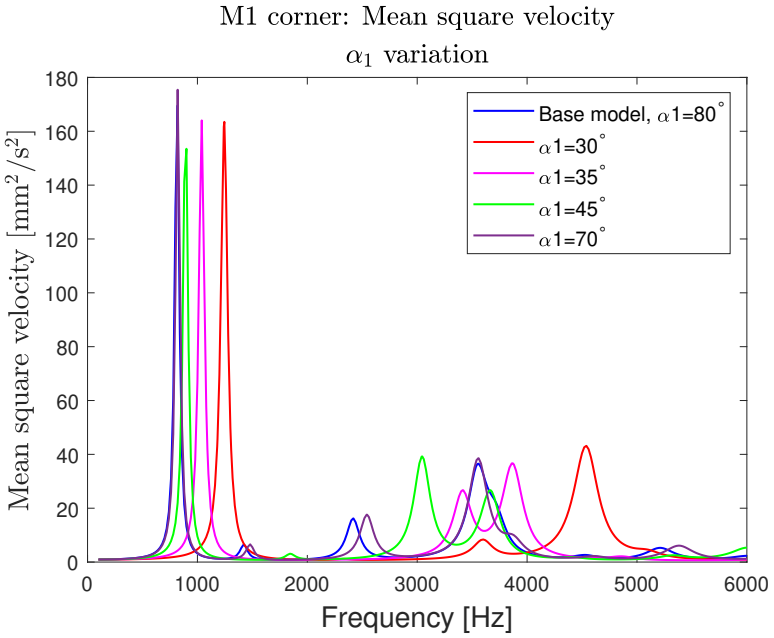

Figure A.39: Mean square velocity of M1 corner single for α_1 variation.

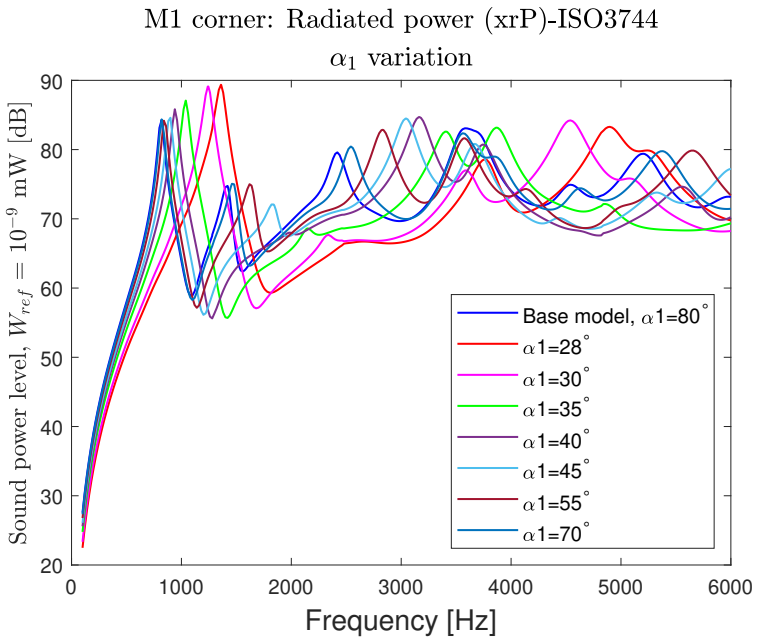

Figure A.40: Radiated power of M1 corner single for α_1 variation.

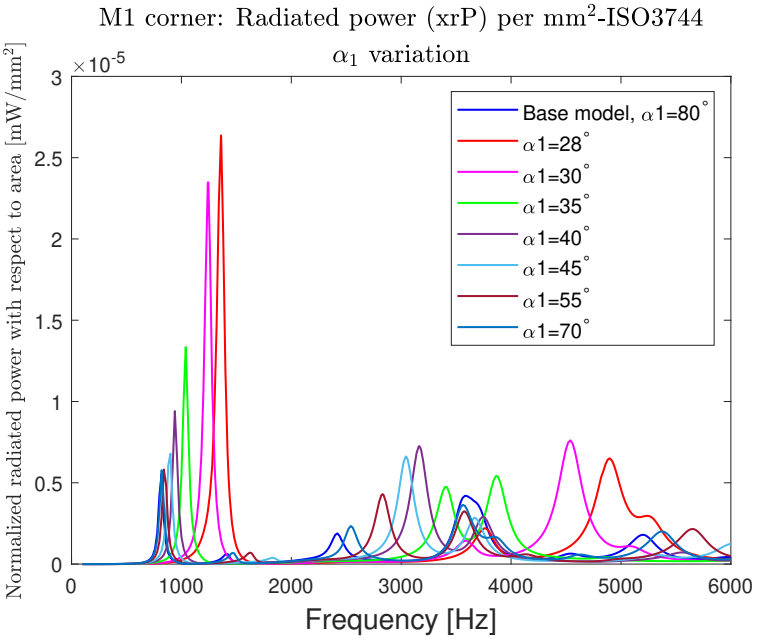

Figure A.41: Radiated power per mm^2 of M1 corner single for α_1 variation.

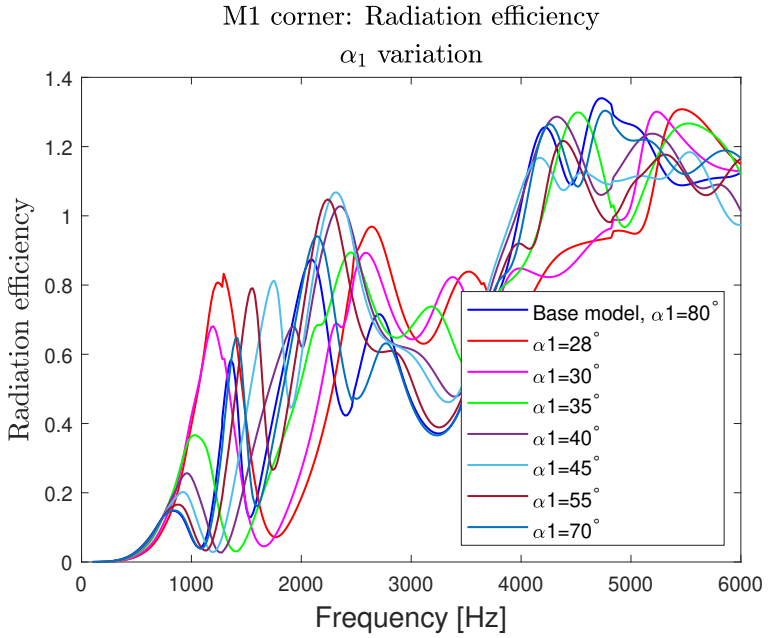

Figure A.42: Radiation efficiency of M1 corner single for α_1 variation.

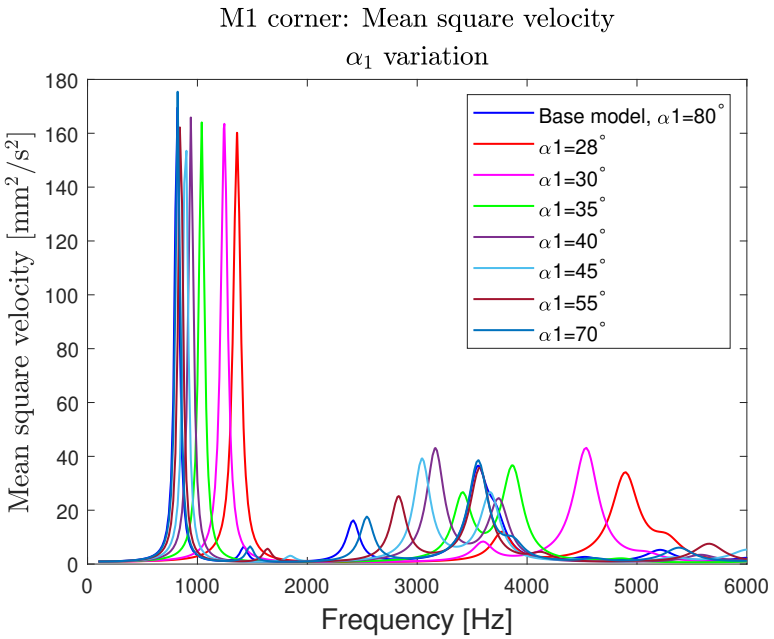

Figure A.43: Mean square velocity of M1 corner single for α_1 variation.

A.4.3.2 α_2 variation

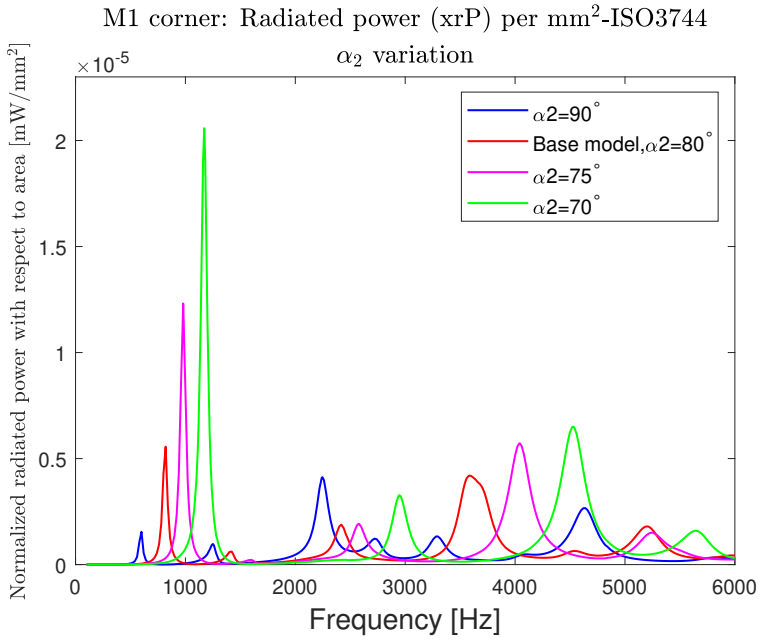

Figure A.44: Radiated power per mm^2 of M1 corner single for α_2 variation.

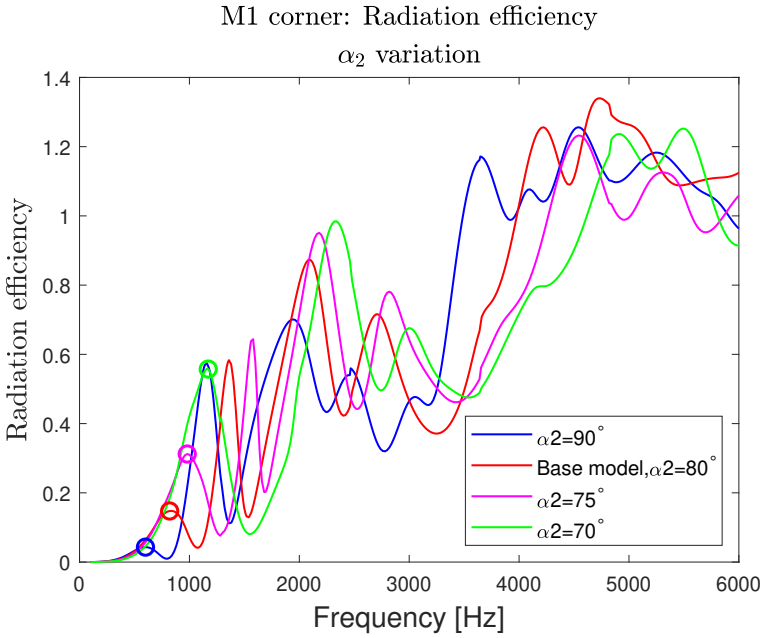

Figure A.45: Radiation efficiency of M1 corner single for α_2 variation.

A.4.3.3 R variation

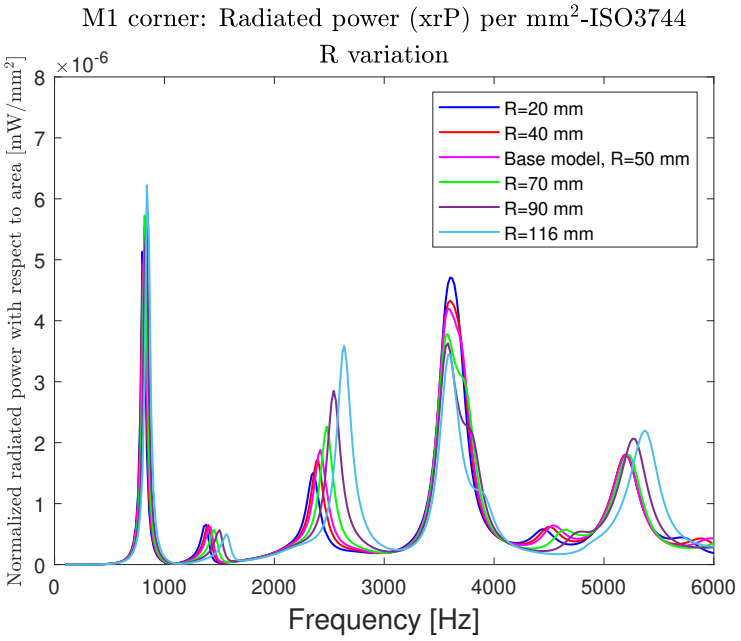

Figure A.46: Radiated power per mm^2 of M1 corner single for R variation.

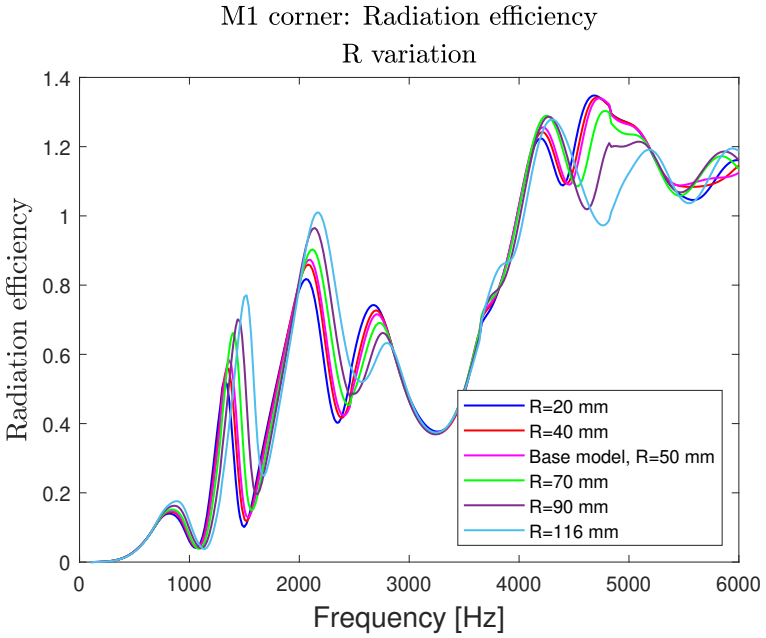

Figure A.47: Radiation efficiency of M1 corner single for R variation.

A.4.4 Model 2- single rib

A.4.4.1 Area variation

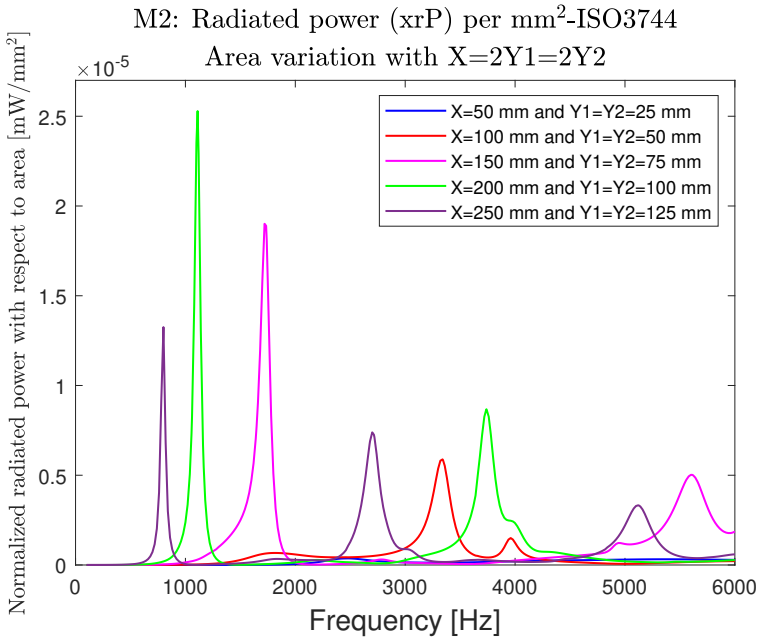

Figure A.48: Radiated power per mm^2 of M2 single for area variation with X=2Y1=2Y2.

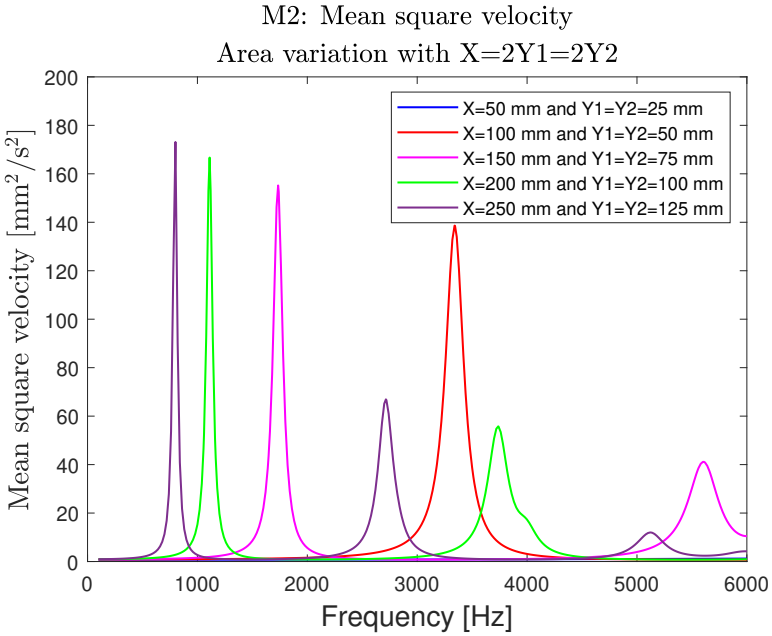

Figure A.49: Mean square velocity of M2 single for area variation with X=2Y1=2Y2.

A.4.4.2 Constant area

7200 mm^2

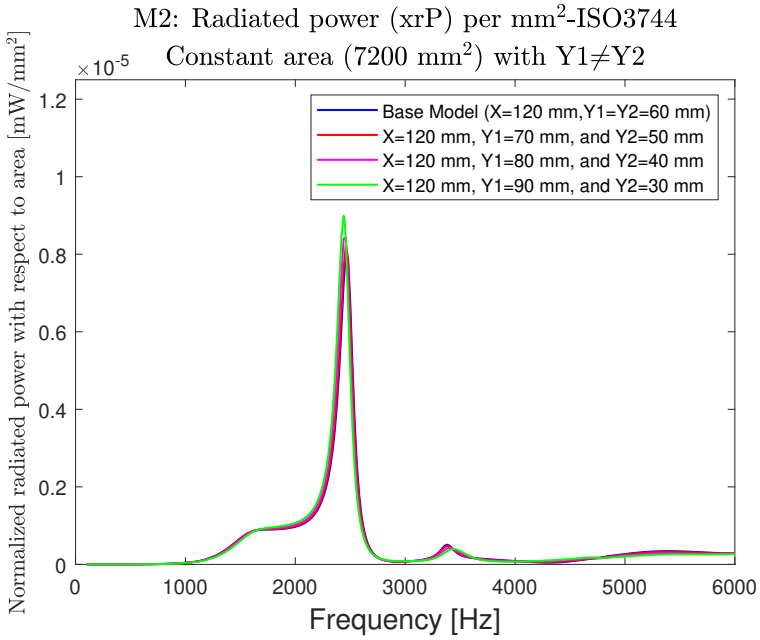

Figure A.50: Radiated power per mm^2 of M2 single for constant area, 7200 mm^2.

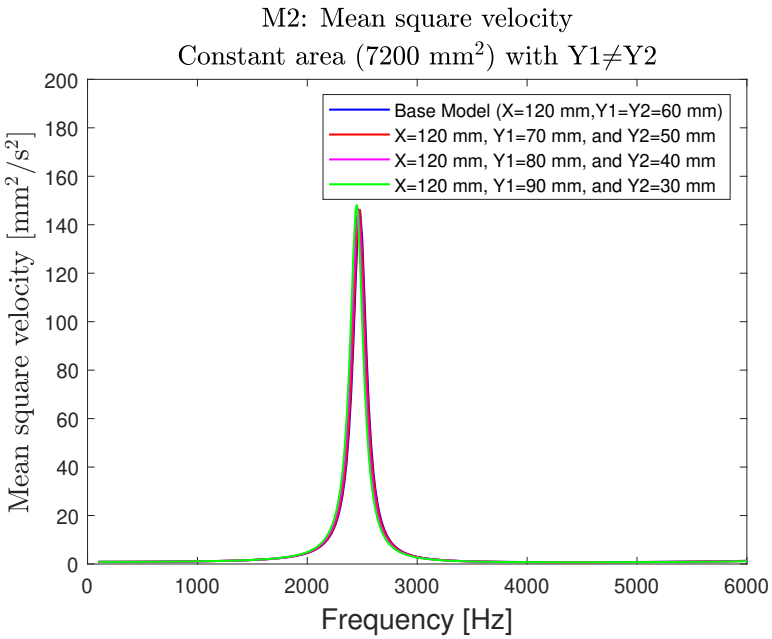

Figure A.51: Mean square velocity of M2 single for constant area, 7200 mm^2.

12800 mm^2

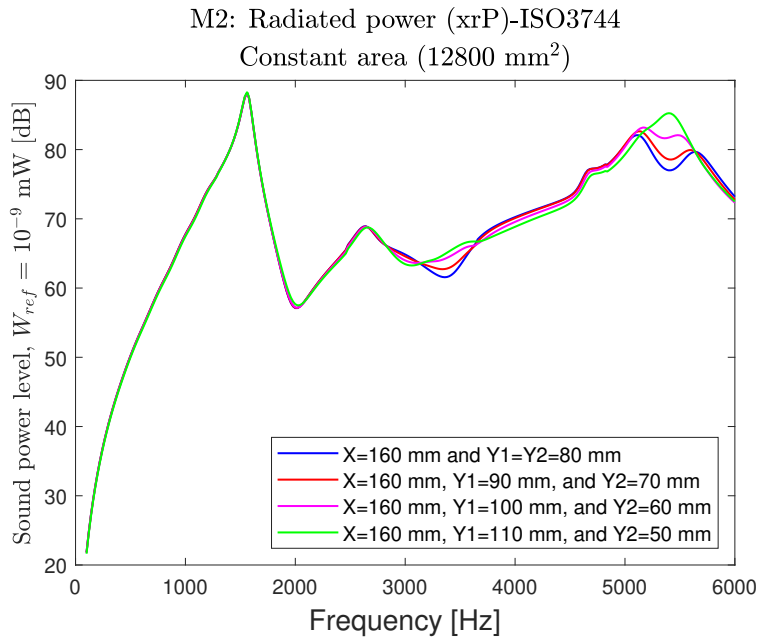

Figure A.52: Radiated power of M2 single for constant area, 12800 mm^2.

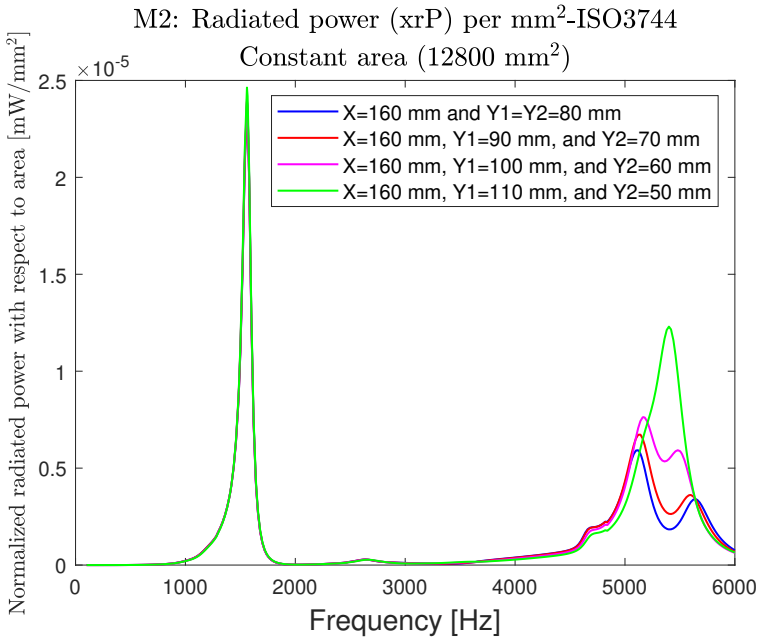

Figure A.53: Radiated power per mm^2 of M2 single for constant area, 12800 mm^2.

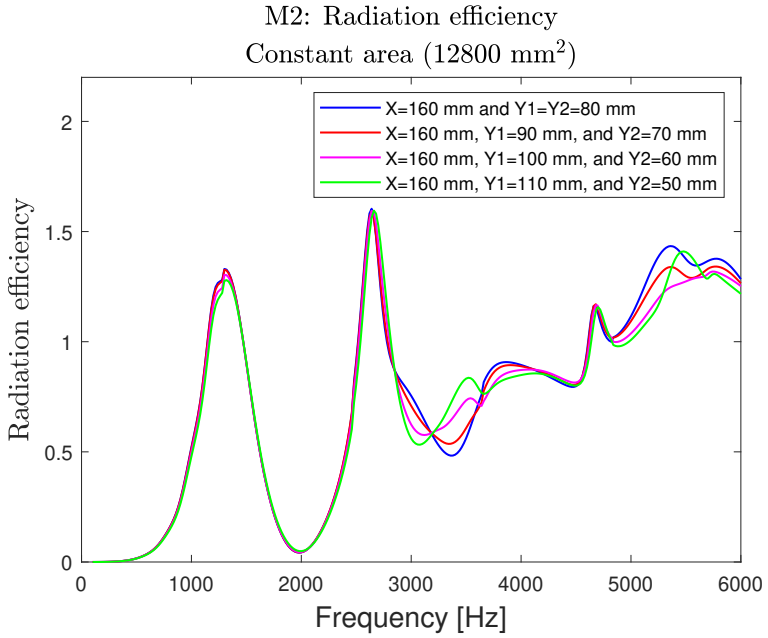

Figure A.54: Radiation efficiency of M2 single for constant area, 12800 mm^2.

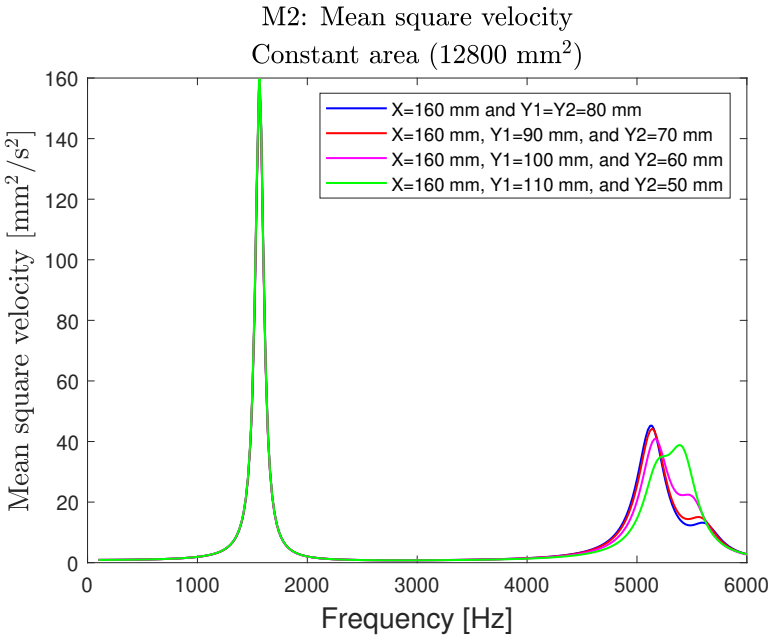

Figure A.55: Mean square velocity of M2 single for constant area, 12800 mm^2.

3600 mm^2

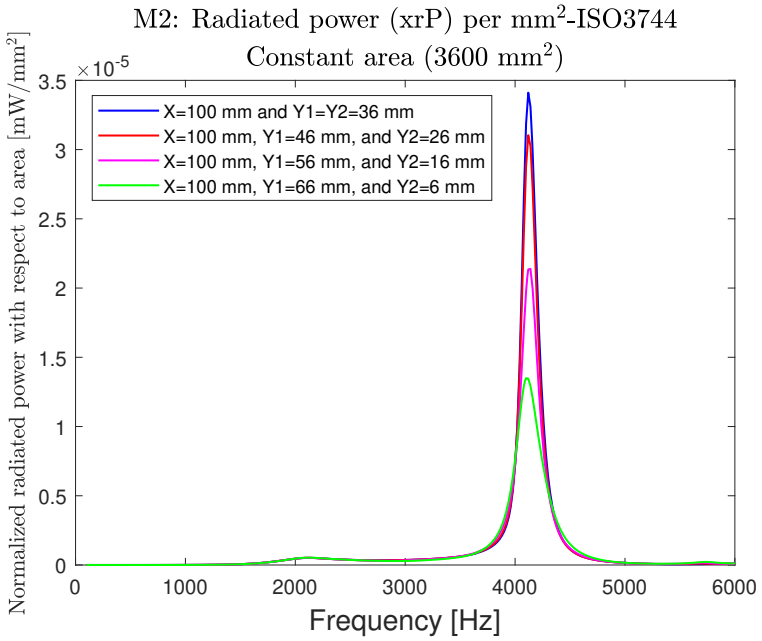

Figure A.56: Radiated power per mm^2 of M2 single for constant area, 3600 mm^2.

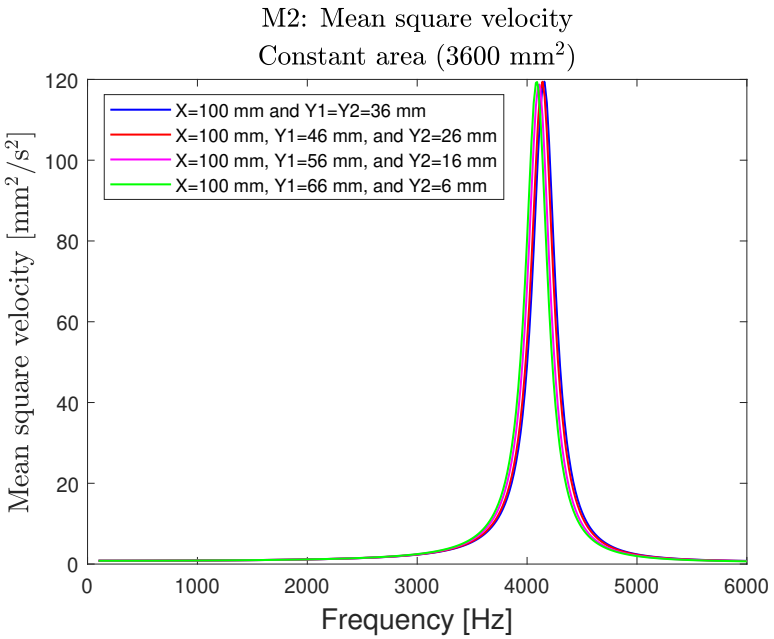

Figure A.57: Mean square velocity of M2 single for constant area, 3600 mm^2.

A.4.4.3 R variation

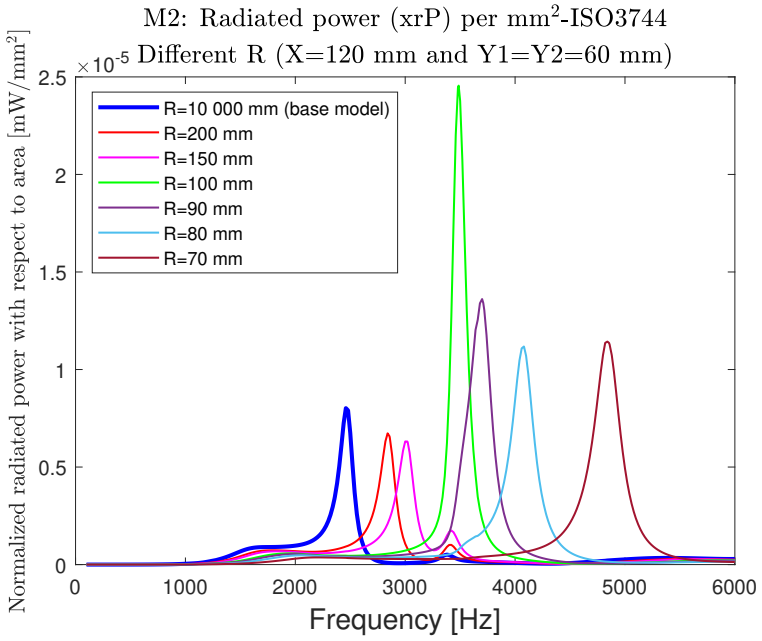

Figure A.58: Radiated power per mm^2 for M2 single of R variation.

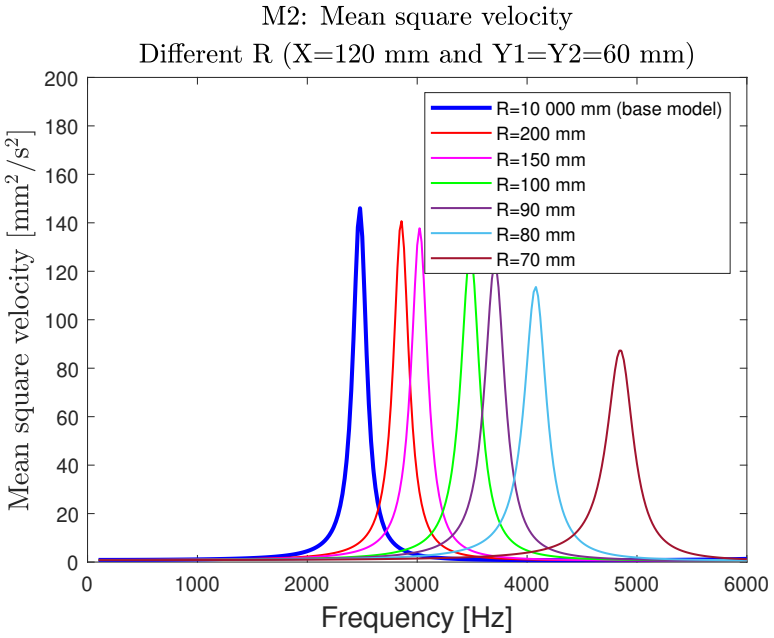

Figure A.59: Mean square velocity for M2 single of R variation.

A.4.5 M1- double rib

A.4.5.1 Area variation

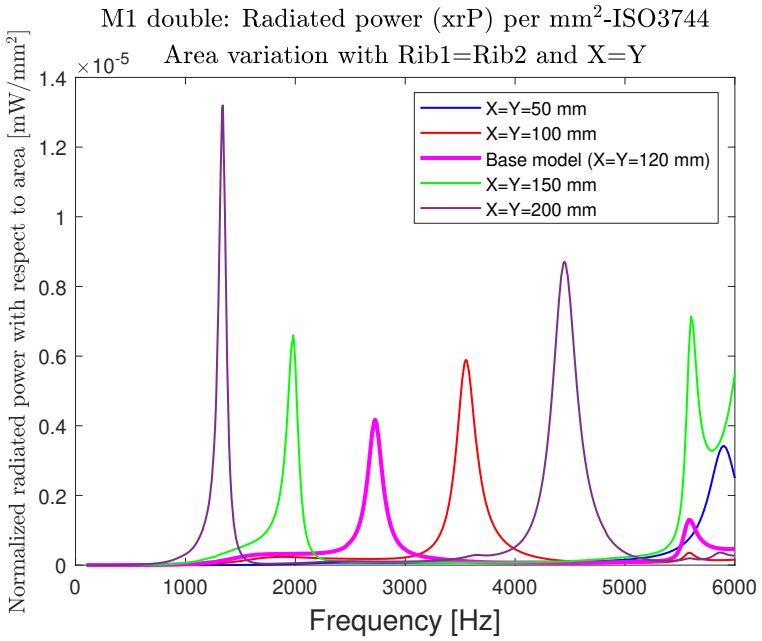

Figure A.60: Radiated power per mm^2 for M1 double of area variation.

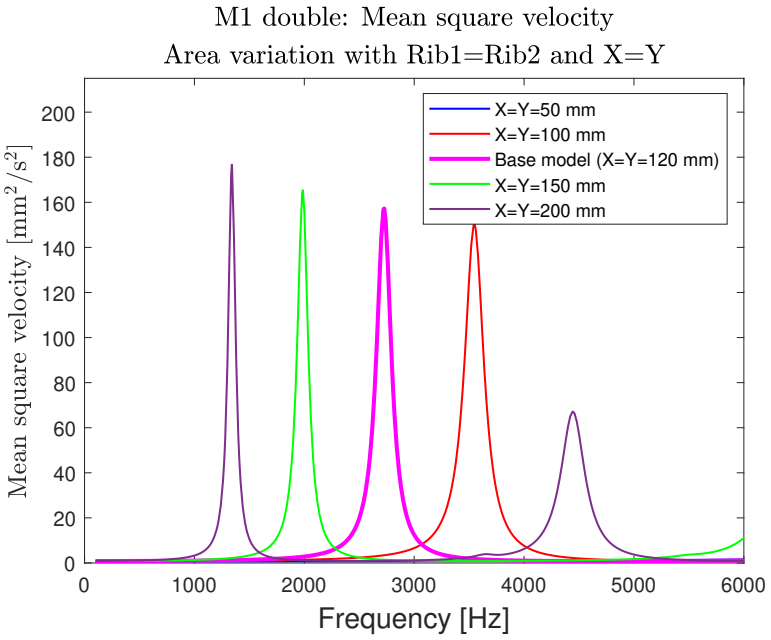

Figure A.61: Mean square velocity for M1 double of area variation.

A.4.5.2 Area variation with Rib1≠Rib2

Rib1: X=Y=120 mm

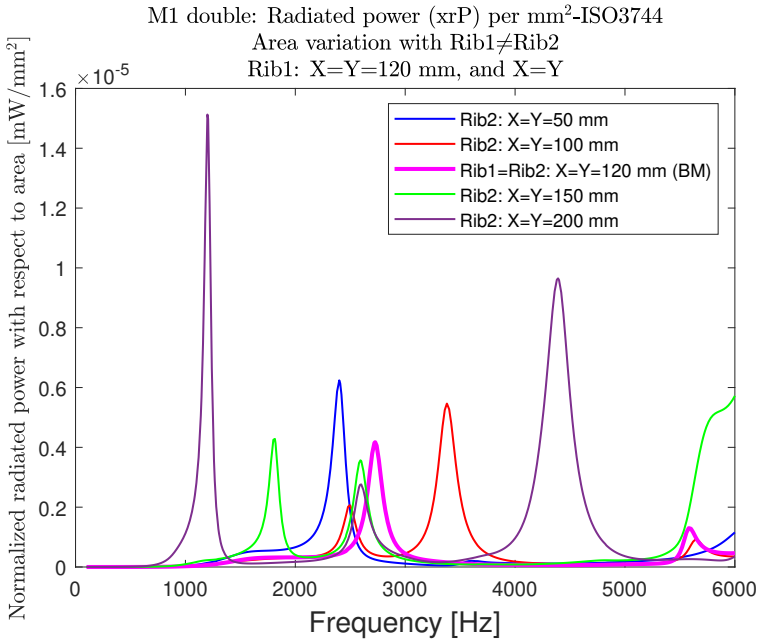

Figure A.62: Radiated power per mm^2 for M1 double of area variation with Rib1≠Rib2 and Rib1: X=Y=120 mm.

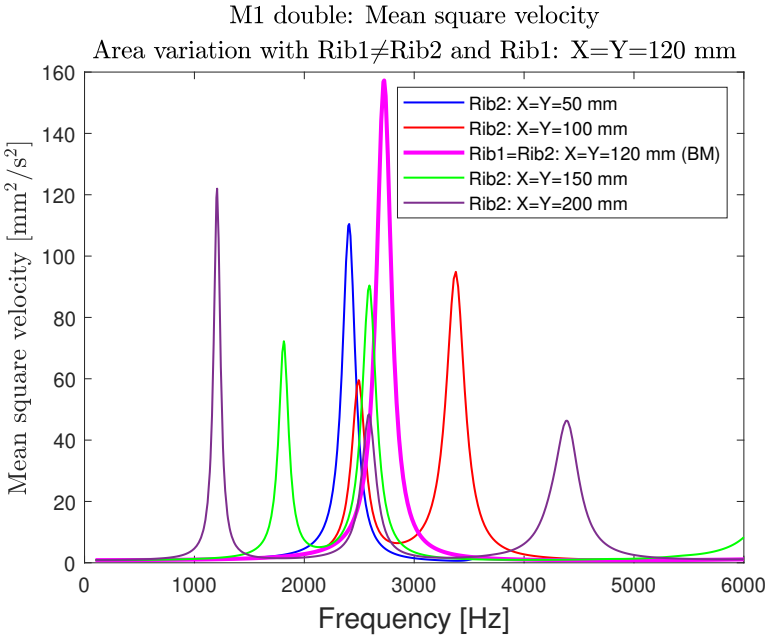

Figure A.63: Mean square velocity for M1 double of area variation with Rib1≠Rib2 and Rib1: X=Y=120 mm.

Rib1: X=Y=50 mm

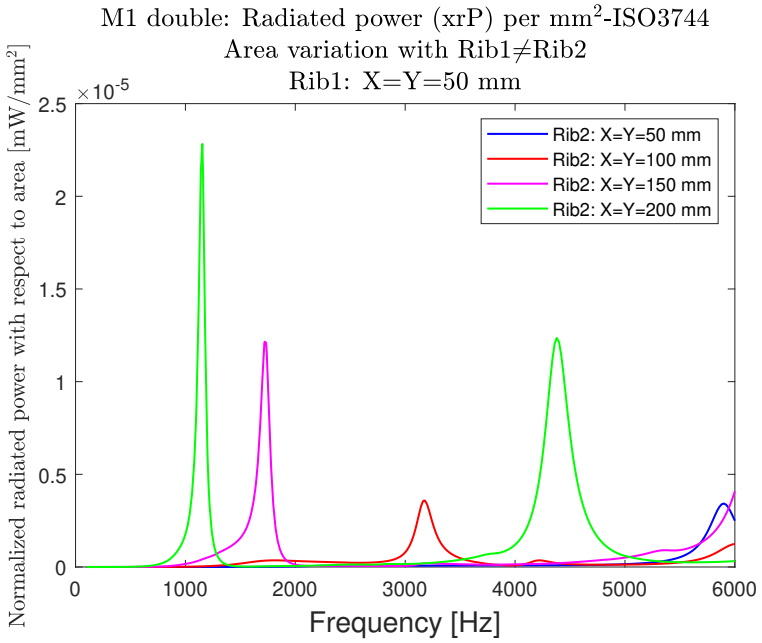

Figure A.64: Radiated power per mm^2 for M1 double of area variation with Rib1≠Rib2 and Rib1: X=Y=50 mm.

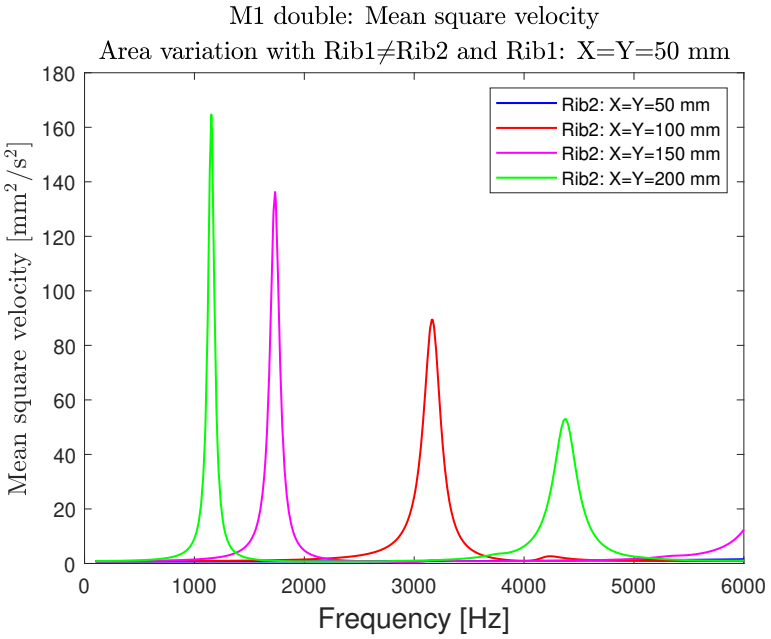

Figure A.65: Mean square velocity for M1 double of area variation with Rib1≠Rib2 and Rib1: X=Y=50 mm.

Rib1: X=Y=200 mm

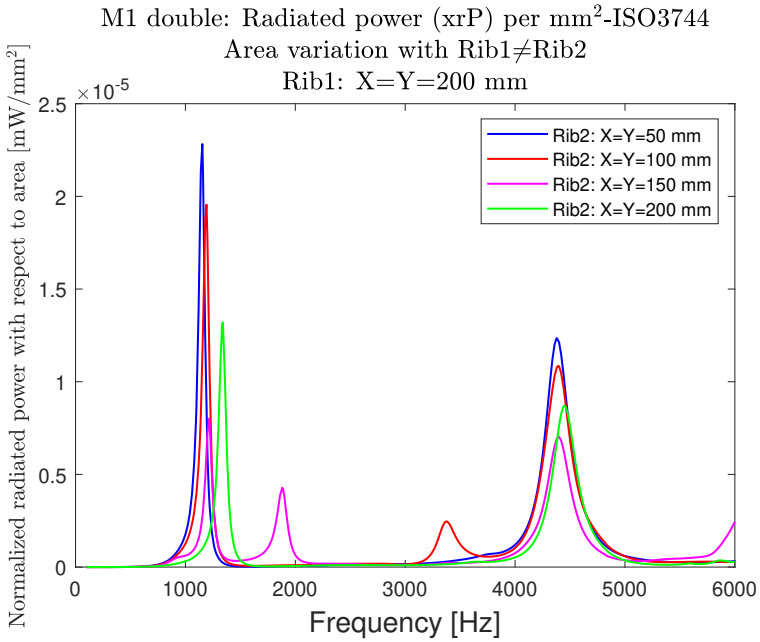

Figure A.66: Radiated power per mm^2 for M1 double of area variation with Rib1≠Rib2 and Rib1: X=Y=200 mm.

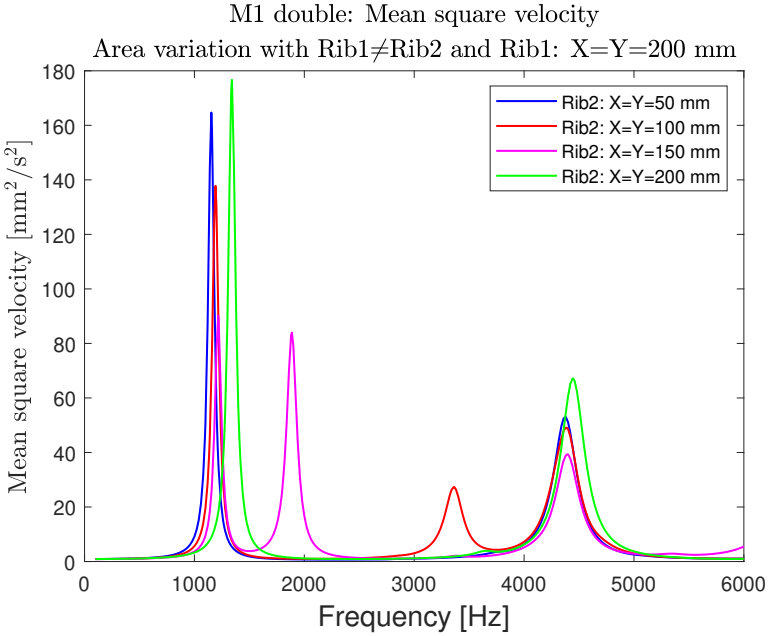

Figure A.67: Mean square velocity for M1 double of area variation with Rib1≠Rib2 and Rib1: X=Y=200 mm.

A.4.6 R variation

A.4.6.1 Rib1=Rib2

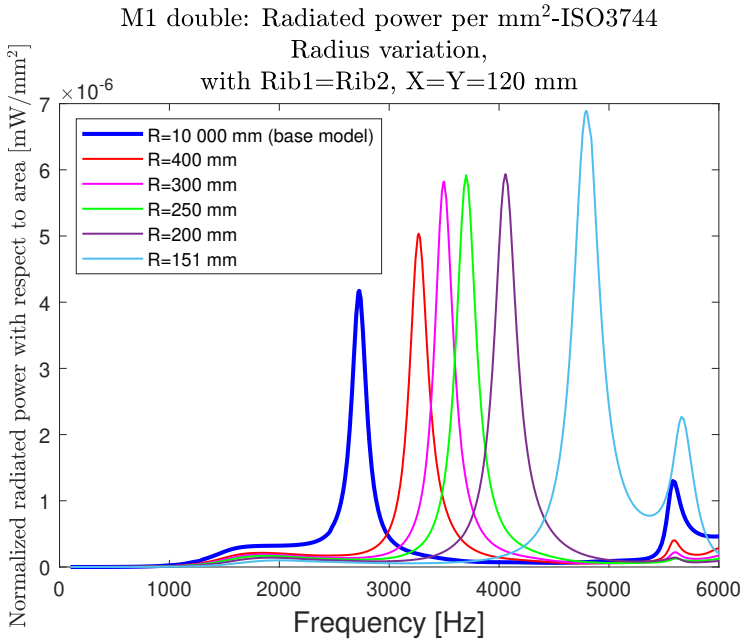

Figure A.68: Radiated power per mm^2 of M1 double for variation of the curvature R, where Rib1=Rib2.

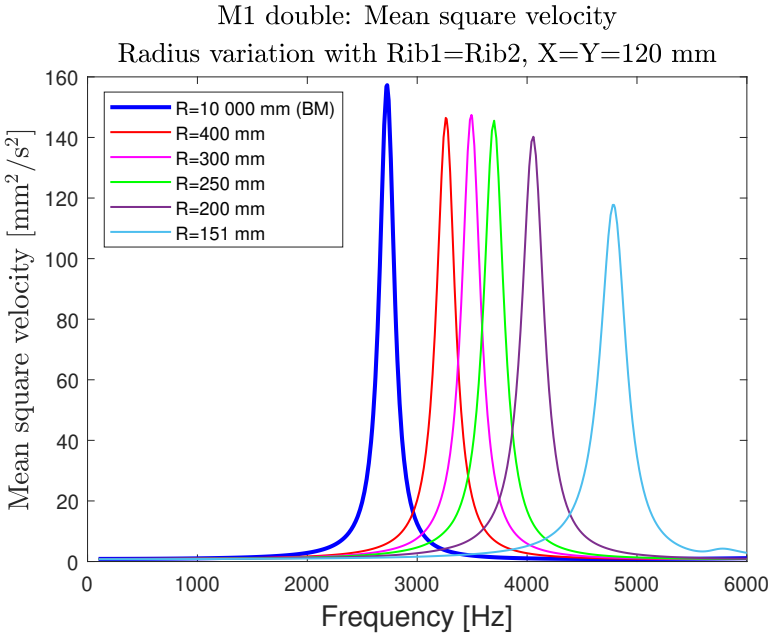

Figure A.69: Mean square velocity of M1 double for variation of the curvature R, where Rib1=Rib2.

A.4.6.2 Rib1≠Rib2, Rib1: R=151 mm

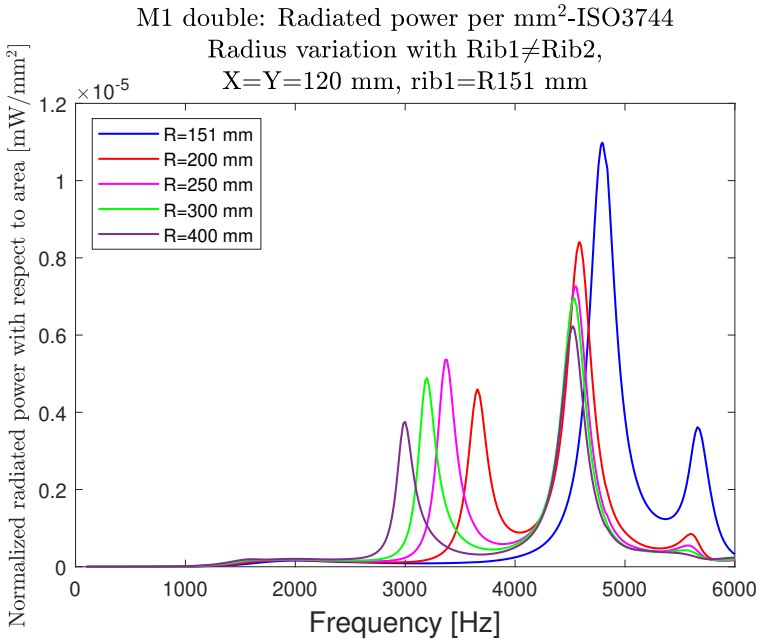

Figure A.70: Radiated power per mm^2 of M1 double for variation of the curvature R, where Rib1≠Rib2 and R for Rib1=151 mm.

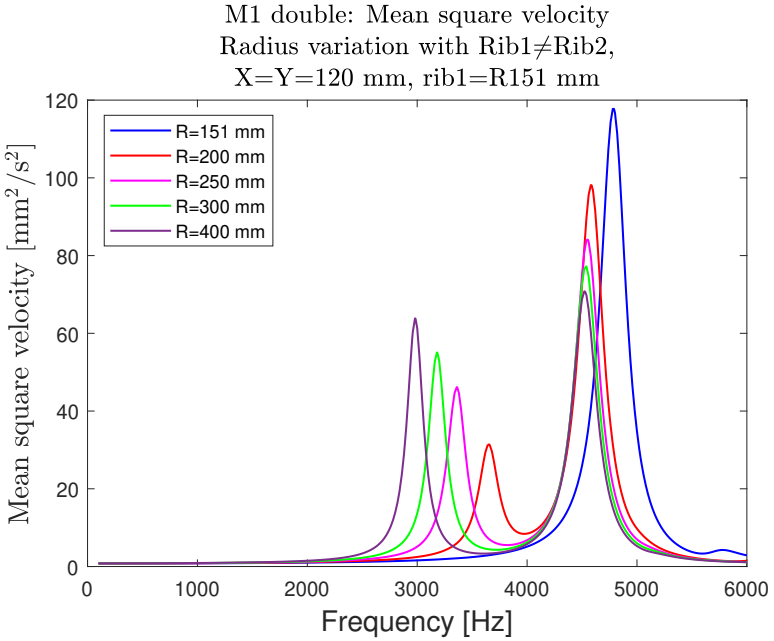

Figure A.71: Mean square velocity of M1 double for variation of the curvature R, where Rib1≠Rib2 and R for Rib1=151 mm.

A.4.6.3 Rib1≠Rib2, Rib1: R=10 000 mm

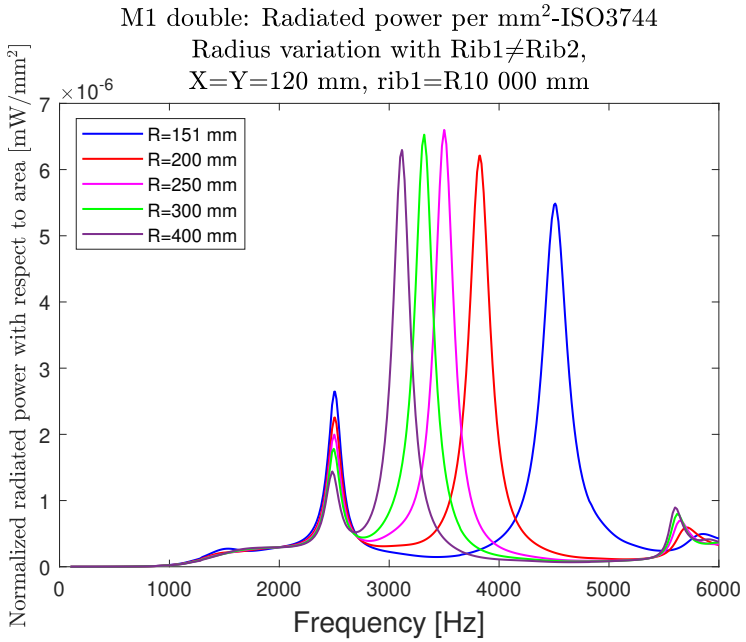

Figure A.72: Radiated power per mm^2 of M1 double for variation of the curvature R, where Rib1≠Rib2 and R for Rib1=10 000 mm.

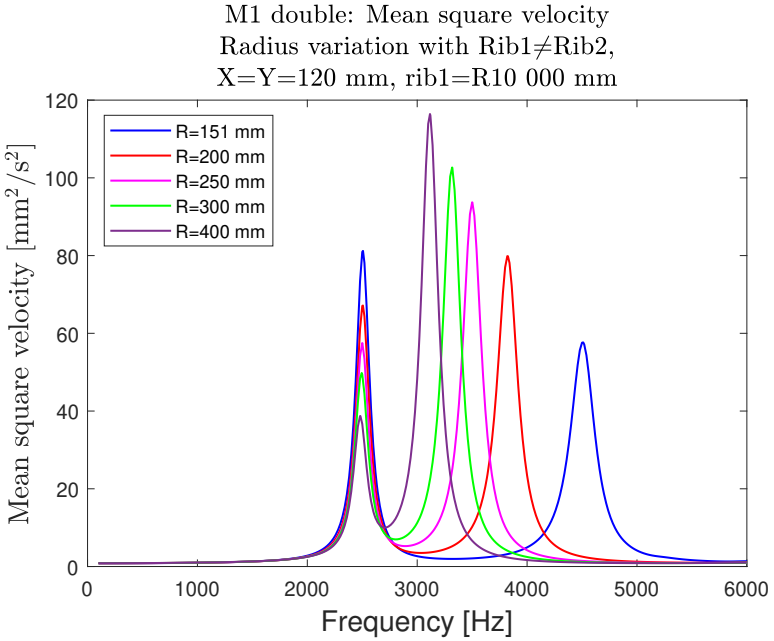

Figure A.73: Mean square velocity of M1 double for variation of the curvature R, where Rib1≠Rib2 and R for Rib1=10 000 mm.

A.4.6.4 Variation of the distance between the ribs

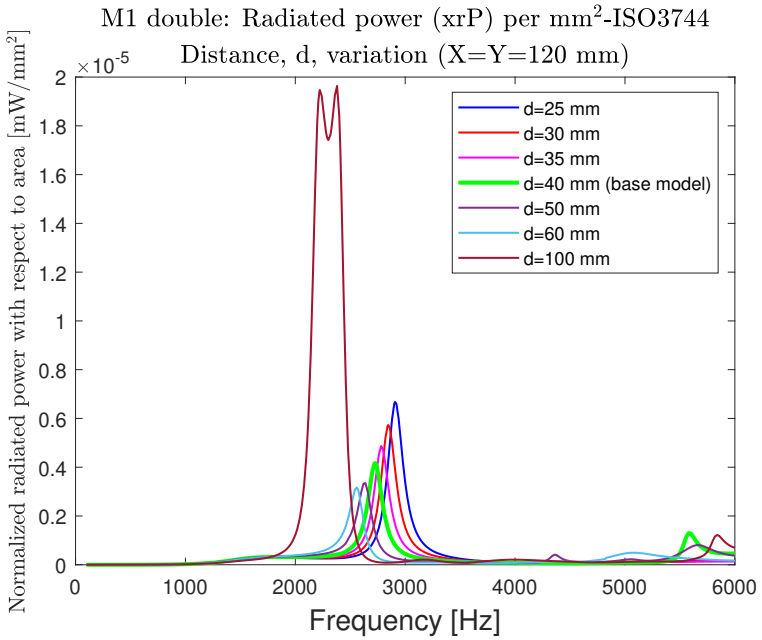

Figure A.74: Radiated power per mm^2 for M1 double of the distance between the ribs variation.

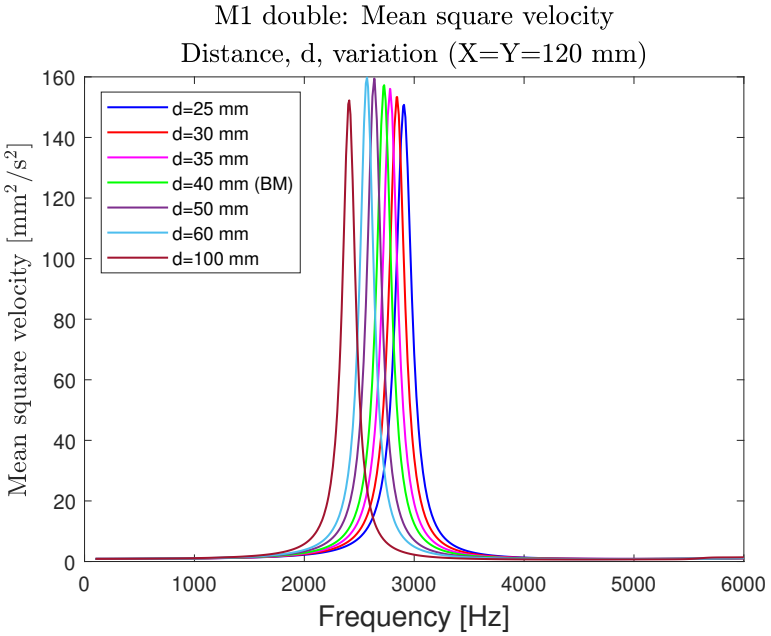

Figure A.75: Mean square velocity of M1 double of the distance between the ribs variation.

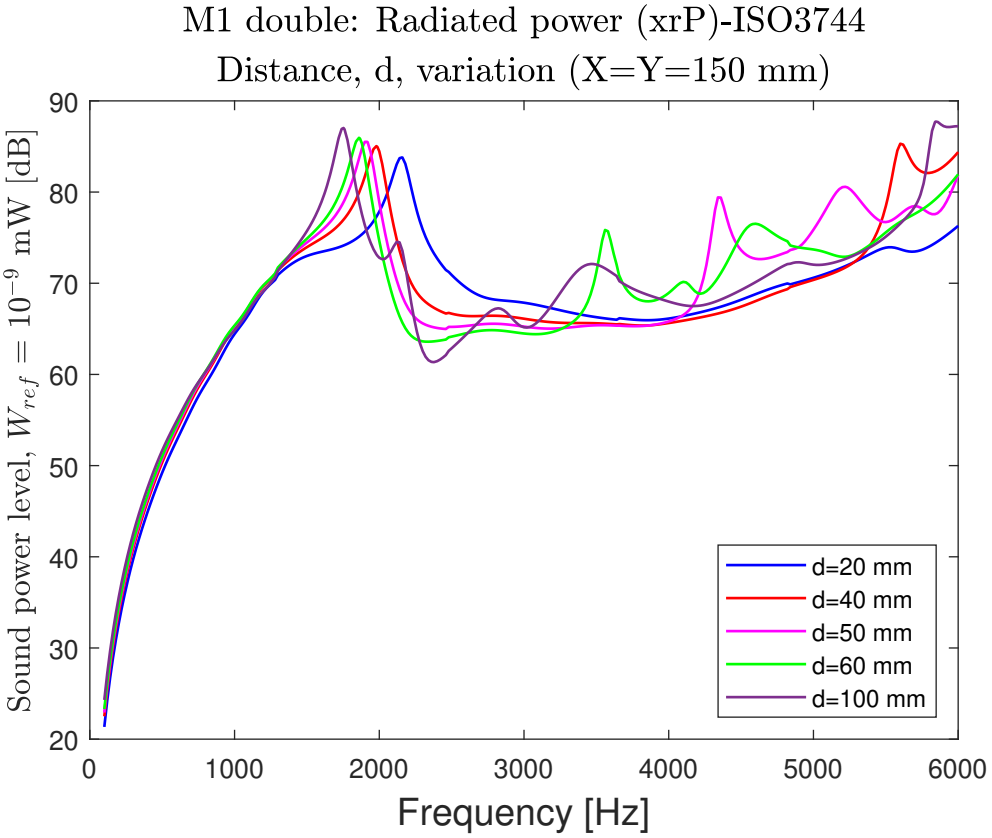

Figure A.76: Radiated power for M1 double of the distance between the ribs variation, X=Y=150 mm.

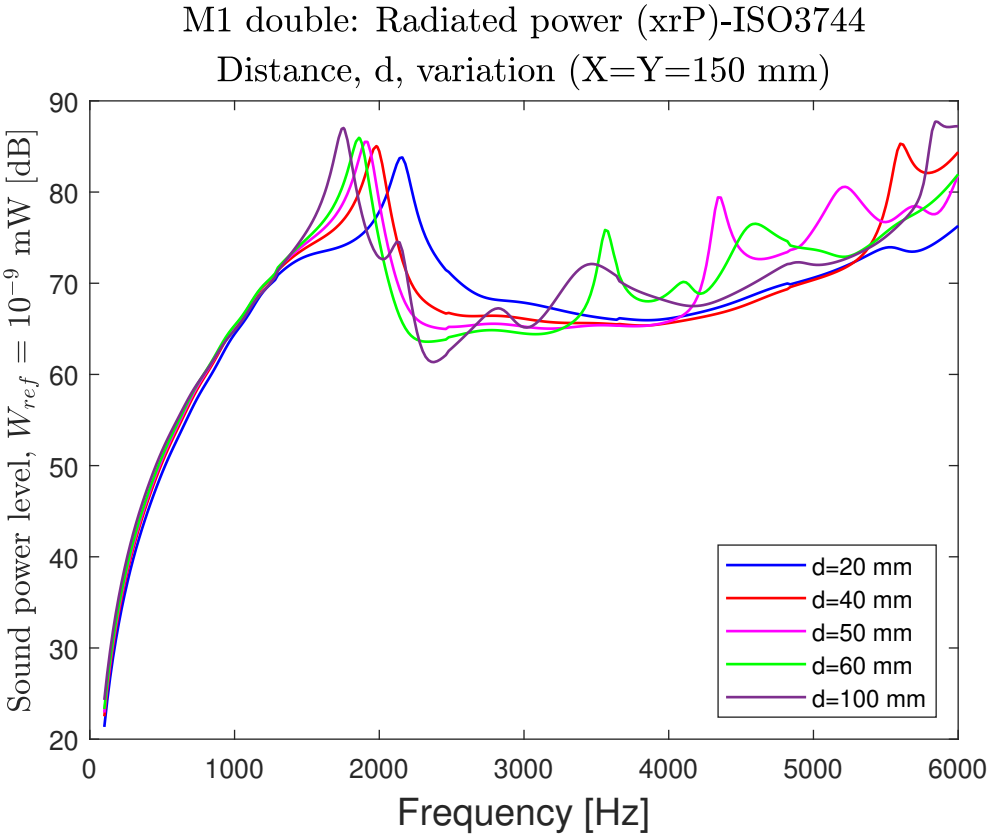

Figure A.77: Radiated power for M1 double of the distance between the ribs variation, X=Y=150 mm.

A.4.6.5 Variation of the angle between the ribs

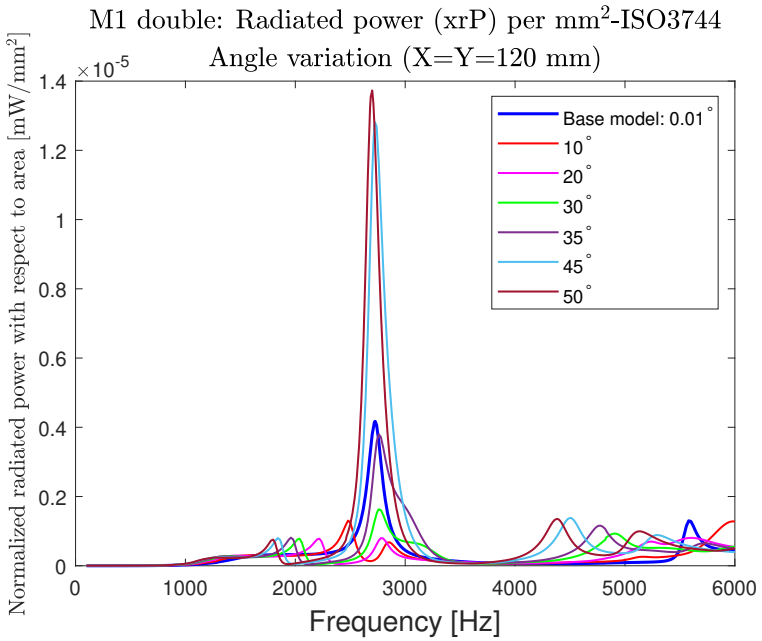

Figure A.78: Radiated power per mm^2 for M1 double of angle between the ribs variation.

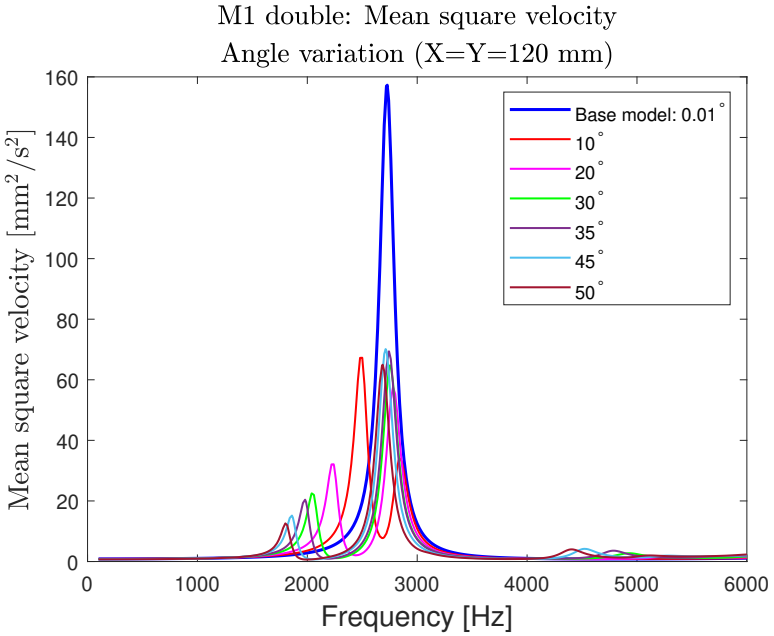

Figure A.79: Mean square velocity of M1 double of the angle between the ribs variation.

A.4.7 Constant volume between the ribs

For these simulations, the volume between the ribs is kept constant by changing the area (X and Y) of the ribs and the distance (d). Both ribs are always the same size.

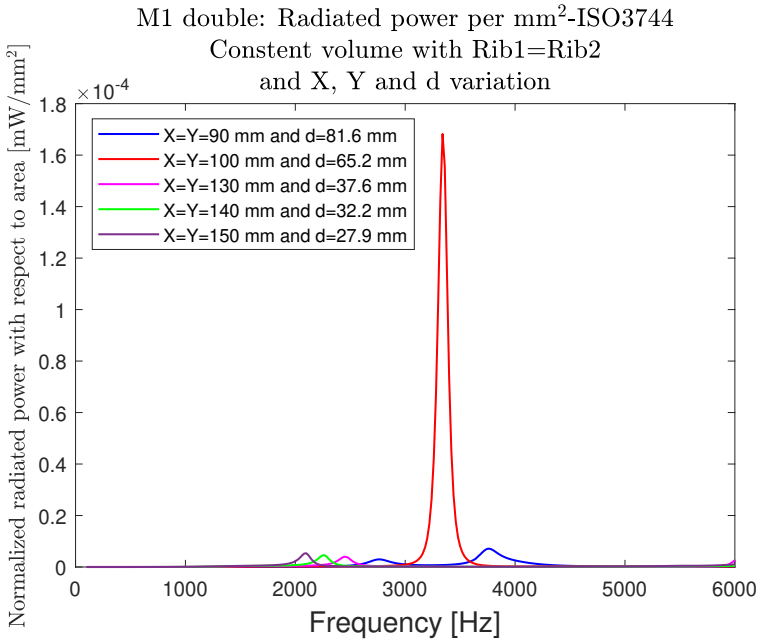

Figure A.80: Radiated power per mm^2 of M1 double with constant volume between the ribs.

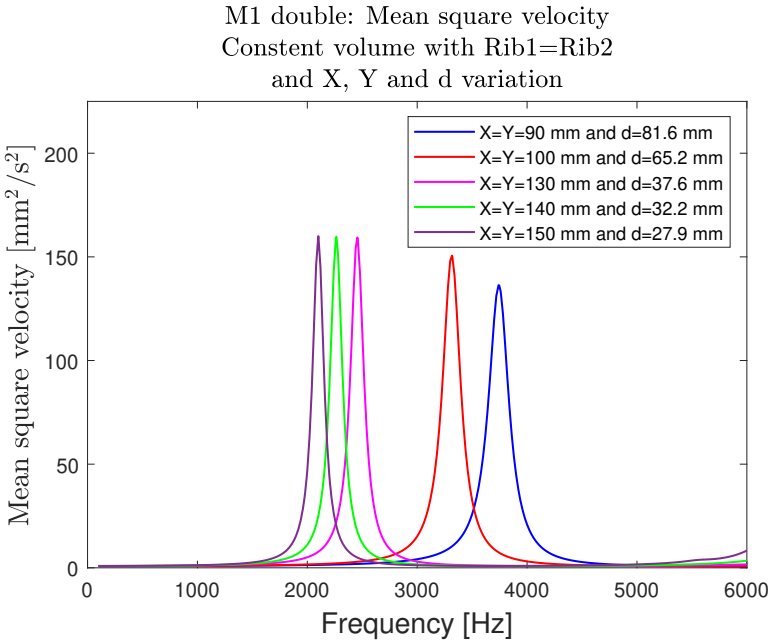

Figure A.81: Mean square velocity of M1 double with constant volume between the ribs.

DEPARTMENT OF MECHANICS AND MARITIME SCIENCES
CHALMERS UNIVERSITY OF TECHNOLOGY
Gothenburg, Sweden
www.chalmers.se

CHALMERS
UNIVERSITY OF TECHNOLOGY